METEOROLOGY HYDROLOGY AND WATER MANAGEMENT
IMGW-PIB Science Journal since 2013

VOL. 13 | ISSUE 2 | 2025

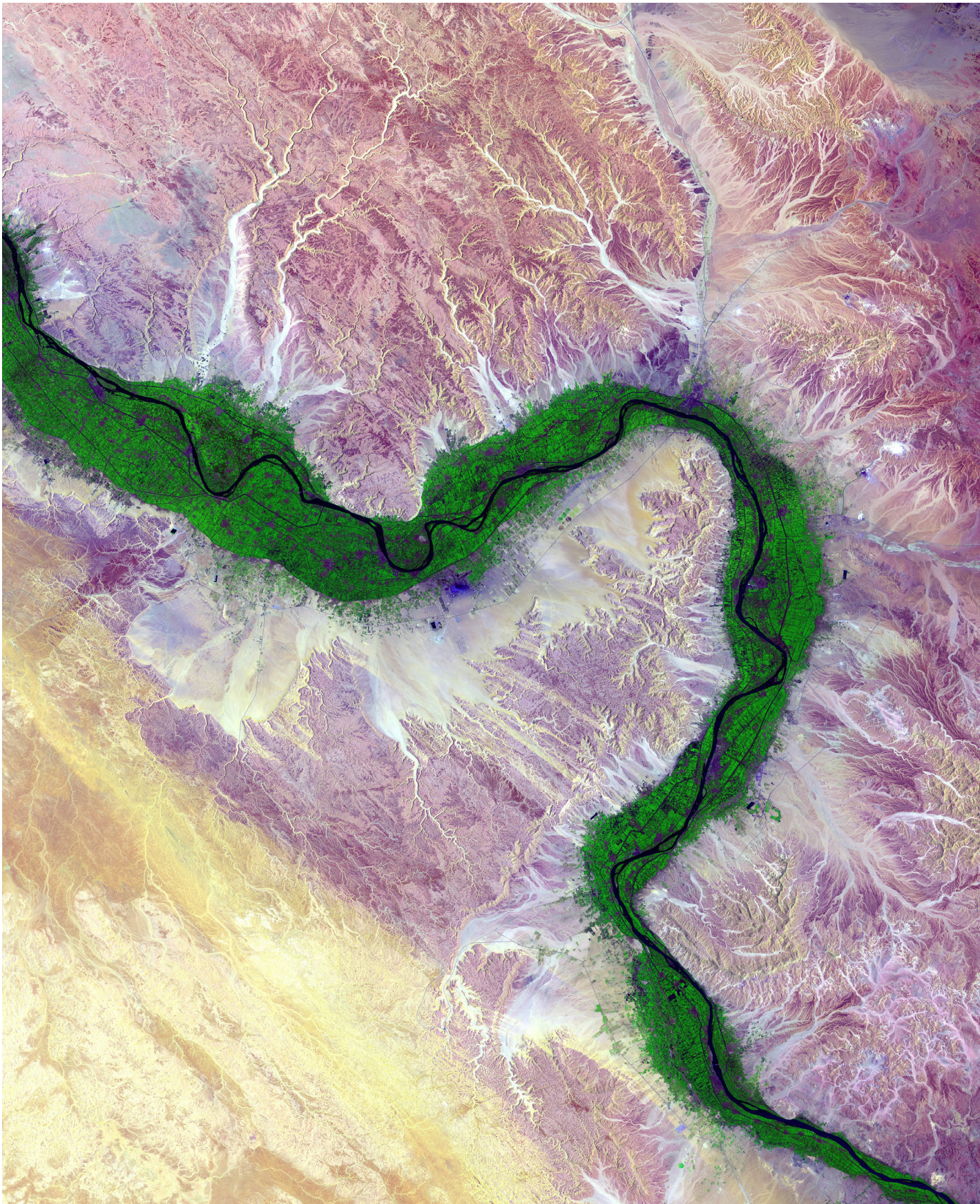

ISNN 2299-3835

Fluvial and flood regime characteristics of the Kaveri River: Southern India

Smita Ramesh Pagare, Pramodkumar Shivajirao Hire

HPT Arts and RYK Science College, Savitribai Phule Pune University, India

Archana Dilip Patil

RNC Arts, JDB Commerce and NSC Science College, India

Abstract

The channel form and processes of erosion and transportation in a river are intimately tied to the fluvial and flood regimes which, in turn, are controlled by the regional hydro-climatic conditions. The Kaveri River serves as a lifeline for the vast population. It is, therefore, necessary to understand the fluvial and flood regime characteristics of the river. Daily, monthly mean discharge data and the annual maximum series (AMS) data were obtained from the Central Water Commission. The analyses of data indicate that the monsoon regime plays a role of considerable importance in determining the river regime conditions. Like the parent stream, the mean annual hydrographs of the tributaries are characterized by one pronounced peak. Although the Kaveri River is perennial, more than 60 to 95% of the flows are recorded in the monsoon months. This is, therefore, the period of geomorphic effectiveness. The time series plots of AMS data reflect substantial maximum interannual variability. The unit discharge of the Kaveri Basin is 0.18 $m^3s^{-1}km^{-2}$, which is lower than other Indian rivers. The values of the coefficient of variation of AMS data range from 0.36 to 1.89, indicating low to high variability. All values of the coefficient of skewness (Cs) are positive and vary between 0.55 and 3.39. The positive values of Cs indicate a few very high-magnitude floods during the gauged period. The envelop curve of the Kaveri Basin falls much below the world envelop curve, revealing that the basin is not capable of producing very large magnitude floods for a given catchment area. The study of hydrographs indicates that large flows occur for 7 to 15 days. Thus, the investigation indicates that the fluvial and flood regime characteristics of the Kaveri River and its tributaries are controlled by monsoonal rainfall pattern and by the release of water from the reservoirs.

Keywords

Kaveri Basin, fluvial regime, flood regime.

Submitted 11 November 2024, revised 9 January 2025, accepted 2 September 2025

DOI: 10.26491/mhwm/210192

1. Introduction

The fluvial regime includes the general flow and performance of a river under natural circumstances, whereas the flood regime clearly highlights on the patterns and effectiveness of floods within a river. Both the notions are significant for understanding and managing rivers, their natural settings, and their impact on channel forms and processes. Incidentally, fluvial geomorphology is the study of interactions between river channel forms and processes at a range of space and time scales (Charlton 2008). The channel form and the processes of erosion and transportation in a river are closely associated with the fluvial and flood regimes, i.e. to the flow which they convey (Leopold et al. 1964; Schumm 1977). Flood geomorphology is concerned with the processes, forms, effects, and causes of floods (Baker et al. 1988). In certain hydro-geomorphic environments, such as the seasonal tropics, floods play a leading role in shaping the river channel and the landscape (Wohl 1992; Gupta 1995). Flood hydrology is essentially concerned with the quantification of hydrological processes and divination of floods. Flood hydrology, over the last one hundred years, has passed across an early observation phase, subsequently a stage of quantification of

hydrological processes, and then the current phase of development and appliance of methodologies for predicting floods (Chow 1964; Baker 1994). In current years, the bulk of research has dealt with the prediction of floods of different magnitude by adopting a variety of approaches. Usually, three main flood-prediction techniques, specifically deterministic, probabilistic and empirical techniques, have been employed in flood hydrology (Ward 1978). The phenomenon of flooding is a natural event which can be regarded as a natural feedback mechanism in order to continue the natural life cycle (Seth 1998). The building of a dam transversely on a river transforms the normal river reach into a stationary water body (Gopal 2016). This alters the hydrological regime of the river in terms of magnitude, frequency, extent, timing and the rate of changes in the flow characteristics. Such modifications in fluvial and flood regimes affect the ecological processes that control the functioning of fluvial ecosystem (Renofalt et al. 2010; Brauman et al. 2007). The objective of this paper is to understand the fluvial and flood regime characteristics of the Kaveri River of southern India and to apprehend the role of the construction of dams across the river and its tributaries on its regime characteristics. Around 96 dams have been constructed in the Kaveri Basin during the last 1000 years (Ekka et al. 2022).

2. Geomorphological and hydrological settings

The Kaveri (also spelled Cauvery) River is a sacred river in southern India and the oldest river in India. It drains a catchment area of 81,155 km² (Fig. 1). It rises in the Western Ghat at an elevation of 1341 m at Talakaveri in the Karnataka State. The river has the fifth largest drainage area in peninsular India, exceeded only by the Godavari, the Krishna, the Mahanadi, the Narmada Rivers. It flows for 800 km, from NW to SE, through the states of Karnataka, Tamil Nadu, Kerala, and Puducherry, and drains in to the Bay of Bengal. The basin is predominantly underlain by Archean-Proterozoic crystalline rocks, such as gneisses, charnockites and granites (Sharma, Rajamani 2001; Valdiya 2001). Quaternary sediments are predominant on the Tamil Nadu plains in the eastern part of the basin. Several N-S and E-W striking lineaments, faults, and shear zones characterize the catchment and the adjoining basins (Vaidyanadhan 1971; Valdiya 2001; Ramaswamy 2006). The basin is elongated in shape.

Two major topographic domains are recognized in the Kaveri Basin: (1) the elevated, low-relief Mysore Plateau with broad valleys and low-gradient streams in the west and (2) the fluvial-deltaic plains (known as the Tamil Nadu plains) to the east (Kale et al. 2014). Several residual hills and inselbergs characterize the Tamil Nadu plains. Between these two domains, there is a series of block mountains, including the Nilgiri, the Biligirirangan (BR), and the Mahadeswaramalai (MM) Hill Ranges and the Sheveroy Hill of Eastern Ghat. It is interested to note that none of the major tributaries joins the left bank in the Tamil Nadu plains.

The climate over the basin is monsoonal. The average annual rainfall of the basin is ~1172 mm (Pagare et al. 2025) (which from >2500 mm in the Western Ghat; headwaters) to ~700 mm in the lower reaches (Kale et al. 2014). Due to the orographic effect, the areas of high rainfall totals are confined to the Western Ghat zone as well as over the BR-MM hill ranges. Over three-fourth of the annual rainfall and

runoff occurs during the southwest monsoon season and about 85% of the annual sediments load is carried during the wet season (Vaithiyanathan et al. 1992). The average annual runoff of the basin is about 21.4 km^3 (CWC 2020), which is significantly lower than those of the other large rivers of the Indian peninsula, such as the Godavari (111 km^3), the Krishna (78 km^3), the Mahanadi (67 km^3) and the Narmada (46 km^3), implying very low unit discharges and rates of denudation.

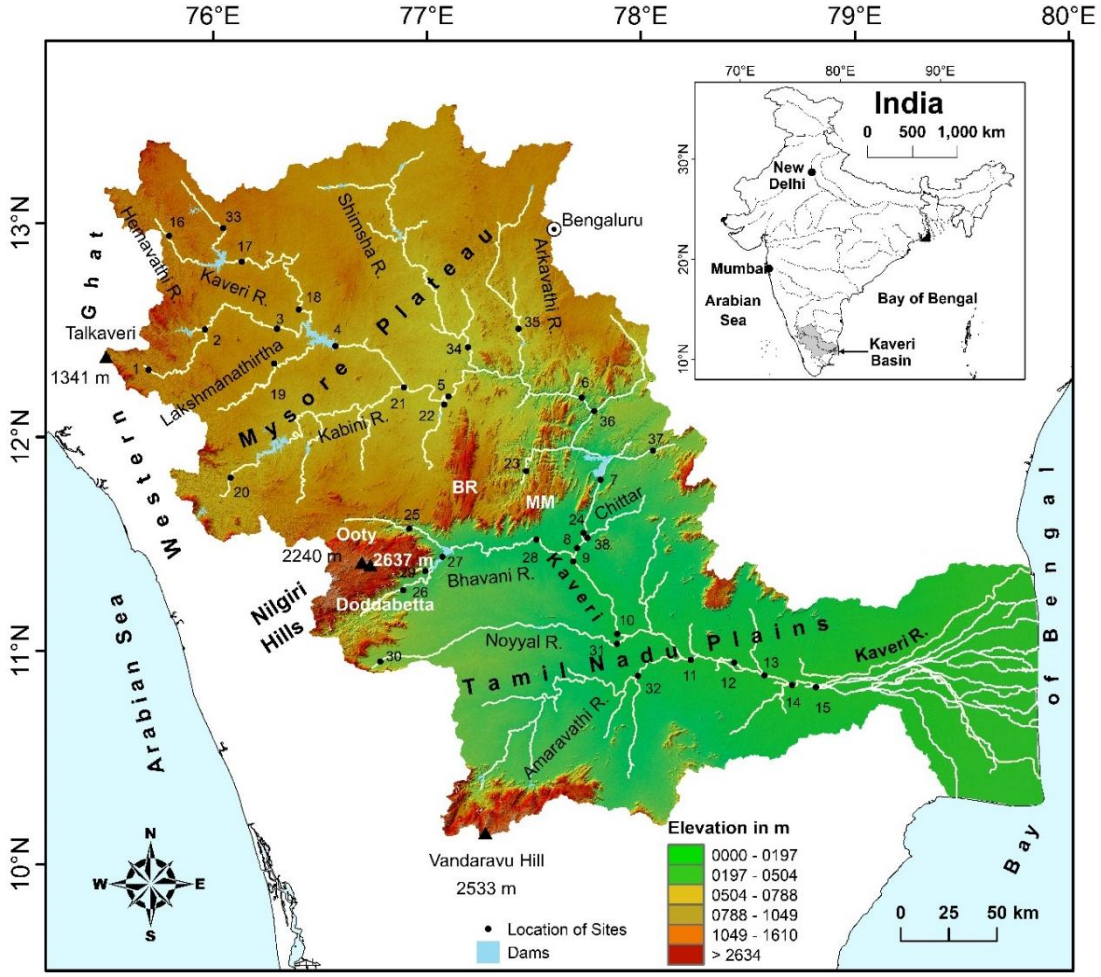

Fig. 1. Physiography of the Kaveri Basin and location of sites; 1 – Napoklu; 2 – Kudige; 3 – Chunchunkatte; 4 – Krishna Raja Sagara (KRS) Dam; 5 – Kollegal; 6 – Biligundulu; 7 – Mettur Dam; 8 – Urachikottai; 9 – Bhavani Bridge; 10 – Kodumudi; 11 – Kattalai Barriage; 12 – Musiri; 13 – Upper Anicut; 14 – Tiruchilapalli; 15 – Grand Anicut; 16 – Sakleshpur; 17 – M.H. Halli; 18 – Akkihebbal; 19 – K.M. Vadi; 20 – Muthankera; 21 – T. Narasipur; 22 – Bendrahalli; 23 – Kudlur; 24 – Sevanur; 25 – Thengumarahada; 26 – Nellithurai; 27 – Bhavanisagar Dam; 28 – Savandapur; 29 – Gandhavayal; 30 – Alandurai; 31 – E-Mangalam; 32 – Nallamaranpatty; 33 – Thimmanahalli; 34 – T.K. Halli; 35 – T. Bekuppe; 36 – Hogenakkal; 37 – Thoppur; 38 – Thevur.

3. Data and methodology

The channel forms and processes of erosion and transportation in a river are closely associated with the fluvial and flood regimes. Therefore, the daily, monthly and annual maximum series (AMS) data of the Kaveri River and its major tributaries are collected from the Central Water Commission (CWC 2020). The discharge regime, best conveyed by a mean annual hydrograph, is usually based on long-term records

(20-30 years) of mean monthly discharge data (Shaw 1988). In the presence of such long gauge records for the selected sites on the Kaveri River, mean annual hydrographs are drawn on the basis of mean monthly discharge data for 40 to 48 years. Further, to enhance understanding about the daily variations in discharge on the Kaveri River, the daily discharge data for one water year (June 2018 to May 2019) are graphically portrayed. Although the 2018-2019 water year happens to be a wet monsoon year, the choice of the water year was merely based on the availability of daily discharge data for a number of sites in the Kaveri Basin. A flood, in a general sense, is defined as a rise in the water level/stage or discharge that results in the overtopping of natural or artificial banks of a stream (Rostvedt et al. 1968, cf. Ward 1978). In hydrology, a flood may be any relatively high water level or discharge above a pre-determined flood level or discharge magnitude (Ward 1978). The measured instantaneous peak flood discharges constitute one of the most important datasets for hydrologists, engineers, environmental planners and geomorphologists. Hydrologists define the highest peak discharge recorded in each year for a series of years at a gauging site as annual peak discharge series or annual maximum series (AMS) (Ward 1978). The AMS data of six sites on the Kaveri River and eight sites on its tributaries have been used to understand flood regime characteristics. First, the AMS data are presented in the form of time series plots to interpret in the interannual variations in the annual peak flood magnitudes. Moreover, in order to further highlight the extent of variability in peak discharges from one year to other, deviations from mean annual peaks have been shown graphically. Second, to reduce and summarize the characteristics of floods, simple statistical analyses of AMS data are carried out. Commonly-used statistical parameters such as average, variability, skewness (Cs), coefficient of variation (Cv), Cs/Cv ratio, etc. are calculated to understand flood regime conditions of the river. In addition to this, the flash flood magnitude index ($FFMI$) and unit discharges are derived to evaluate the variability and the potential of large floods on the Kaveri River and its tributaries. Furthermore, unit discharges are calculated and used to construct an envelope curve for the Kaveri Basin. Flood hydrographs are constructed to understand the characteristics of the floods of the river and its tributaries. The maps used for the present study are based on the analysis of ca. 30-m resolution SRTM-DEM data processed in ArcGIS Desktop: Release 10.8.

4. Results and discussion

4.1. Fluvial regime characteristics

The Kaveri River has the unique locational advantage in the sense that its upper catchment area receives rainfall during summer from the southwest monsoon, and the lower catchment area during the winter season from the retreating northeast monsoon. Like other monsoon-dominated rivers, the Kaveri River also shows changes in discharge characteristics from year to year as well as from season to season. Nevertheless, the interannual and inter-seasonal variations in discharge shows a distinct average annual pattern of variations which is best displayed by the mean annual hydrographs. The mean annual hydrographs provide a good idea about the periods of high and low flows as well as the range of streamflows in a river during a year (Shaw 1988). Such graphs have been constructed for a few stations to understand the main features of the fluvial regime of the Kaveri River and its tributaries.

4.1.1. Mean annual flow pattern

The mean annual flow pattern of six sites on the Kaveri River and three sites on its major tributaries are based on 40 to 48 years of data and given in Figure 2 and Table 1. A cursory examination of the mean annual hydrographs indicates that the annual flow pattern reflects the seasonal rhythm of the monsoon rainfall plus water released from reservoirs during the non-monsoon season. There is flow in the monsoon months (June to November) and it dwindles in non-monsoon months (December to May). The highest flows occur at all the sites in between July and September except at Savandapur and Nellithurai site on the Bhavani River. By this time, maximum annual rainfall is received by the basin and the soils are fully saturated. Hence, even unexceptional heavy rains produce high runoff. The lower mean flows at Savandapur is attributed to the Lower Bhavani Reservoir and, at Nellithurai, is ascribed to several small dams on the Bhavani River upstream of this site. The peak mean flows are observed at the Kollegal and Biligundulu sites in the month of August. Both the sites are located downstream of the second largest dam on the Kaveri River, i.e. Krishna Raja Sagar (KRS) Dam. Therefore, the mean annual flow at these two sites is controlled by this dam. However, the flow regime of the Kodumudi, Musiri and Urachikottai sites is regulated by Mettur Dam which is the largest dam on the Kaveri River. The mean peak flows at these sites are observed in the month of August. This pattern is expected because water is stored in the Mettur Dam in the month of July.

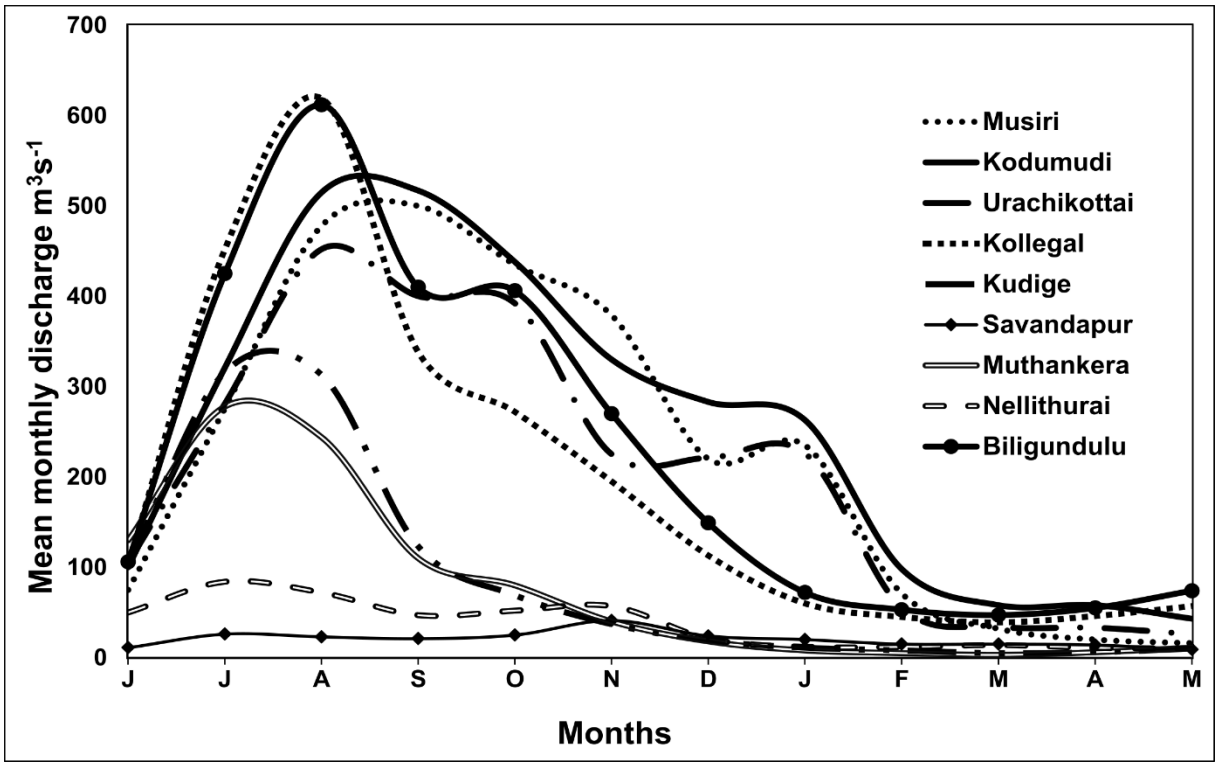

Fig. 2. Flow regime of the Kaveri River and its major tributaries; See Figure 1 for location of sites.

The nature of mean annual hydrographs for all the sites on the Kaveri River suggests that the contribution of groundwater to the streams during the dry season is generally negligible. This means that most of the

geomorphic work of erosion and transportation is confined during the monsoon months of the year and the maximum geomorphic work is accomplished in the months of July and August.

Table 1. Flow characteristics of the Kaveri River and its major tributaries with gauging sites. (Averages of the monthly mean discharges m^3s^{-1} (1971-2019; 40 to 48 years of record)).

Months	Kaveri Musiri	Kaveri Kodumudi	Kaveri Urachikottai	Kaveri Biligundulu	Kaveri Kollegal	Kaveri Kudige	Bhavani Savandapur	Kabini Muthankera	Bhavani Nellithurai	Shimsha T.K.. Halli	Hemavathy M.H. Halli
J	75	100	105	106	103	104	11	130	50	8	15
J	276	321	281	425	452	316	26	278	84	7	63
A	478	515	452	612	619	313	23	244	72	21	104
S	500	517	400	410	338	123	21	110	47	59	60
O	435	438	392	406	272	69	25	80	52	67	42
N	379	330	225	270	195	37	41	40	57	41	35
D	220	283	221	149	113	19	24	18	21	20	23
J	235	263	226	72	60	11	20	8	12	7	16
F	71	98	55	53	45	8	15	5	12	4	18
M	32	58	34	47	39	5	15	3	14	4	17
A	20	58	33	55	46	6	14	6	11	4	19
M	16	43	26	74	57	10	9	11	10	7	18
A.T. (J-M)	2737	3024	2450	2679	2339	1021	244	933	442	249	430
M.T. (J-N)	2143	2221	1855	2229	1979	962	147	882	362	203	319
N.M.T.(D-M)	594	803	595	450	360	59	97	51	80	46	111
M.A.F. m^3/s (J-M)	228	252	204	223	195	85	20	78	37	21	36
M.M.F. m^3/s (J-N)	357	370	309	372	330	160	25	147	60	34	53
% of M.F. (J-N)	78	73	76	83	85	94	60	95	82	82	74
% of N.M.F. (D-M)	22	27	24	17	15	6	40	5	18	18	26

J-D – January to December; A.T. (J-M) – Annual Total (June-May); M.T. (J-N) – Monsoon Total (June-November); N.M.T. (D-M) – Non-Monsoon Total (December-May); M.A.F. (J-M) – Mean Annual Flow (June-May); M.M.F. (J-N) – Mean Monsoon Flow (June-November) N.M.F. – Non-Monsoon Flow; M.F. (J-N) – Monsoon Flow (June-November); N.M.F. (D-M) – Non-Monsoon Flow (December-May); Data source: CWC; See Figure 1 for location of sites.

Mean annual hydrographs give an average picture; however, the diurnal variations in discharge are insufficiently expressed by such graphs. Therefore, to get an idea about the nature of changes in the daily discharges during the wet season, the diurnal discharge for one water year (June 2018 to May 2019) has been plotted in Figure 3 and 4. The figures clearly indicate that the wet period (June to November) is characterized by multiple, short and sharp flood peaks. For some sites on the Kaveri River, the discharge may vary by as much as 2500 to 7500 m^3s^{-1} in a single day; for instance, at the Musiri site. As expected, it is interesting to note that all peak flows match from the upstream to downstream gauging sites.

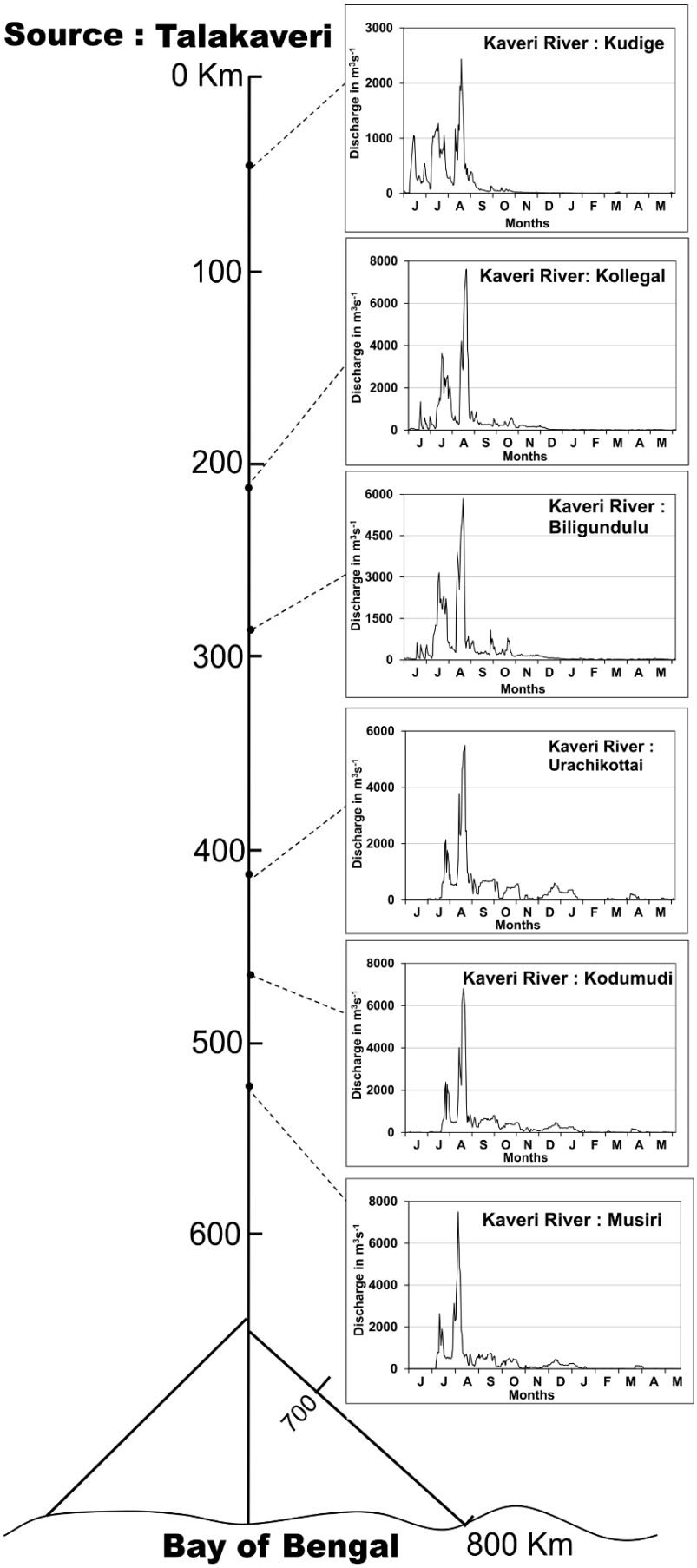

Fig. 3. Annual hydrographs of the Kaveri River; See Figure 1 for location of sites.

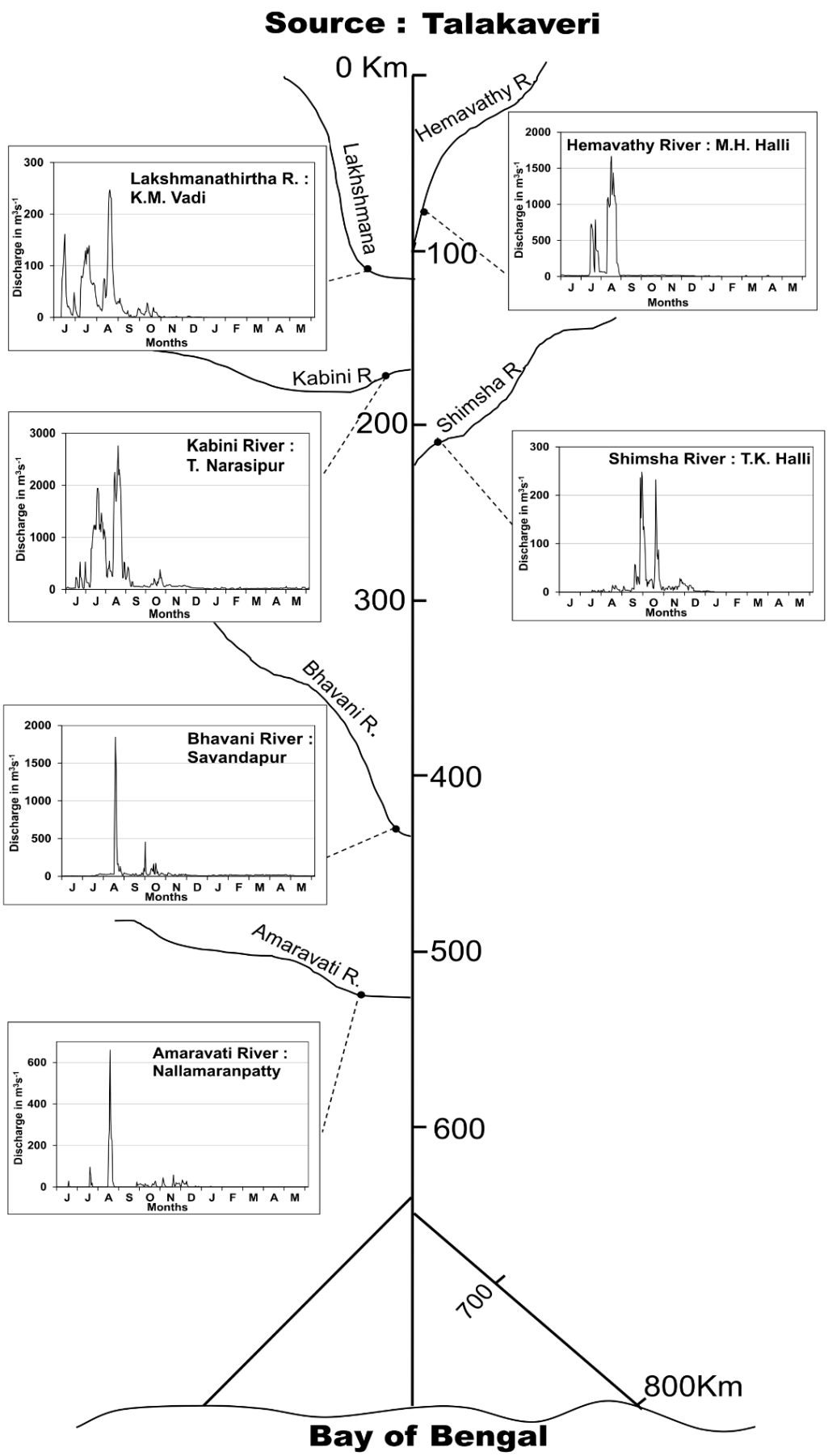

Fig. 4. Annual hydrographs of tributaries of the Kaveri River; See Figure 1 for location of sites.

The average flow characteristics of six sites on the Kaveri River and eight sites on the tributaries are given in Table 1. The analysis show that the monsoon flows range between 60% and 95%. On the other hand, non-monsoon flows vary between 5 and 40%. The table also indicates that the Kaveri River, as well as its largest tributary, the Kabini, experiences high discharge in the months of July to October. The percentage of non-monsoon flows are invariably less than 25% in the case of all the sites on the Kaveri River and its tributaries, except the Bhavani River at Savandapur (Non-monsoon flow is 40%). This is attributed to the release of water from the Lower Bhavani Reservoir during the non-monsoon season. The average flow characteristics clearly reveal that the geomorphic work of erosion and transportation is confined during the monsoon months of the year, i.e. from June to November. However, the maximum geomorphic work is accomplished in the months of July and August. The mean annual flow pattern of the Tapi and Mahi Rivers of central India specify that the rivers experience over 90% of the annual flows during the monsoon season (June to October), and during the dry season (November to May) the flow magnitude is very low (Hire 2000; Pawar 2019). It shows a slightly dissimilar pattern of monsoon rainfall.

4.2. Flood regime characteristics

It is evident from the above discussion that the monsoon regime plays a role of considerable importance in determining the fluvial regime conditions of the river under study. However, the usefulness of discharge regime characteristics is limited for geomorphological purposes because it is based on monthly means. Most of the geomorphic work in seasonal tropics is accomplished by individual flood events, which are not sufficiently signified by monthly means. Research on some large Indian rivers demonstrate that the channel morphology and fluvial processes are related to very large but relatively infrequent flood events (Goswami 1985; Kale et al. 1994; Gupta 1995; Gupta et al. 1999; Hire 2000; Pawar 2019; Patil 2017; Patil et al. 2024a, 2024b). Therefore, an attempt has been made to understand the magnitude, variability and frequency characteristics of individual floods on the Kaveri River and its tributaries on the basis of available annual peak discharge data.

4.2.1. Interannual variability in annual peak discharges

The temporal patterns of variation in the annual peak discharges at six sites on the Kaveri River and eight sites on its tributaries are illustrated in Figures 5 and 6. All graphs reveal a high interannual variability in the annual peak discharges. The figures also show the occurrence of a very few large events during the gauge period.

4.2.2 Average magnitude and variability of floods

The available gauged data indicate that the mean discharges range between 299 and 2621 m^3s^{-1} on a tributary of the Kaveri River, namely Lakshmanathirtha at the K.M. Vadi, and at the Kollegal site on the mainstream, respectively (Tab. 2). According to Kochel (1988) floods that are likely to cause significant geomorphic change are those that produce discharges many times above the mean flows experienced by a river. This can be simply established by estimating the $Qmax/Qm$ ratio. Table 2

demonstrates that, for most sites, the *Qmax/Qm* ratio varies between 2 and 10. This specifies that maximum annual peak discharges (*Qmax*) are 2 to 10 times higher than average peaks, since the more variable the flow is, the more important the higher discharges become (Wolman, Miller 1960). The effect of such extreme flows on geomorphic activity in channel is unquestionably noteworthy. It is interesting to note that the Amaravati River at Nallamaranpatty site shows that the maximum annual peak discharge is about 10 times higher than the mean annual peak discharge. Therefore, this *Qmax* would have caused remarkable geomorphic changes in the channel of the Amaravati River.

Besides the *Qmax/Qm* ratio, the coefficient of variation (*Cv*) is another useful measure of variability in the annual peak discharges. The *Cv* is the ratio between the standard deviation and the mean. The *Cv*(*s*) for the sites under investigation range between 0.36 and 1.89 (or 36 to 189%) which shows low to very high variability in the AMS (Tab. 3). As per earlier discussion, as expected, the *Cv* of the Amaravati River at Nallamaranpatty is maximum.

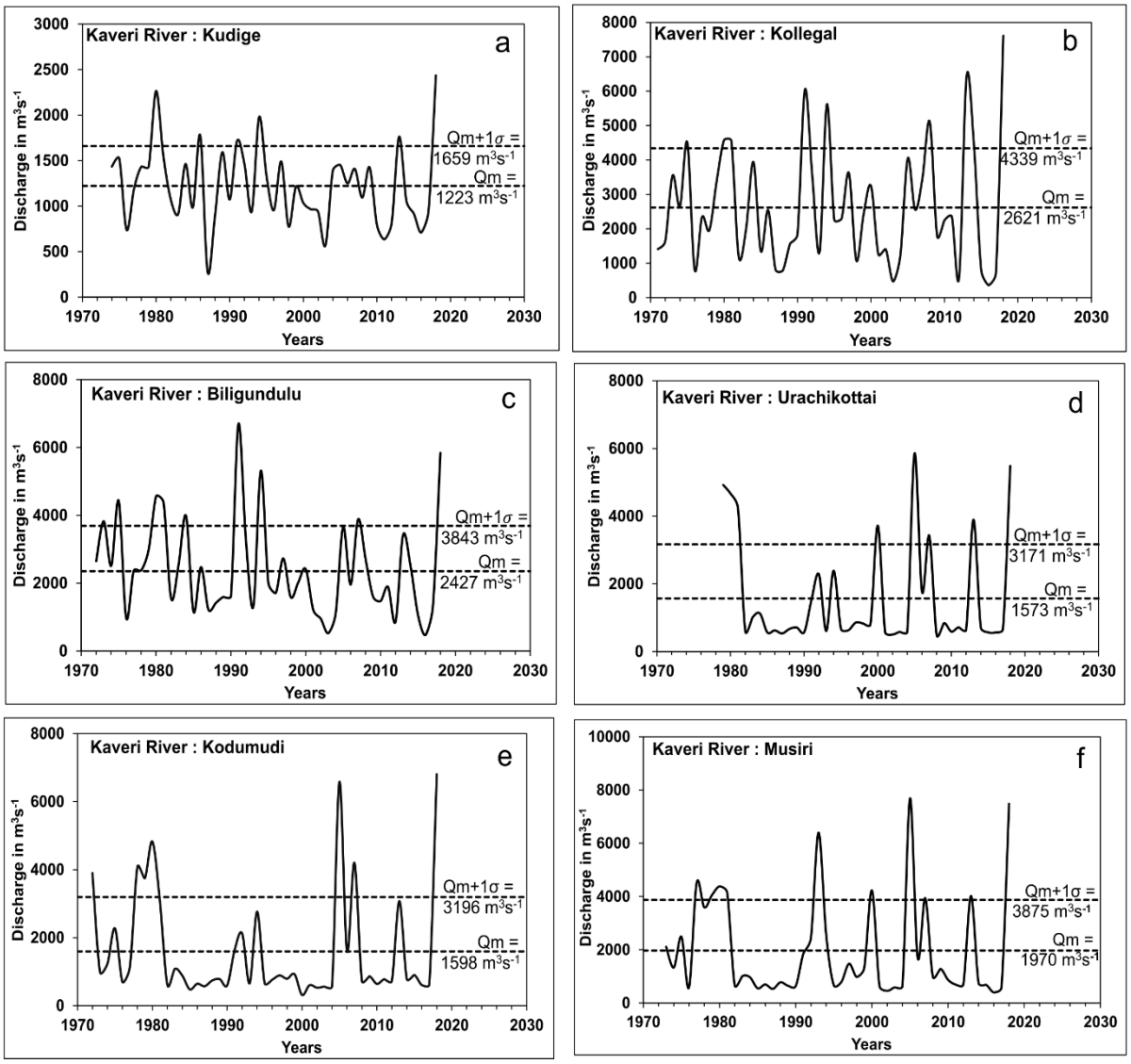

Fig. 5. Annual maximum series of the Kaveri River; See Figure 1 for location of sites.

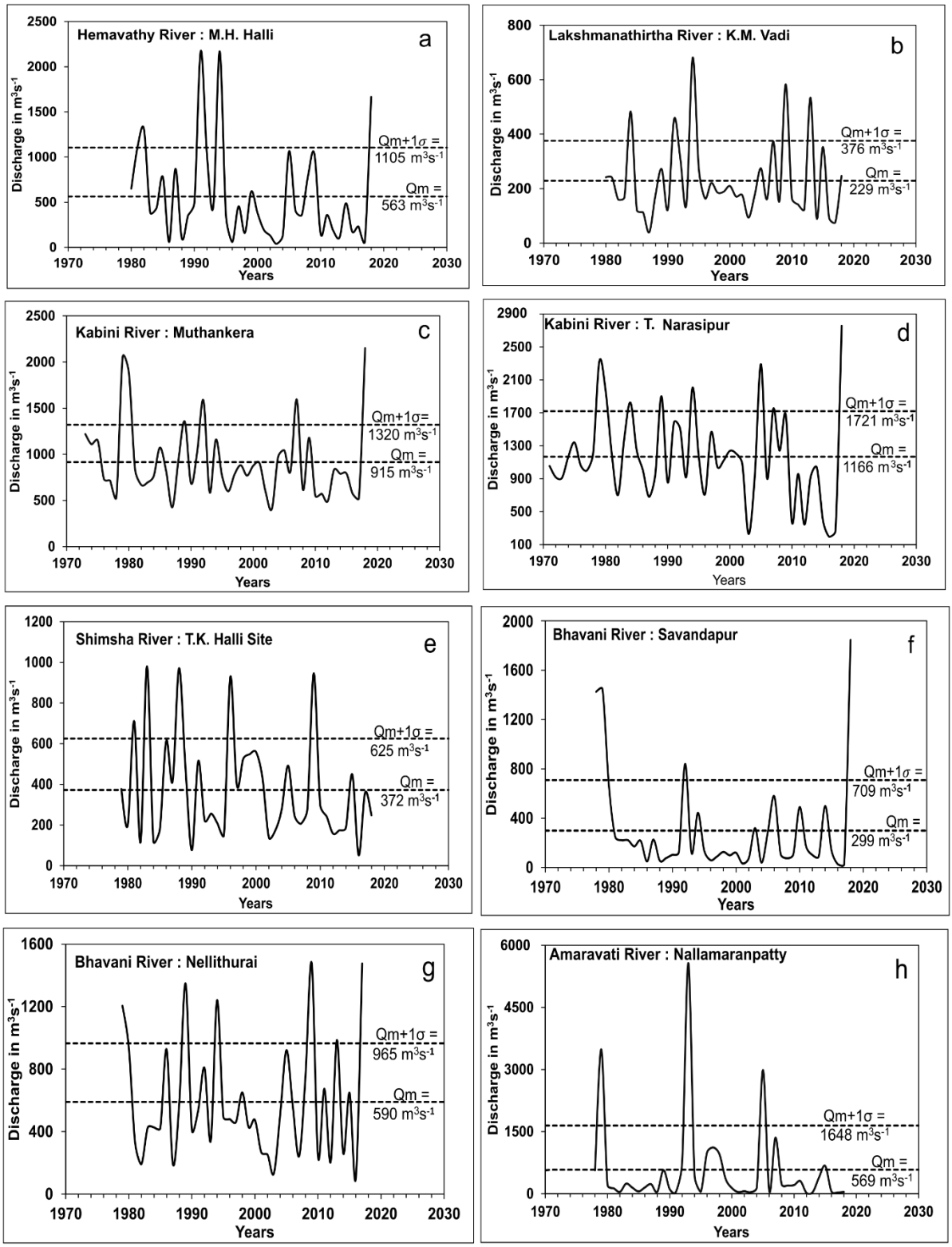

Fig. 6. Annual maximum series of tributaries of the Kaveri River; See Figure 1 for location of sites.

Table 2. Flood flow characteristics of the Kaveri River and its major tributaries.

SN	River	Site	*A* [mm²]	*RL*	*Qmin* [m³s⁻¹]	*Qmax* [m³s⁻¹]	*Qm* [m³s⁻¹]	Flood range	*Qmax/ Qm*
1	Kaveri	Kudige	1934	45	279	2435	1223	2156	1.99
2	Kaveri	Kollegal	21082	48	360	7609	2621	7249	2.90
3	Kaveri	Biligundulu	36682	47	470	6688	2427	6218	2.76
4	Kaveri	Urachikottai	44100	40	485	5855	1573	5370	3.72
5	Kaveri	Kodumudi	53233	47	314	6808	1598	6494	4.26
6	Kaveri	Musiri	66243	46	400	7690	1970	7290	3.90
7	Hemavathy	M.H. Halli	3050	39	39	2172	563	2133	3.86
8	Lakshmanathirtha	K.M. Vadi	1330	39	39.93	681	229	641	2.97
9	Kabini	T. Narasipur	7000	48	194	2757	1166	2563	2.36
10	Kabini	Muthankera	1260	46	409	2150	915	1741	2.35
11	Shimsha	T.K. Halli	7890	40	51.24	980	372	928	2.63
12	Bhavani	Savandapur	5776	41	25.96	1845	299	1819	6.17
13	Bhavani/Moyar	Thengumarahada	1370	40	29.65	653	148	623	4.41
14	Bhavani	Nellithurai	1475	39	103	1478	590	1375	2.51
15	Noyyal	E-Mangalam	3386	20	0	175	60	175	2.92
16	Amaravati	Nallamaranpatty	9080	41	21	5571	569	5550	9.79

Qmin – Minimum annual peak discharge; *Qmax* – Maximum annual peak discharge; *Qm* – Mean annual peak discharge; *A* – Catchment area; *RL* – Record Length; Data source: CWC; See Figure 1 for location of sites.

Table 3. Discharge characteristics of the Kaveri River and its major tributaries.

SN	River	Site	*RL*	*Qmax* [m³s⁻¹]	*Qm* [m³s⁻¹]	Σ [m³s⁻¹]	*Cv*	*Cs*	*Cs*/Cv
1	Kaveri	Kudige	45	2435	1223	436	0.36	0.55	1.54
2	Kaveri	Kollegal	48	7609	2621	1717	0.66	0.93	1.42
3	Kaveri	Biligundulu	47	6688	2427	1416	0.58	1.08	1.85
4	Kaveri	Urachikottai	40	5855	1573	1597	1.02	1.53	1.51
5	Kaveri	Kodumudi	47	6808	1598	1597	1.00	1.88	1.88
6	Kaveri	Musiri	46	7690	1970	1905	0.97	1.57	1.62
7	Hemavathy	M.H. Halli	39	2172	563	541	0.96	1.63	1.70
8	Lakshmanathirtha	K.M. Vadi	39	681	229	145	0.63	1.52	2.40
9	Kabini	T. Narasipur	48	2757	1166	554	0.48	0.62	1.30
10	Kabini	Muthankera	46	2150	915	404	0.44	1.50	3.40
11	Shimsha	T.K. Halli	40	980	372	253	0.68	1.14	1.68
12	Bhavani	Savandapur	41	1845	299	409	1.37	2.53	1.85
13	Bhavani/Moyar	Thengumarahada	40	653	148	151	1.02	1.99	1.95
14	Bhavani	Nellithurai	39	1478	590	375	0.64	0.98	1.54
15	Noyyal	E-Mangalam	20	175	60	42	0.70	0.90	1.29
16	Amaravati	Nallamaranpatty	41	5571	569	1078	1.89	3.39	1.79

Qmax – Maximum annual peak discharge; *Qm* – Mean annual peak discharge; σ – Standard deviation: *Cv* – Coefficient of variation: *Cs* – Coefficient of skewness; *RL* – Record length. See Figure 1 for location of sites; data source: CWC.

In order to further highlight the extent of variability in peak discharges from one year to other, deviations from mean annual peaks have been shown graphically for a few sites (Fig. 7 and 8). The plots confirm the highly variable nature of flows in the Kaveri Basin. Nevertheless, an interesting fact reflected by the graphs is the positive departures from the mean. The positive departures are much higher than the negative. It is an imperative characteristic of AMS. Further, mean is strongly affected by a few large magnitude floods.

In addition to this, numerous workers have used the Beard's flash flood magnitude index ($FFMI$) to assess the variability of floods measured as an index of flood flashiness (Baker 1977). The $FFMI$ values are computed from the standard deviation of logarithms of AMS as given below:

$$FMM = \sqrt{\frac{\sum X^2}{N-1}} \quad (1)$$

where, $X = Xm - Qm$, Xm – annual maximum event, Qm – mean annual peak discharge, N – number of years of record (X, Xm, and Qm expressed as logarithms to the base of 10).

$FFMI$ values approaching 1.0 indicate a high propensity for flash floods accompanied by geomorphic changes within the basin (Kochel 1988). Nevertheless, the $FFMI$ values observed in the Kaveri River Basin remain moderate. The values range from 0.16 to 0.61 (Tab. 4), with a basin-wide mean of 0.32, which is slightly above the global mean of 0.28 (McMahon et al. 1992; Erskine, Livingstone 1999). The highest value is observed on the Amaravati River at the Nallamaranpatty site which is 0.61. It is attributed to the very high positive departures from the mean annual peak discharge (Fig. 8h). Notably, none of the sites on the mainstream Kaveri River exceed a value of 0.36, suggesting the absence of flash flood events during the period of systematic data collection.

4.2.3. Skewness

The skewness is properly designated as the coefficient of skewness (Cs), which is the utmost widely used measure of moments in geomorphological and hydrological studies of floods. A recognisable fact is that the AMS data are not normally distributed. Thus, it is inevitable to calculate the Cs of the AMS data. The values of Cs for all the discharge gauging sites on the Kaveri River and its major tributaries are positive, extending from 0.55 to 3.39 (Tab. 3). The Cs figures achieved for other large Indian rivers (Sakthivadivel, Raghupathy 1978) are analogous with the Cs values derived for the Kaveri River and its tributaries. The positive Cs values recommend the existence of one or two (or a few) large magnitude floods during the period of systematic observations. However, the value of Cs is dubious when it is derived from less than 50 years of observations (Viessman et al. 1989). In addition to this, the ratio of skewness and coefficient of variation (Cs/Cv) has also been used by some hydrologists to substantiate the gradation of skewness (Shaligram, Lele 1978). The values of this ratio for various gauging sites in the Kaveri Basin fluctuate between 1.29 and 3.40. The highest value of the quotient has been observed for the Kabini River at the

Muthankera site. The values of this quotient for some of the sites on the Tapi River in central India range from 0.93 to 2.84 (Patil et al. 2024b). The Cs/Cv quotients are more than 2.0 for most large Indian rivers (Shaligram, Lele 1978). However, for most of the sites on the Kaveri River and its tributaries, this ratio is less than two except two sites, namely Muthankera on the Kabini River and K.M. Vadi on the Lakshmanathirtha River. The derivation of this quotient, subsequently, verifies that the distribution of AMS for the Kaveri Basin is not very skewed.

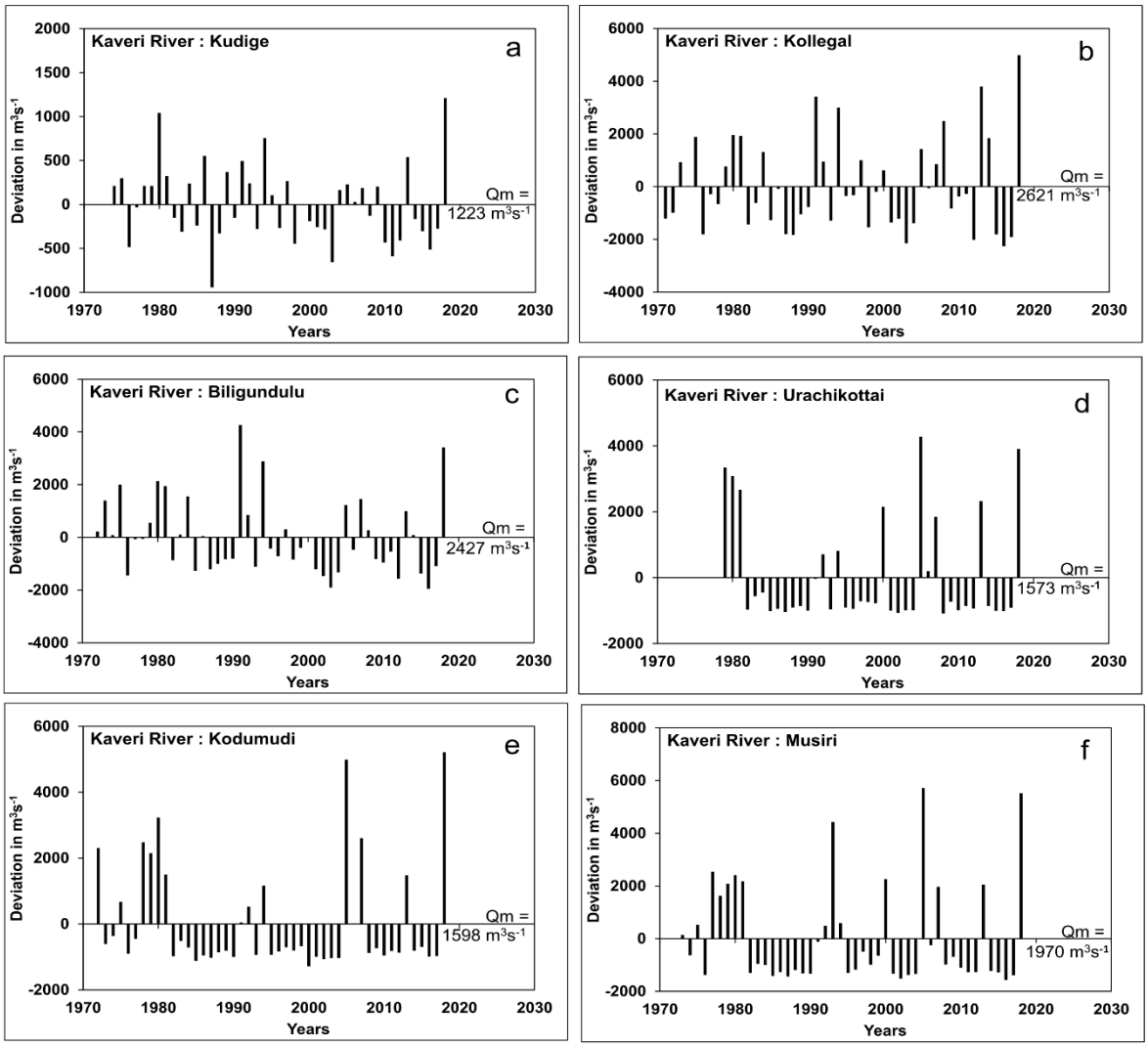

Fig. 7. Departure from mean annual peak discharge on the Kaveri River; See Figure 1 for location of sites.

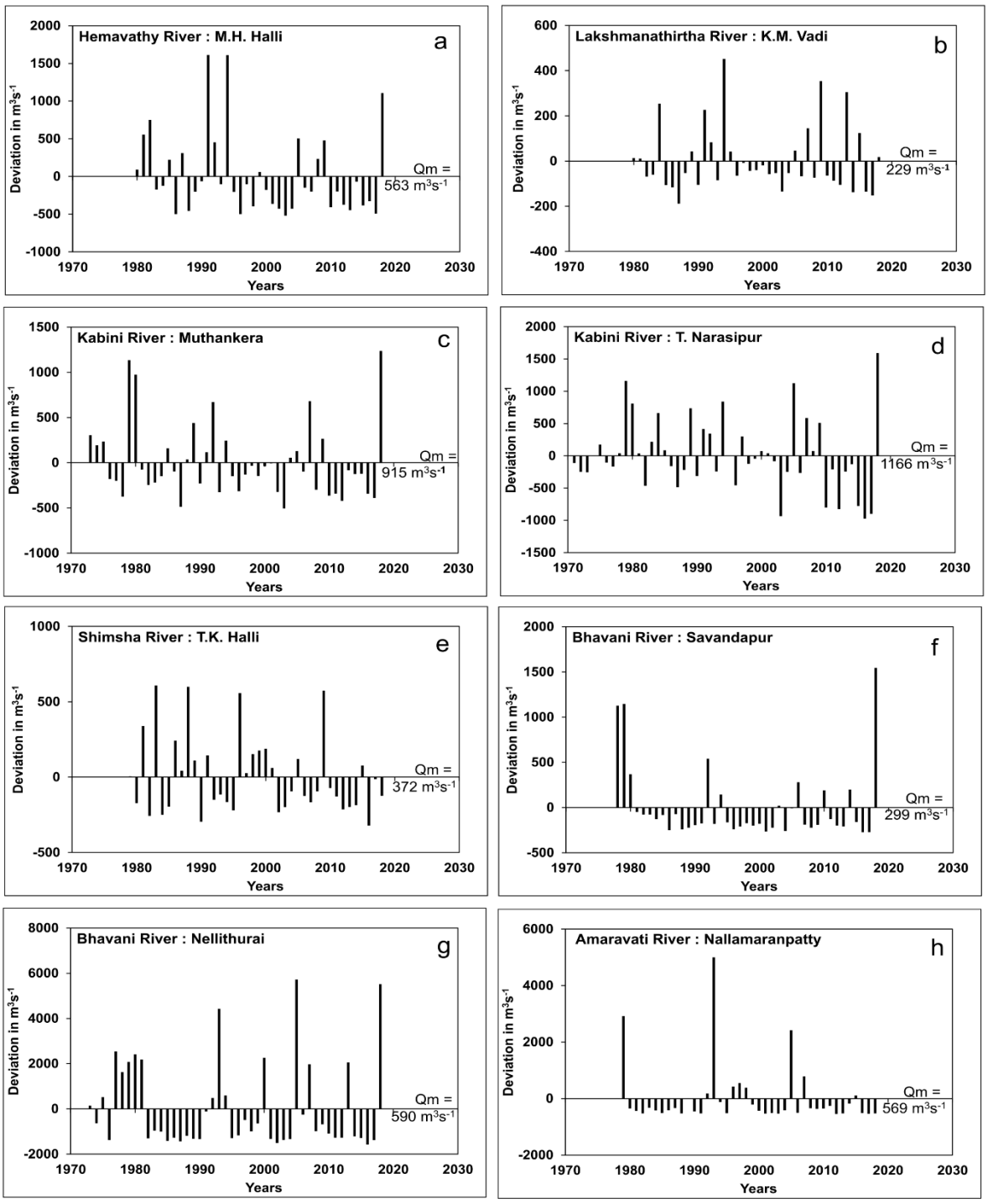

Fig. 8. Departure from mean annual peak discharge on the tributaries of the Kaveri River; See Figure 1 for location of sites.

Table 4. Flash flood magnitude indices of the Kaveri River and its tributaries.

SN	River	Site	Record Length	*FFMI*
1	Kaveri	Kudige	45	0.16
2	Kaveri	Kollegal	48	0.31
3	Kaveri	Biligundulu	47	0.25
4	Kaveri	Urachikottai	40	0.34
5	Kaveri	Kodumudi	47	0.32
6	Kaveri	Musiri	46	0.36
7	Hemavathy	M.H. Halli	39	0.42
8	Lakshmanathirtha	K.M. Vadi	39	0.26
9	Kabini	T. Narasipur	48	0.25
10	Kabini	Muthankera	46	0.16
11	Shimsha	T.K. Halli	40	0.31
12	Bhavani	Savandapur	41	0.44
13	Bhavani	Thengumarahada	40	0.36
14	Bhavani	Nellithurai	39	0.28
15	Noyyal	E-Mangalam	20	0.30
16	Amaravati	Nallamaranpatty	41	0.61
			Mean	0.32

FFMI – Flash flood magnitude index; See Figure 1 for location of sites.

4.2.4. Unit discharge

Unit discharge is an additional significant measure that indicates the likelihood of high magnitude floods on a river (Gupta 1988). The quotient of unit discharge is derived by dividing the maximum annual peak discharge (*Qmax*) with the upstream catchment area (*A*). It provides the water yield (or discharge) per unit basin (drainage) area and is expressed in terms of $m^3s^{-1}km^{-2}$. The unit discharges computed for the sites in the Kaveri Basin vary between 0.02 and 1.71 $m^3s^{-1}km^{-2}$ (Tab. 5). The supreme unit discharge is witnessed on the Kabini River at Muthankera site for the 2018 large magnitude flood. An examination of the unit discharges of the Kaveri and Tapi Basins as a whole are 0.18 and 0.65 $m^3s^{-1}km^{-2}$ respectively (Hire 2000; Patil et al. 2024b). It is interesting to note that the unit discharge of the entire Kaveri Basin (0.18 $m^3s^{-1}km^{-2}$) is very low when compared with other Indian rivers with comparable drainage basin areas.

4.2.5. Discharge-area envelope curve

The highest ever produced flood in a drainage area is commonly presumed to be a magnitude of the prospective flow for geomorphic effectiveness (Costa, O'Connor 1995). Exceptionally high magnitude floods indexed by drainage area or return period are supposed to produce enormous powers – sufficient to cause long-lasting alterations in the river channel and morphology of valley. However, under specified hydro-climatic circumstances there is a higher physical boundary to the large magnitude floods that can be produced (Enzel et al. 1993) and, therefore, the supreme conceivable power that can be created. Consequently, to evaluate the prospect of a basin or region producing an extreme probable uttermost flood, regional envelope curves covering the supreme discharges produced in a region have frequently

been applied to demarcate the expected upper limits to large magnitude floods (Enzel et al. 1993). This graphical and empirical method is established on two assumptions: (1) that there are physical upper bound limits to amount of precipitation to a basin (Enzel et al. 1993) and: (2) the highest flood per unit drainage area in one basin is expected to be generated in neighbouring basins having analogous hydro-geomorphic circumstances (Mutreja 1995).

Table 5. Unit discharges of the Kaveri River and its major tributaries.

SN	River	Site	Area [km^2]	*Qmax* [m^{3}s^{-1}]	Unit discharge [m^{3}s^{-1}km^{-2}]
1	Kaveri	Napoklu	335	6	0.02
2	Kaveri	Kudige	1934	2435	1.26
3	Kaveri	Kollegal	21082	7609	0.36
4	Kaveri	Biligundulu	36682	6688	0.18
5	Kaveri	Urachikottai	44100	5855	0.13
6	Kaveri	Kodumudi	53233	6808	0.13
7	Kaveri	Musiri	66243	7690	0.12
8	Kaveri	Chunchunkatte	2995	2920	0.97
9	Kaveri	Bhavani Bridge	49876	5862	0.12
10	Kaveri	KRS Dam	10,619	5918	0.56
11	Kaveri	Upper anicut	67301	13097	0.19
12	Kaveri	Grand anicut	67769	13451	0.20
13	Kaveri	Mettur Dam	42217	12912	0.31
14	Kaveri	Kattalai Barrage	66243	7690	0.12
15	Kaveri	Tiruchilapalli	67769	13000	0.19
16	Hemavathy	M.H. Halli	3050	2172	0.71
17	Hemavathy	Akkihebbal	5236	2185	0.42
18	Hemavathy	Sakleshpur	617	760	1.23
19	Yagachi	Thimmanahalli	1010	393	0.39
20	Kabini	T. Narasipur	7000	2757	0.39
21	Kabini	Muthankera	1260	2150	1.71
22	Shimsha	T.K. Halli	7890	980	0.12
23	Arkavathi	T. Bekuppe	3500	424	0.12
24	Lakshmanathirtha	K.M. Vadi	1330	681	0.51
25	Bhavani	Savandapur	5776	1845	0.32
26	Bhavani/Moyar	Thengumarahada	1370	653	0.48
27	Bhavani	Nellithurai	1475	1476	1.00
28	Bhavani	Bhavanisagar Dam	4199	2939	0.70
29	Noyyal	E- Mangalam	3386	175	0.05
30	Amaravati	Nallamaranpatty	9080	5571	0.61
31	Noyyal	Alandurai	156	1.56	0.01
32	Gandhayar	Gandhavayal	91	49	0.54
33	Sarabenga	Thevur	1248	168	0.13
34	Chittar	Sevanur	258	59	0.23
35	Thoppaiyar	Thoppur	362	61	0.17
36	Palar	Kudlur	709	77	0.11
37	Chinnar	Hogenakkal	1636	251	0.15
38	Suvarnavathi	Bendrahalli	1900	510	0.27
	Kaveri Basin	**-**	**81155**	**14716**	**0.18**

A = Catchment area; Qmax = Maximum annual peak discharge; See Figure 1 for location of sites.

The discharge-area envelope curve for the Kaveri Basin has been constructed with the support of maximum annual peak discharge (*Qmax*) data and upstream catchment area (*A*) available for more than 38 discharge gauging sites in the Kaveri Basin (Tab. 5). The curve is represented in Figure 9. In addition to this, the world envelop curve constructed by Baker (1995) is portrayed in the same diagram for comparison. An assessment with Baker's world envelope curve (Fig. 9) clearly demonstrates that the peak discharges on the Kaveri River and its tributaries are comparatively much smaller in magnitude than the floods produced for the similar drainage basin areas in the other parts of the world. However, a cursory inspection of the envelope curve of southern Indian rivers indicates that the drainages in southern India (including Kaveri) produced similar flood peak discharges. The analysis, therefore, clearly demonstrates that under given meteorologic, hydrologic and geomorphic circumstances, an exceptionally high magnitude of discharges cannot be generated in the Kaveri River and its tributaries. However, further investigations are necessary to find out the floods of greater magnitude that have occurred in the Kaveri Basin.

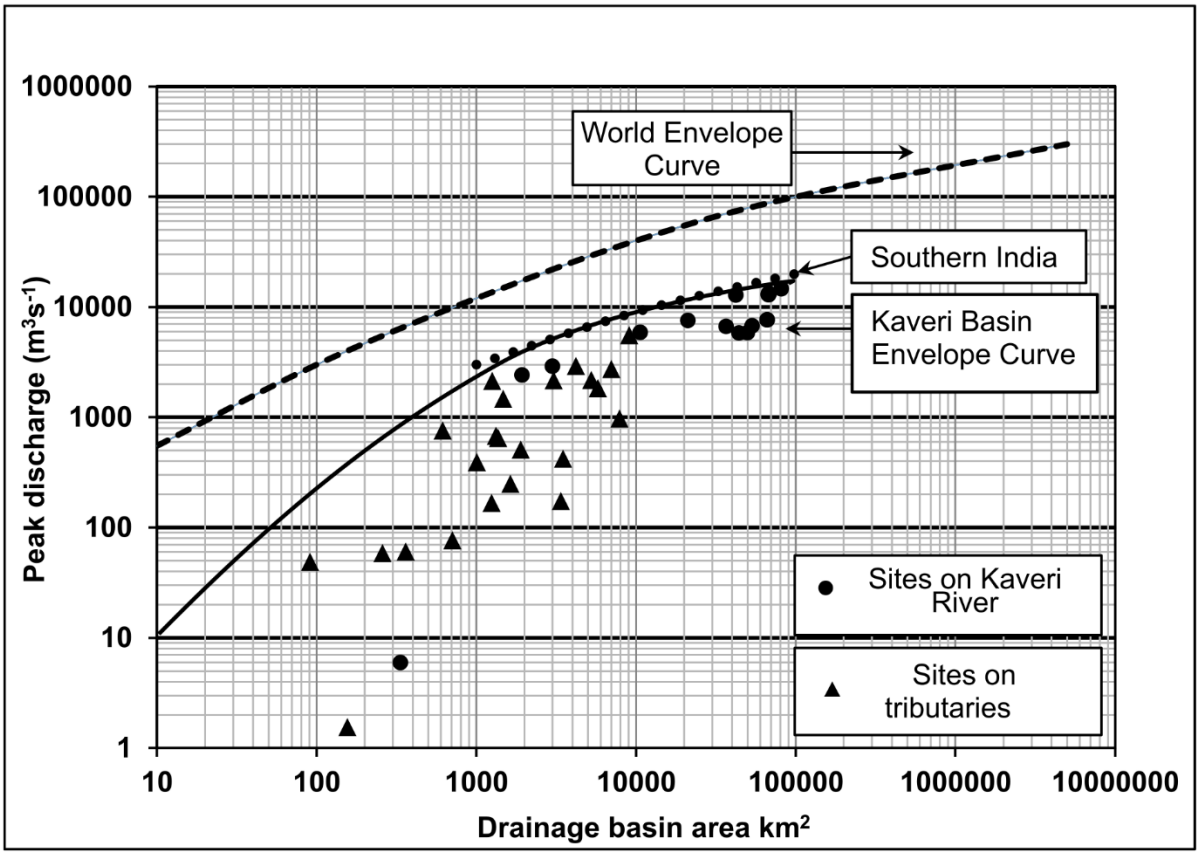

Fig. 9. Discharge-area envelope curve of the Kaveri Basin.

4.2.6. Flood hydrograph analysis

In order to recognize the short-term deviations in flood discharge it is necessary to investigate the nature of the increase and decrease of water level or discharge at-a-station throughout the occurrence of floods. It is accomplished by construction and investigation of flood hydrographs. The flood hydrographs are

available for upstream locations such as Kudige, Kollegal, middle reaches namely Biligundulu, Urachikottai, and downstream sites viz. Kodumudi and Musiri on the Kaveri River (Fig. 1). Figure 10 (a-f) shows the flood hydrographs of one of the large-magnitude flood events, i.e. the 2018 flood documented at the gauging sites mentioned above on the Kaveri River. The diagrams illustrate that the specific high magnitude flood events have occurred for a long duration: ranging from 7 to 15 days. This is anticipated in an elongated basin such as the Kaveri. Further, this suggests that the large magnitude flood events on the Kaveri River are long-lasting events and consequently reveal geomorphic efficiency.

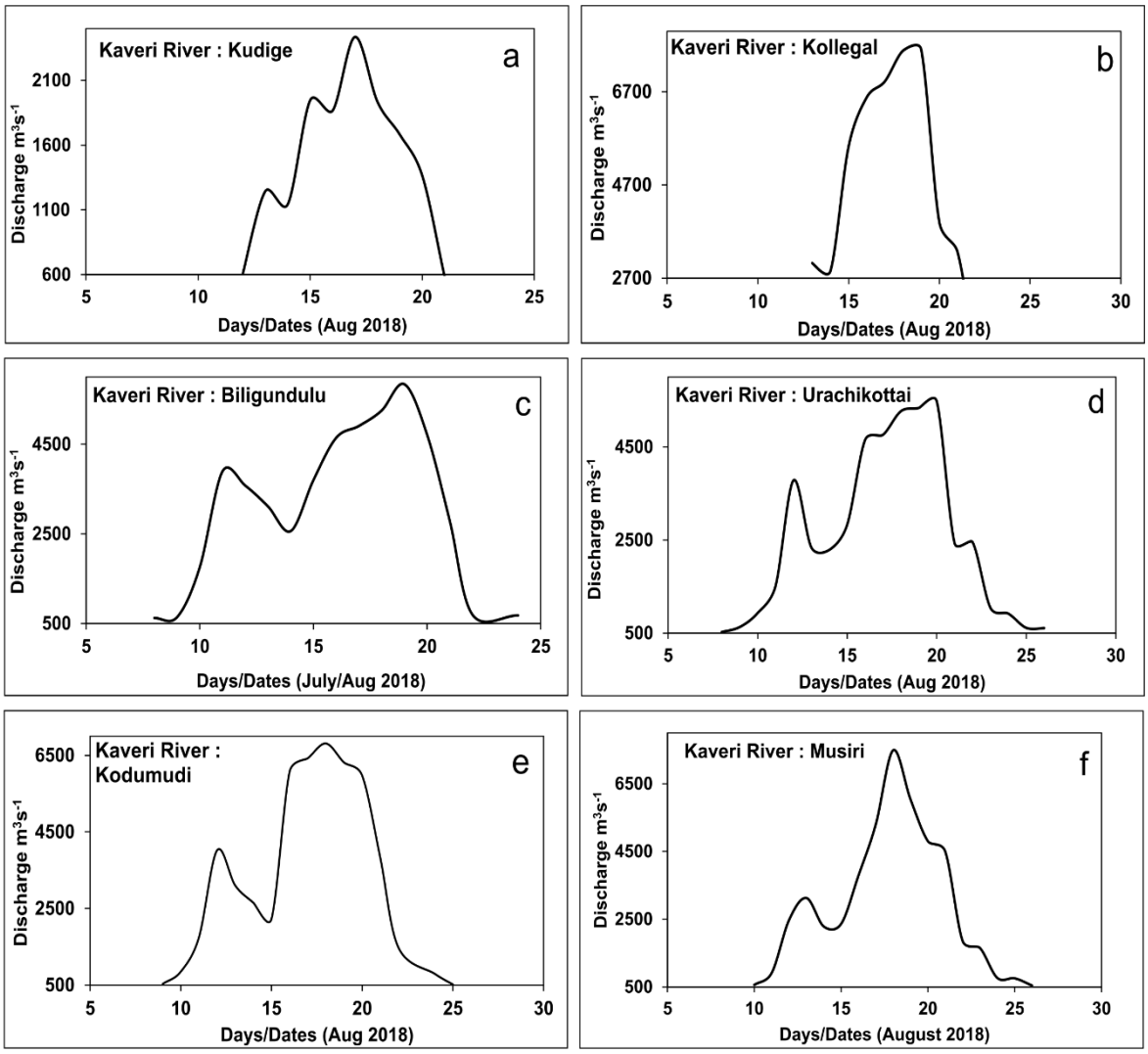

Fig. 10. Flood hydrographs of the Kaveri River; See Figure 1 for location of sites.

5. Conclusions

The fluvial and flood regime investigations of the Kaveri River and its tributaries meaningfully indicate that the monsoon regime and release of water from dams play a role of considerable importance in determining the river regime conditions of the river under study. The seasonal fluctuations in the discharge of the river and its tributaries reflect the distribution of monsoon rainfall. The mean annual hydrographs of the Kaveri River and its tributaries indicate a simple discharge regime with one

pronounced peak. Over 60% to 95% of the annual flows occur in the monsoon season and, during the dry season, the flow magnitude dwindles up to 5%. The time series plots of the annual maximum series data reflect high as well as low interannual variability. Slightly high variability is also indicated by the values of coefficient of variation (0.36 to 1.89) and the flash flood magnitude index (0.16 to 0.61). In general, the maximum annual peak discharges are 2 to 10 times higher than the mean annual maximum discharges. All these indices indicate that the river experiences significant geomorphic work during large floods. The positive Cs values recommend the existence of one or two (or a few) large magnitude floods during the period of systematic observations on the Kaveri River and its tributaries. The unit discharge of the entire Kaveri Basin (0.18 $m^3s^{-1}km^{-2}$) is much less when matched with other Indian rivers with comparable drainage basin areas. The analysis of the envelope curve clearly demonstrates that, under given meteorologic, hydrologic and geomorphic circumstances, an exceptionally high magnitude discharge cannot be generated on the Kaveri River and its tributaries. The study of flood hydrographs illustrates that the specific high magnitude flood events occur for a long duration, ranging from 7 to 15 days. Thus, the investigation indicates that the fluvial and flood regime characteristics of the Kaveri River and its tributaries are controlled by monsoonal rainfall pattern and by the release of water from dams.

Funding

1. Anusandhan National Research Foundation (ANRF), formerly, Science and Engineering Research Board (SERB)), Department of Science and Technology (DST), Government of India (Project File No. CRG/2022/000823 dated September 1, 2023).
2. ICSSR Centrally-Administered Full-Term Doctoral Fellowship for 2024–25 (ICSSR/RFD/24-25/GEOG/GEN/144, dated February 6, 2025).

Acknowledgements

The authors are grateful to Anusandhan National Research Foundation (ANRF), formerly Science and Engineering Research Board (SERB)), Department of Science and Technology (DST), Government of India for financial support to conduct this research work (Project File No. CRG/2022/000823 dated September 1, 2023). This study is also supported by the ICSSR Centrally-Administered Full-Term Doctoral Fellowship for 2024-25 (ICSSR/RFD/24-25/GEOG/GEN/144, dated February 6, 2025), awarded to Smita Pagare (First Author). The authors are thankful to Central Water Commission, New Delhi for providing hydrological data. The authors also gratefully acknowledge the support extended by the research centre at HPT Arts and RYK Science College, Nashik – 422005, India, affiliated with Savitribai Phule Pune University, for providing the academic infrastructure and resources vital to the successful completion of this research.

References

Baker V.R., 1977, Stream-channel response to floods, with examples from central Texas, Geological Society of American Bulletin, 88 (8), 1057-1071, DOI: 10.1130/0016-7606(1977)88<1057:SRTFWE>2.0.CO;2.

Baker V.R., 1994, Geomorphological understanding of floods, Geomorphology, 10 (1-4), 139-156, DOI: 10.1016/0169-555X(94)90013-2.

Baker V.R., 1995, Global palaeohydrological change, Quaestiones Geographicae, 4, 27-35.

Baker V.R., Kochel R.C., Patton P.C., 1988, Flood Geomorphology, Wiley.

Brauman K.A., Daily G.C., Duarte T.K., Mooney H.A., 2007, The nature and value of ecosystem services: an overview highlighting hydrologic services, Annual Review of Environment and Resources, 32, 67-98, DOI: 10.1146/annurev.energy.32.031306.102758.

Charlton R., 2008, Fundamentals of Fluvial Geomorphology, Routledge.

Chow V.T., 1964, Handbook of Applied Hydrology, McGraw-Hill, New York.

Costa J.E., O'Connor J.E., 1995, Gemorphologically effective foods, [in:] Natural and Anthropogenic Influences in Fluvial Geomorphology, Geophysical Monograph, 89, 45-56.

CWC, 2020, Water Year Book 2018-19: Cauvery and Southern Rivers Circle, Central Water Commission, Ministry of Jal Shakti, Government of India.

Ekka A., Keshav S., Pande S., Zaag P., Jiang Y., 2022, Dam-induced hydrological alterations in the upper Cauvery river basin, Journal of Hydrology: Regional Studies, 44, DOI: 10.1016/j.ejrh.2022.101231.

Enzel Y., Ely L.L., House P.K., Baker V.R., 1993, Palaeoflood evidences for a natural upper bound to flood magnitudes in the Colorado Basin, Water Resources Research, 29 (7), 2287-2297, DOI: 10.1029/93WR00411.

Erskine W.D., Livingstone E.A., 1999, In-channel benches: the role of floods in their formation and destruction on bedrock-confined rivers, [in:] Varieties of Fluvial Form, A.J. Miller, A. Gupta (eds.), John Wiley and Sons Ltd., Chichester, 445-475.

Gopal B., 2016, A conceptual framework for environmental flows assessment based on ecosystem services and their economic valuation, Ecosystem Services, 21 (Part A), 53-58, DOI: 10.1016/j.ecoser.2016.07.013.

Goswami D.C., 1985, Brahmaputra River, Assam, India: Physiography, basin denudation, and channel aggradation, Water Resources Research, 21 (7), 959-978, DOI: 10.1029/WR021i007p00959.

Gupta A., 1988, Large floods as geomorphic events in the humid tropics, [in:] Flood Geomorphology, V.R. Baker, R.C. Kochel, P.C. Patton (eds.), Wiley, New York, 301-315.

Gupta A., 1995, Magnitude, frequency, and special factors affecting channel form and processes in the seasonal tropics, [in:] Natural and Anthropogenic influences in the Fluvial Geomorphology, J.E. Costa, A.J. Miller, K.W. Potter, P. Wilcock (eds.), American Geophysical Union, Washington, DC, Monograph 89, 125-136.

Gupta A., Kale V.S., Rajaguru S.N., 1999, The Narmada River, India, through space and time, [in:] Varieties of Fluvial Form, A.J. Miller, A. Gupta (eds.), John Wiley and Sons Ltd., Chichester, 113-341.

Hire P.S., 2000, Geomorphic and Hydrologic Studies of Floods in Tapi Basin, PhD thesis. University of Pune, Pune, India.

Kale V.S., Ely L.L., Enzel Y., Baker V.R., 1994, Geomorphic and hydrologic aspects of monsoon floods on the Narmada and Tapi Rivers in central India, Geomorphology, 10 (1-4), 157-168, DOI: 10.1016/0169-555X(94)90014-0.

Kale V.S., Sengupta S., Achyuthan H., Jaiswal M.K., 2014, Tectonic controls upon Kaveri River drainage, cratonic Peninsular India: Inferences from longitudinal profiles, morphotectonic indices, hanging valleys and fluvial records, Geomorphology, 227, 153-165, DOI: 10.1016/j.geomorph.2013.07.027.

Kochel R.C., 1988, Geomorphic impact of large floods: review and new perspectives on magnitude and frequency, [in:] Flood Geomorphology, V.R. Baker, R.C. Kochel, P.C. Patton (eds.), Wiley, New York, 169-187.

Leopold L.B., Wolman M.G., Miler J.P., 1964. Fluvial Process in Geomorphology. Freeman, San Francisco.

McMahon T.A., Finlayson B.L., Haines A.T., Srikanthan R. (eds.), 1992, Global runoff – Continental Comparisons of Annual Flows and Peak Discharges, Catena Paperback, 166 pp.

Mutreja K.N., 1995, Applied Hydrology, Tata McGraw-Hill Publishing Company Ltd., New Delhi.

Pagare S.R., Hire P.S., Patil A.D., 2025, Magnitude and frequency analyses of floods on the Kaveri River of the Southern India by using Gumbel Extreme Value type I probability distribution, Hydrospatial Analysis, 9 (1), 1-9, DOI: 10.21523/gcj3.2025090101.

Patil A.D., 2017, Bedrock Channel of the Par River: Its Forms and Processes, PhD thesis. Tilak Maharashtra Vidyapeeth, Pune, India.

Patil A.D., Hire P.S., Bramhankar G.W., Khandare P.R., Gunjal R.P., Anwat V.K., 2024a, Flood meteorology, hydrology, and geomorphology of the Upper Godavari River, Western India, Meteorology Hydrology and Water Management, *12* (1), 65-82, DOI: 10.26491/mhwm/191702.

Patil A.D., Pawar U.V., Bramhankar G.W., Hire P.S., 2024b, Flood hydrology, hydraulics, and hydrodynamics of the Tapi River, Western India, [in:] Rivers of India, S. Kanhaiya, S. Singh, A. Dixit, A.K. Singh (eds.), Springer, 213-232, DOI: 10.1007/978-3-031-49163-4_13.

Pawar U.V., 2019, An Analytical Study of Geomorphological, Hydrological, and Meteorological Characteristics of Floods in the Mahi River Basin: Western India, PhD Thesis, Tilak Maharashtra Vidyapeeth, Pune, India.

Ramaswamy S.M., 2006, Remote sensing and active tectonics of South India, International Journal of Remote Sensing, 27 (20), 4397-4431, DOI: 10.1080/01431160500502603.

Renofalt B.M., Jansson R., Nilsson C., 2010, Effects of hydropower generation and opportunities for environmental flow management in Swedish riverine ecosystems, Freshwater Biology, 55 (1), 49-67, DOI: 10.1111/j.1365-2427.2009.02241.x.

Sakthivadivel R., Raghupathy A., 1978, Frequency analysis of floods in some Indian rivers, Hydrology Review, 4, 57-67.

Schumm S.A., 1977, The Fluvial System, John Wiley and Sons, New York.

Seth S.M., 1998, Flood hydrology and flood management in India, [in:] Floods Studies in India, V.S. Kale (ed.), Geological Society of India, Memoir, 41, 155-172.

Shaligram V.M., Lele V.S., 1978, Analysis of hydrologic data using Pearson Type III distribution, Nordic Hydrology, 9, 31-42.

Sharma A., Rajamani V., 2001, Weathering of charnockites and sediment production in the catchment area of the Cauvery River, southern India, Sedimentary Geology, 143 (1-2), 169-184, DOI: 10.1016/S0037-0738(01)00102-6.

Shaw E.M., 1988, Hydrology in Practice, VanNostrand Reibhold Int. Co. Ltd., London.

Vaidyanadhan R., 1971, Evolution of the drainage of Cauvery in South India, Journal Geological Society of India 12 (1), 14-23, DOI: 10.17491/jgsi/1971/120102.

Vaithiyanathan P., Ramanathan Al., Subramanian V., 1992, Sediment transport in the Cauvery River basin: sediment characteristics and controlling factors, Journal of Hydrology 139 (1-4), 197-210, DOI: 10.1016/0022-1694(92)90202-7.

Valdiya K.S., 2001, Tectonic resurgence of the Mysore plateau and surrounding regions in cratonic Southern India, Current Science, 81 (8), 1068-1089.

Viessman W., Lewis G.L., Knapp J.W., 1989, Introduction to Hydrology, Happer and Row Publishers, Singapore.

Ward R., 1978, Floods. A Geographical Perspective, The MacMillan Press Ltd., London

Wells N.A., Dorr J.A., 1987, Shifting of the Kosi River, Northern India, Geology, 15 (3), 204-207, DOI: 10.1130/0091-7613(1987)15<204:SOTKRN>2.0.CO;2.

Wohl E.E., 1992, Bedrock benches and boulder bars: Floods in the Burdekin Gorge of Australia, Geological Society of America Bulletin, 104 (6), 770-778, DOI: 10.1130/0016-7606(1992)104<0770:BBABBF>2.3.CO;2.

Wolman M.G., Miller J.P., 1960, Magnitude and frequency of forces in geomorphic processes, Journal of Geology, 68 (1), 54-74, DOI: 10.1086/626637.

Analysis of rainfall and windflow patterns in southwestern Nigeria

Elisha Ademola Adeleke

University of Ilorin, Nigeria

Abiodun Daniel Olabode

Adekunle Ajasin University, Nigeria

Abstract

The fluctuations in the observed rainfall pattern is a great concern for the rainfed-based system in Nigeria. In Southwestern Nigeria, for example, it has become difficult to predict rainfall activities in most cities and villages in the recent times. This study is focused on the analysis of rainfall and wind-flow patterns in Southwestern Nigeria. Secondary data on rainfall and wind-flow were collected from weather stations across Ikeja, Ibadan, Abeokuta, Osogbo and Akure between the years 1971 and 2020. Data were subjected to descriptive statistics with the results presented using wind flow maps. Results revealed that the recorded mean seasonal rainfall amounts of 303 mm in Ikeja, followed by Akure (229 mm), Osogbo (178 mm), and Ibadan (169 mm), were indications of local weather patterns like the influence of sea breeze that usually results in rainfall variability. The South-westerly monsoon is moisture -laden and hence a rain-bearing wind, which blows inland from the Atlantic Ocean. The study also observed the weakness of the wind during the December, January and February (DJF) months, due to the local influence of the dry harmattan wind that blows northerly from the opposite direction. This period of dryness has been accounted for in the low rainfall amount recorded in most stations. especially in Ibadan at this time. Primarily, heat, moisture and aerodynamic indices were found to be the primary control factors of rainfall patterns in the study area. It is therefore recommended that wind flow direction is an important key element to guide decisions on human outdoor activities, travel plans and agricultural practices.

Keywords

Climate, rainfall pattern, wind flow maps, dry harmattan, southwestern Nigeria.

Submitted 24 May 2025, revised 7 September 2025, accepted 8 September 2025

DOI: 10.26491/mhwm/210420

1. Introduction

The climate of Nigeria spreads across the distance of 1,100 km of the south and the north of the country, thus, covers many of the climatic belts of West Africa (Iloeje 1981). This climate is dominated by the influence of three wind currents that include: the tropical maritime (mT) air mass, the tropical continental (cT) air mass and the equatorial easterlies (Ojo 1977). The first air mass originates from the southern high-pressure belt located off the Namibian coast and, in its path, picks up moisture from over the Atlantic Ocean and is thus wet. The second air mass (cT) originates from the high-pressure belt north of the Tropic of Cancer. This latter air mass picks up little moisture along its path and is thus dry. These first two air masses (mT and cT) meet along a slanting surface called the Inter Tropical Discontinuity (ITD). The third air mass (equatorial easterlies) is a rather erratic cold air mass, which comes from the east and flows in the upper atmosphere along the ITD.

Adejuwon (2012) noticed that, apart from the contribution of ITD to rainfall distribution in South-western Nigeria, other factors controlling rainfall in the area include the ocean-atmosphere interaction, relief, line squall and the local features. Ifabiyi and Omoyosoye (2011) also observed that rainfall within the tropical regions is highly variable, and this accounts for the uneven distribution of rainfall frequency, amount, duration, density and some other variables throughout Nigeria. In another study, Odjugo (2010)

observed that there has been a statistically significant increase in precipitation and air temperatures in vast major cities in Nigeria. Eludoyin (2009) studied monthly rainfall distribution in Nigeria between 1985-1994 and 1995-2004 and noticed some fluctuations in most months over the decades. Igwenagu (2015) also observed this fluctuation as measures of irregularity in the patterns of rainfall in Enugu state, Nigeria. She observed a clear decline in patterns of rainfall from the year 2000 to 2001 and a slight increase from 2002 to 2003. The trend increased remarkably from 2004 to 2010 with a peak being observed in 2006. Ayansina and Ogunbo (2009) investigated the seasonal rainfall variability in the Guinea savannah part of Nigeria and concluded that rainfall variability continues to be on the increase as an element of climate change. Olaniran (2002) opined that the rainfall onset (start of rain) has been progressively delayed since 1968 over southern Nigeria and this has been further corroborated by a significant decline in April rainfall.

In Benin City, Nigeria, Ikhile and Aifesehi (2011) observed that rainfall in the decade 1961-2000 exhibited distinct variations, with the first decades showed double maxima of rainfall with an August break. In the fourth decade (1991-2000), the August break was absent with the August months recording generally higher rainfall values than all the other decades. This means that the normal trend was reversed in this decade. Even the December months were very wet. January was generally the driest month with a total of 682 mm of rain between 1960 and 2000. July was the wettest month with a total of 14 975 mm of rainfall between 1961 and 2000.

However, Babatolu (2002) noticed that rainfall distribution of Ondo during the period of study (1961-2000) showed wide variability. The highest rainfall figure in the decade was recorded in 1963 (2,441 mm) and the lowest was recorded in 1997 (1,217 mm). The rains decreased generally in the last decade (1991-2000), meaning that rainfall distribution along the axis of Ondo and Benin is quite varied (Ikhile, Aifesehi 2011). However, Olaniran (2002) agreed that the likelihood of flooding in the southwestern Nigeria is as a result of abundant of rainfall received by the region especially with Ondo and Ado flooding in 1999. He further explained that flooding is common in these areas in the month of July as evidence that the area is experiencing normal rainfall but not in rainfall frequency.

Olaniran (2002) concluded that there has been a progressive early retreat of rainfall over Nigeria for up to half a century now, and that this is consistent with this pattern of decline in the frequency of rainfall. This pattern is as a result of noticeable changes in the beginning and end of the rainy season in recent times in Nigeria. Odjugo (2010), Oguntude et al. (2012) separately reported that spatial and temporal variations in temperature were noticed in Nigeria where air temperature has been on the increase gradually since 1901 and with a noticeable increase from 1970. Igwenagu (2015) found that the average annual rainfall in coastal areas of Enugu is around 2000 mm because of heavy rainfall during the rainy season.

The coastal regions of West Africa (areas around Calabar) are a continuously rainy area, where there are some seasonal variations in rainfall but where no real dry season occurs. This is followed by a region where two rainy seasons and two dry periods alternate. The length and intensity of the two major rainy and two dry seasons are rarely the same. In the northern part of West Africa, only a short rainy season and a long dry season occur.

Rainfall decreases, both in duration and amount, from the coast to the interior except where altitudinal effects create islands of higher rainfall (e.g. Jos Plateau). The coastal areas receive over 4000 mm spread over 8-10 months while the extreme north receives less than 250 mm spread over 3 to 4 months. The length of each season however varies from place to place depending on the proximity from the sea (Oyewo 2005)

Wind plays a great role in the formation of rainfall in Nigeria; the direction of wind blow determines the rainfall pattern, which majorly in moist-rich environments with moist air mass, thus leading to rainfall. Moreover, the process of adiabatic cooling and condensation is an essential factor of rainfall (Bravar, Kavvas 1991; Christopherson 2012). As it relates to other element of weather, wind direction has been changing with climate change. The direction of wind has been shifting from normal to abnormal over particular periods of time (Christopherson, Birkeland 2017; Davy et al. 2018). In some prevailing conditions, changes in wind pattern can bring about rainfall or drought conditions. Thus, observing the direction of wind could help in determining the nature of rainfall over a period of time.

The selection of Southwestern Nigeria for this study enhances the understanding of climate patterns in most of the related environment in Nigeria and in the world at large. This current research examines the analysis of rainfall and wind-flow patterns in Southwestern Nigeria with a view to determining the best way to adapt to the impact of climate change on rainfall fluctuation.

2. Materials and methods

Southwestern Nigeria is a prominent region in the country. It is located roughly between longitudes 2°31' and 6°00' East and latitudes 6°21' and 8°37' North. This region comprises six states and their capitals: Lagos (Ikeja), Ogun (Abeokuta), Oyo (Ibadan), Osun (Osogbo), Ondo (Akure), and Ekiti (Ado-Ekiti) (Fig. 1). This location is dominated by the Yoruba-speaking people of Nigeria with some high levels of related indigenous socio-economic activities that include agriculture. The agricultural practices are dependent of the rain-fed cultivation of both cash and food crops. However, the vegetation and soil types vary significantly as it depends on prevailing environmental dynamos.

Rainfall and wind flow data from the study area were collected from five major weather stations across Ikeja, Ibadan, Abeokuta, Osogbo and Akure between 1971 and 2020. The selection of the study locations and the observed data periods were based on the availability of/and accessibility to recorded climate data. These seasonal climatic data were subjected to descriptive statistics with their results presented through charts and wind flow maps. Geographical Information System application (Arc GIS 10.1) was used to map out the patterns of wind direction within the study area. The application's capability to perform image interpolation and rasterization is one of its relevant key components in this study. The interpolation capability of GIS helped in adjusting image resolution and quality, while rasterization converted vector graphics into a pixel-based format. The obtained mean annual value of the climatic variables was used to map out the proportion of the variable in each weather station such that the thicker in colouration obtained, the higher the concentration of the variable in the station. Wind direction in this study was typically reported using the cardinal directions (north, east, south, west) and their intermediate points.

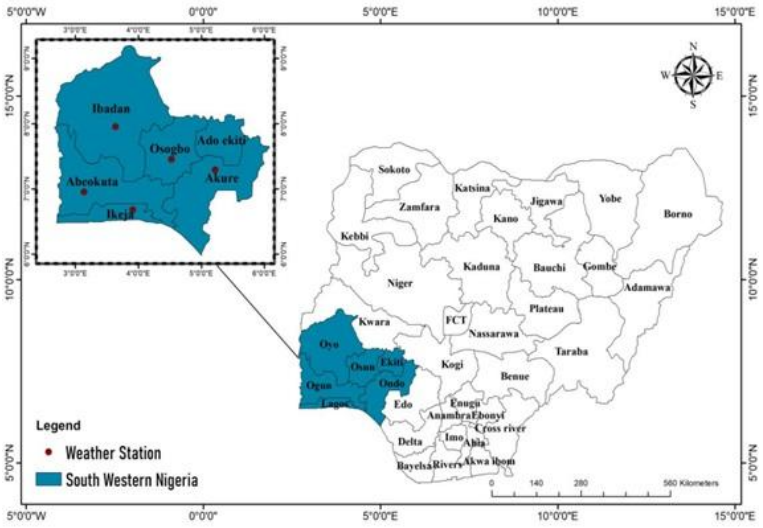

Fig. 1. Nigeria map showing Southwestern and locations of weather stations.

3. Results

3.1. Seasonal rainfall data in the Southwestern Nigeria

It was observed that Southerly, Westerly and South-westerly wind streams were the dominant wind flow pattern over the entire study area. These wind flows encountered some micro- and mesoscale motions that often refer to disturbances or perturbation in the region. The disturbances exerted measures of influence on rainfall amounts recorded over four major seasons considered in this study. These seasons are: December-January-February (DJF), March-April-May (MAM), June-July-August (JJA) and September-October-November (SON) (Fig. 2). The mean seasonal rainfall amount in the decades during the period of study (1971-2020) was presented in Table 1. The South-westerly monsoon is moisture laden and hence a rain- bearing wind which blows inland from the Atlantic Ocean; as it blows inland, its influence on producing rain weakens. The weakness of this wind aggravates during the December, January and February (DJF) months. These are dry seasons because of the local influence of the dry harmattan wind which blows via the northerly wind from the opposite direction. This accounts for the low rainfall amount recorded in most stations, especially in Ibadan at this time. Ibadan ought to receive more rainfall than the Akure and Osogbo stations because of its proximity to the Atlantic Ocean. In the June, July and August (JJA) season, the South-westerly is strengthened mainly because of the absence of the desiccating wind and it is able to push inland. This accounts for the higher rainfall amount recorded in every station as compared with the December, January and December (DJF) season.

It is important to note that during the March, April and May (MAM) season, spatial patterns of variation change slightly from the previous occurrence. Based on the record, the decade 1991-2000 was wetter than 1981-1990. Ibadan ceased to be the driest during the first two decades, especially in the seasons of DJF and MAM. However, variation in rainfall might be explained by the orographic characteristics of Akure and Osogbo, which were situated on a higher ground level. This finding is supported with the outcome of Barbro and Deliang (2003) that, on the upwind side of a mountain, precipitation increases; while less rainfall is recorded on the leeward side.

Table 1. Mean seasonal rainfall amounts in decades between 1971-2020. Source: Author's computation (2023).

Decade	Stations	DJF	MAM	JJA	SON
1971-1980 (Dry decade)	Ikeja	20.76	171.51	302.98	136.36
	Ibadan	11.68	132.50	168.64	113.10
	Abeokuta	0	0	0	0
	Osogbo	20.26	124.77	178.03	119.42
	Akure	19.36	133.41	229.30	142.99
1981-1990 (Wet decade)	Ikeja	33.97	133.10	174.05	100.58
	Ibadan	13.14	132.81	135.89	92.98
	Abeokuta	0	0	0	0
	Osogbo	9.98	117.64	138.10	112.84
	Akure	25.26	145.33	208.98	123.98
1991-2000 (Dry decade)	Ikeja	16.50	121.26	198.82	100.83
	Ibadan	12.14	108.79	182.95	107.14
	Abeokuta	15.65	116.05	150.88	77.44
	Osogbo	12.53	118.58	157.55	111.99
	Akure	19.98	162.36	197.41	108.88
2001-2010 (Dry decade)	Ikeja	25.10	136.97	187.30	129.95
	Ibadan	20.01	118.62	176.64	105.95
	Abeokuta	14.31	100.72	167.84	85.78
	Osogbo	12.66	116.07	177.67	117.90
	Akure	15.19	145.91	230.41	130.74
2011-2020 (Wet decade)	Ikeja	27.64	162.22	214.27	124.83
	Ibadan	17.50	133.70	177.64	103.37
	Abeokuta	10.65	119.64	168.14	76.52
	Osogbo	14.99	135.01	165.49	131.37
	Akure	19.46	158.44	240.16	111.03

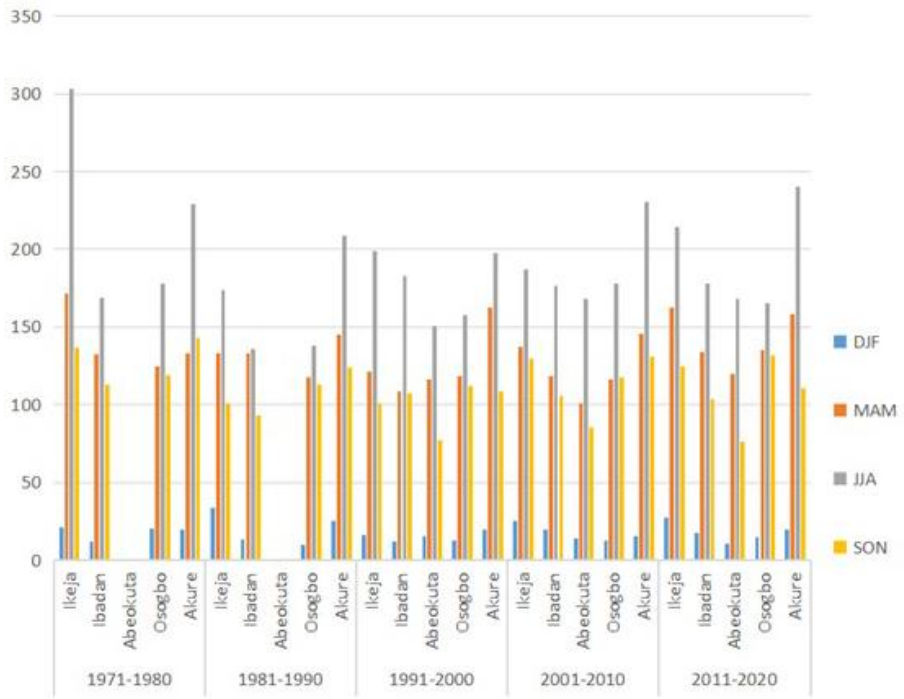

Fig. 2. Rainfall data in selected Nigerian Southwestern cities from 1971 to 2020.

3.2. Wind flow direction and the Nigerian rainfall system between 1971-2020

The South-westerly monsoon wind was consistent with the DJF season over Ikeja, Ibadan, Akure, while the extension of strong westerly wind components pushing from the coastal area were much more prevalent in Osogbo with a relatively stable atmosphere (Fig. 3). High wind speeds, fluctuating between 4.14-4.86 m/s, was recorded in Akure. The DJF rainfall amounts of 21 mm, 12 mm, 20 mm, 19 mm were recorded for Ikeja, Ibadan, Osogbo and Akure respectively. Osogbo's weather conditions were fairly good in the season of DJF which could be the reason for the station recording rainfall of around 20 mm in the decade.

The strong South-westerly wind stream was prominent and advanced in the season of JJA, being the peak of the annual rainfall amount. In this season, Ikeja received a mean seasonal rainfall amount of 303 mm while 169 mm in Ibadan, 178 mm in Osogbo and 229 mm in Akure were recorded respectively (Tab. 1). This implies that some local weather patterns like sea breeze and urban heat island influence had contributed to the high amount of rainfall recorded in Ikeja in JJA season compared to other stations. Ayoade (1988; 2004) and Omogbai (2010) agreed with this result – that maritime air mass is prominently alert during the season of JJA – which accounts for more rainfall at this time.

Tropical westerly jet streams majorly characterized the season of MAM in all the meteorological stations. During the season, Ikeja recorded 172 mm mean seasonal rainfall amounts with 133 mm in Ibadan, 124 mm in Osogbo and 133 mm in Akure. The close proximity of Ikeja to the Atlantic Ocean with the influence of strong southerly winds and local sea breezes must have been the main reasons for the area recording a remarkable amount of rainfall in the season.

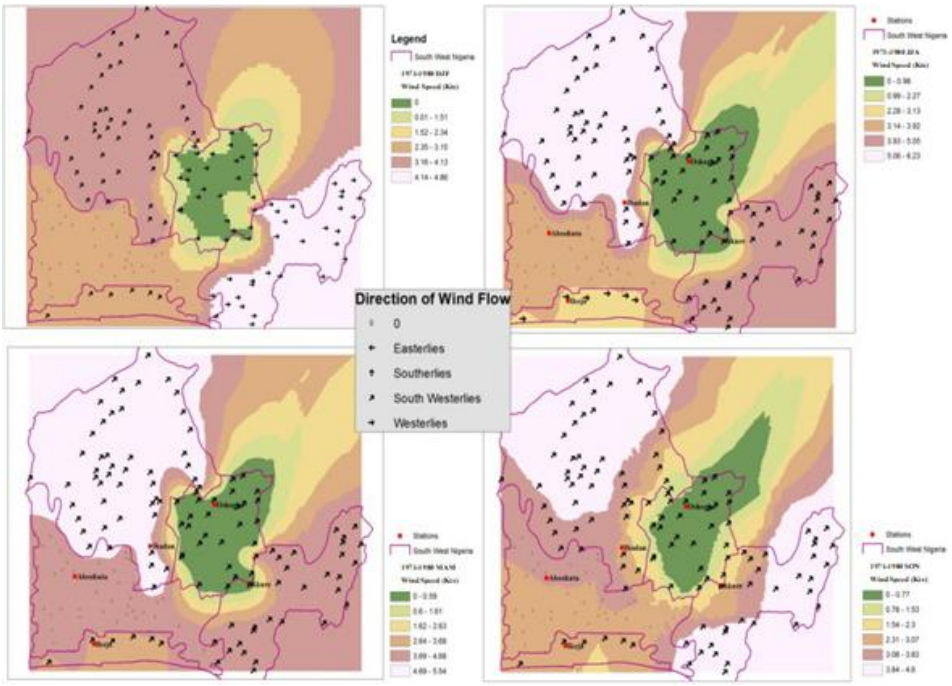

Fig. 3. Predominant Seasonal Wind flow (1971-1980).

Extensive strong southerly wind flows characterized the study area with a corresponding rainfall amount of 136 mm in Ikeja, 113 mm in Ibadan, 119 mm in Osogbo and 142 mm in Akure in the season of SON. This result shows that a westerly monsoon wind was the major wind direction that explained the rainfall system of southwestern Nigeria in the first decade (1971-1980) of study. However, these meteorological stations are found to be domiciled in major cities in Nigeria. Meanwhile, high amounts of rainfall recorded in these stations are expected, as supported by Odjugo (2010) in his observation that there have been statistically significant levels of precipitation and temperatures in vast major cities in Nigeria.

The strong westerly wind flow was effective in all the seasons in the second decade (1981-1990) as shown in Figure 4. This pattern of wind flow generally affected the rainfall system of the study area with Ikeja recording a 34 mm mean seasonal rainfall amount. About 13 mm was recorded in Ibadan, 10 mm in Osogbo and 25 mm in Akure respectively. The raining season JJA was largely influenced by strong southerly components pushing from coastal areas toward the continent. Such push with high speed of wind fluctuating between 5.22-6.33 m/s in Ikeja and Ibadan created good weather conditions and high tendency for the development of eddies. This type of weather contributed remarkably to a high mean seasonal rainfall amount of 135 mm and 174 recorded in Ibadan and Ikeja. However, there are many high scrapers that obstructed the inflow of moisture laden southerly streams at any particular location. At such locations, bulk of eddies were developed and lower atmosphere were fully saturated and resulted in corresponding amount of rainfall.

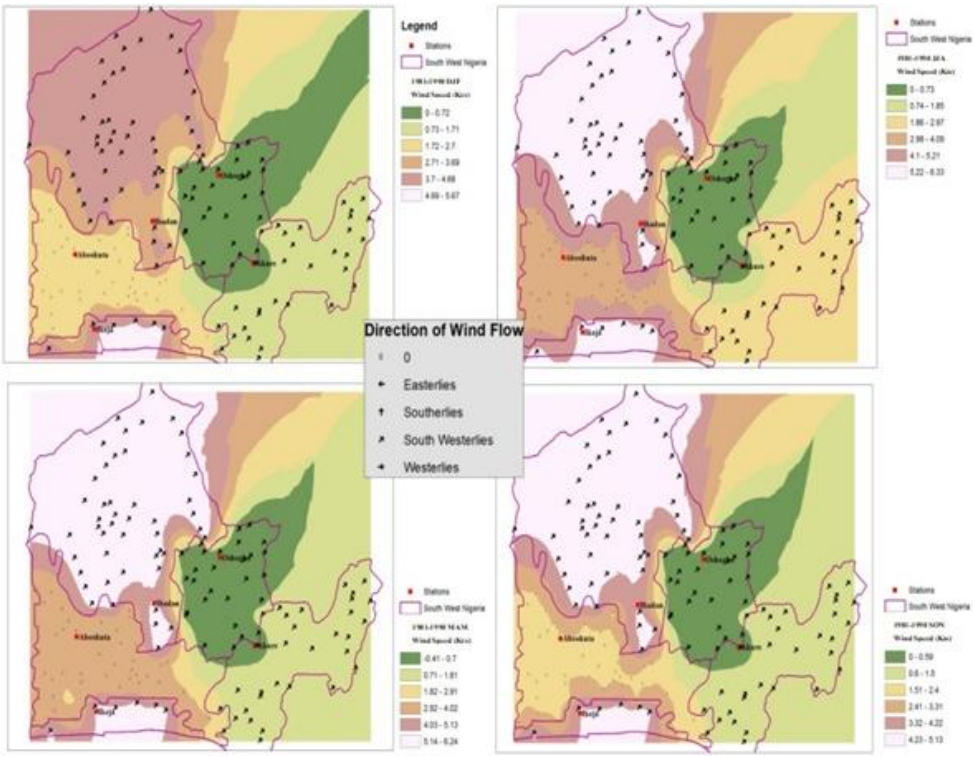

Fig. 4. Predominant Seasonal Wind flow (1981-1990).

In Osogbo, a relatively stable atmosphere of 0.1-0.73 m/s wind speed was noted. The humid nature of this environment accounted for the higher levels of rainfall, though the weather condition was fairly bad because

of the high pressure that characterized the area recorded with 138 mm amount of rainfall. Moreover, the convergence of direct southerly moisture flows over Akure with wind speed ranging between 0.74-1,85 m/s also affected the rainfall system of this area compared to other stations in the same season, JJA.

The season of MAM in the decade was also influenced by a tropical westerly wind with a mean seasonal rainfall amount of 133 mm recorded in Ikeja, 133 mm in Ibadan, 118 mm in Osogbo and 145 mm in Akure respectively. Akure recorded a high amount of rainfall, about 145 mm, due to the pronounced effect of the orographic nature of the area and the wind speed being relatively low (about 2.9 m/s). The SON season recorded low amounts of rainfall compared to SON of the previous decade. However, southerly wind dominated the season in all the stations with high wind speed fluctuating between 4.23-5.13 m/s in Ikeja and Ibadan. It was observed that high rates of wind speed in these stations resulted in low amount of rainfall in 100 mm in Ikeja and 93 mm in Ibadan compare to 113 mm in Osogbo and 124 mm recorded in Akure in the same SON season. The high amount of rainfall recorded during the seasons MAM and JJA, and relatively high rainfall in SON is as a result of the movement of ITD towards the northern part of the country during these seasons. Adejuwon et al. (1990) and Ayoade (1988) are in support of this, finding that ITD is the most popularly accepted medium that influences rainfall distribution in Nigeria. In other words, rain falls mostly when an area is overlain by the maritime air mass and ceases when the area is overlain by continental tropical air mass.

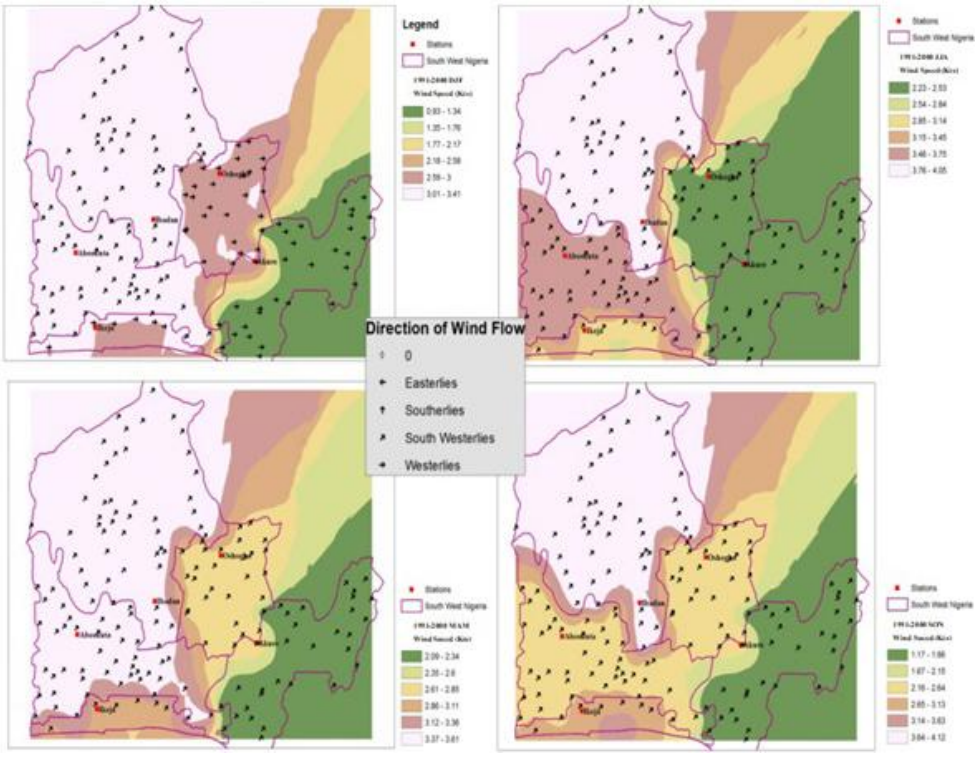

Fig. 5. Predominant Seasonal Wind flow (1991-2000).

In Figure 5, it was observed that both Westerlies and South-westerly wind streams were the major wind patterns that controlled the rainfall system of the study area in the decade (1991-2000). The summer period of DJF revealed that South-westerly winds over Ibadan and Abeokuta produced mean seasonal

rainfall amount of 12 mm and 16 mm. The westerly wind component over Osogbo, Akure and Ikeja recorded low amounts of mean seasonal rainfall of 13 mm, 20 mm and 17 mm respectively. The rate of wind speed in Akure was extremely low compared to other stations. This low wind speed however must have been the reason for the station recording increased amounts of rainfall. Ideally, low wind speed would always promote air convergence in the lower atmosphere.

In the season of JJA, a South-westerly air stream was very pronounced and acted to induce convective precipitation as high mean seasonal rainfall amount of 199 mm in Ikeja, 183 mm in Ibadan, 151 mm in Abeokuta, 158 mm in Osogbo and 198 mm in Akure were recorded respectively. Wind speed contributed to the development of various weather systems in this season because the low effect of the southerly moist air from the Atlantic Ocean influenced the weather pattern in Ikeja, thereby increased the rainfall amount compared to other stations that were far apart from the effect. The MAM and SON were predominantly influenced by the South-westerly monsoon wind that repeated itself from season to season. The season being the period for rainfall onset, received a corresponding rainfall amount of 121 mm in Ikeja, 109 mm in Ibadan, 116 mm in Abeokuta, 119 mm in Osogbo and 162 mm in Akure. A kind of low pressure was created in SON toward the Atlantic Ocean, with wind speed ranging between 3.63-4.12 m/s in Ibadan and 3.14-3.63 m/s in Akure. This showed that weather condition was fairly good, and that the atmosphere was relatively stable in the season. This is the reason for the season recording a corresponding rainfall amount of 101 mm in Ikeja, 107 mm in Ibadan, 77 mm in Abeokuta, 112 mm in Osogbo and 109 mm in Akure. Wind speed was generally low in the decade compared to the last decade. However, the ITD has been shifted towards the southern part of the country whereby dry wind with easterly effect has greater influence on the rainfall system at this season. Both the temperature and wind speed are on the increase during the season of DJF because of the state of ITD. Adejuwon (1990) supported this finding with his assertion that rainfall characteristics in terms of distribution, retreat and periodicities cannot be compared with the relatively stable nature of the temperature.

This study revealed that, in Figure 6, southerly wind stream, westerly wind and South-westerly wind flows were the principal wind patterns that controlled the rainfall system of the study area in the 2001-2010 decade. Southerly wind was prevalent in Ibadan and Abeokuta in the season of DJF, MAM, JJA and SON while southerly wind over Ikeja in the season of MAM and SON produced the mean seasonal rainfall of 137 mm and 130 mm. Similarly, strong consistent westerly winds with continental air mass over Osogbo and Akure in DJF accounted for low mean seasonal rainfall amount of 13 mm and 15 mm respectively. Osogbo recorded 118 mm high amount of rainfall in SON season because of strong westerly push. Meanwhile, South-westerly wind influenced the rainfall system in JJA and MAM in all the stations with the exception of Ikeja with corresponding mean seasonal rainfall amount ranging between 100-230 mm with maximum wind speed fluctuating between 5.19-5.98 m/s in the season of peak amount of rainfall (JJA). However, the low wind speed of 0.71-1.27 m/s was recorded in SON season. In DJF, atmospheric volume was reduced and allowed the free flow of air stream especially in Ikeja, Osogbo and Abeokuta fluctuating between 4.0-4.6 m/s, 3.4-3.9 m/s and 2.79-3.39 m/s respectively.

The season of JJA revealed that extensive westerly stream had its way over the entire study area. Akure recorded substantial mean seasonal rainfall of about 146 mm because the speed of wind was very low thereby allowing the formation of rain-forming cloud. Ikeja received about 137 mm of rainfall because of the effect of local wind, e.g. the prevailing sea breeze. The low effect of the sea breeze was also noted in Abeokuta just as continental effects like relief, topography and vegetation typically influenced the rainfall system of Akure. This result is supported by Barbro and Deliang (2003): that precipitation distribution in Sweden is largely influenced by wind speed and topography.

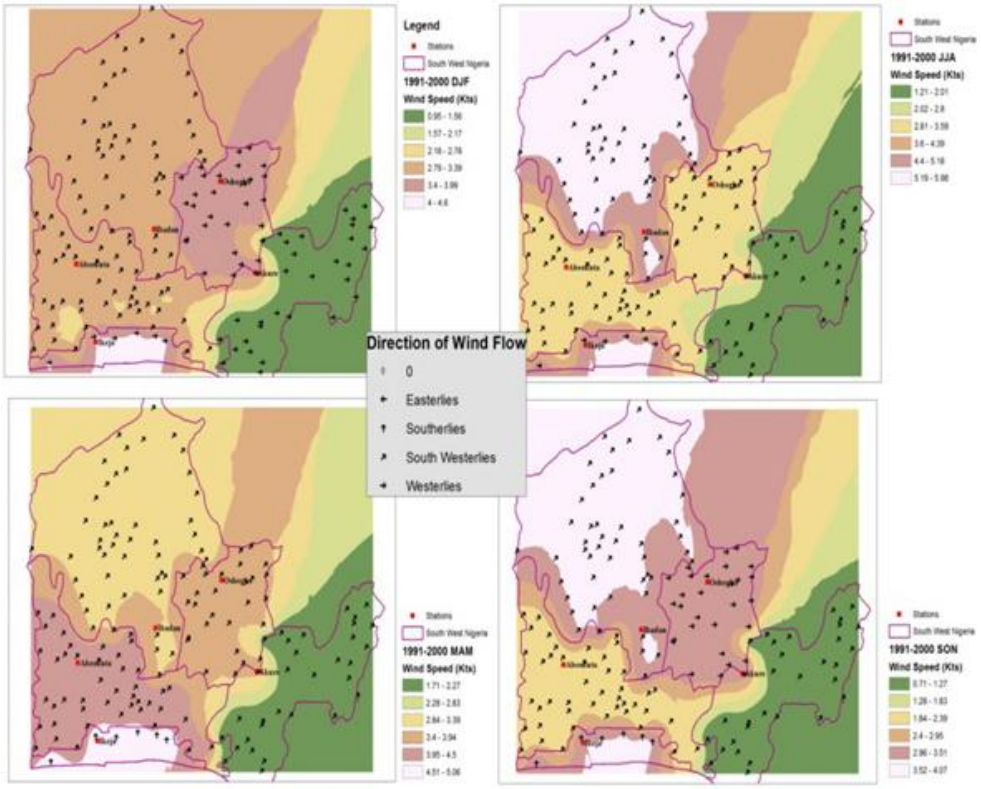

Fig. 6. Predominant seasonal wind flow (2001-2010).

Figure 7 showed the predominant direction of wind flows between 2001-2010 in the study area. The DJF season recorded that South-westerly wind streams were very prominent in Ikeja, Ibadan, Abeokuta and Osogbo with corresponding mean seasonal rainfall amount 28 mm, 18 mm, 11 mm and 15 mm respectively, and direct westerlies over Akure accounting for 20 mm mean seasonal rainfall. The season of JJA was the peak of maximum mean seasonal rainfall in the decade. The season was majorly controlled by South-westerly monsoon winds with a remarkable corresponding rainfall amount of 214 mm in Ikeja, 178 mm in Ibadan, 168 mm in Abeokuta, 166 mm in Osogbo and 240 mm in Akure compared to the SON season which was controlled by the South-westerly wind. It could be pointed out that the season of SON had little effect on easterly flows from the Sahara area. This easterly flow contributed to little decline in rainfall amount to 130 mm, 106 mm, 86 mm, 118 mm and 131 mm recorded in Ikeja, Ibadan, Abeokuta, Osogbo and Akure respectively compared with the JJA season in the decade.

Interestingly, the MAM season recorded average mean seasonal rainfall amount due to the interception of easterly winds over this period. The decade was marked with high wind speeds in Ikeja, ranging between 5.38-6.18 m/s in DJF, 5.22-5.63 m/s in JJA, 5.62-6.24 m/s in MAM and 4.66-5.29 m/s in SON respectively. Similarly, Osogbo recorded an increasing wind speed, fluctuating between 4.57-5.37 m/s in DJF, 4.79-5.21 m/s in JJA, 4.99-5.61 m/s in MAM and 4.03-4.65 m/s in SON respectively. It thus implied that strong southerly winds exerted a great control on the rainfall system in the decade as measured with a reasonable mean seasonal rainfall amount. The decade must have recorded bountiful economic yields especially in the area of agriculture in the study area. Hsu and Guo's (2005) report is consonant with this finding that rainfall loss rate increases when wind speed increases and rainfall intensity decreases. In other words, rainfall amount is largely affected by predominant wind speed and wind direction.

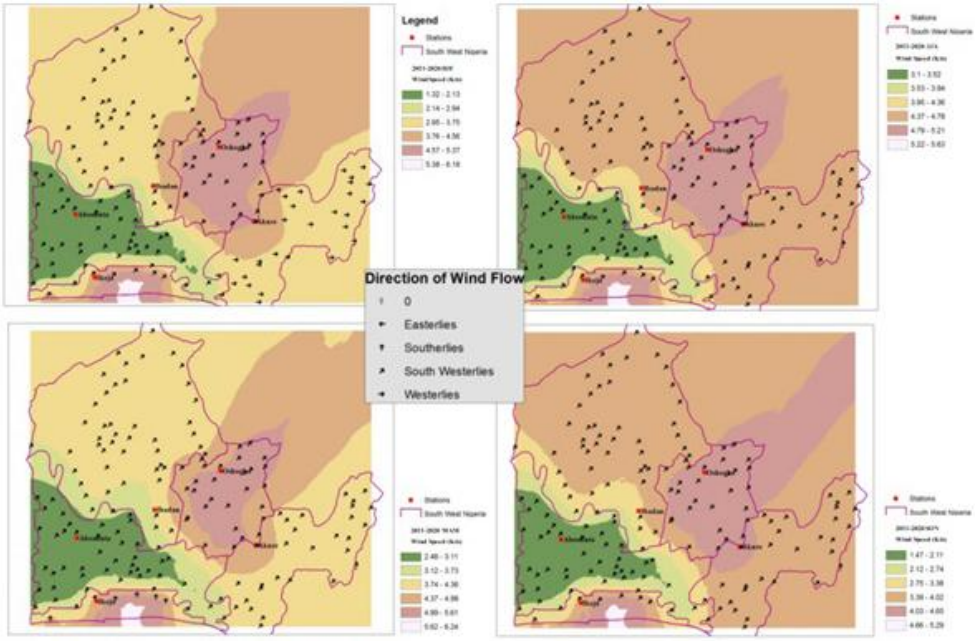

Fig. 7. Predominant Seasonal Wind flow (2011-2020).

4. Conclusion

The study has examined rainfall and wind flow patterns of southwestern Nigeria from 1971 to 2020 and observed a deviation from the annual mean. Ikeja was perceived as the wettest location in the rainy season of the June, July and August (JJA) months because of the strong southerly wind and local sea breeze that generated a remarkable amount of rainfall in the season. The recorded mean seasonal rainfall amounts of 303 mm in Ikeja, followed by Akure (229 mm), Osogbo (178 mm), and Ibadan (169 mm) were indications of local weather patterns, like sea breeze influence, that usually results in rainfall variability. The South-westerly monsoon is moisture laden and, hence, a rain bearing wind, which blows inland from the Atlantic Ocean. The study also observed the weakness of the wind during the December, January and February (DJF) months due to the local influence of the dry harmattan wind that blows northerly from the opposite direction. This period of dryness has been accounted for low rainfall amount recorded in most stations. especially in Ibadan at this time.

References

Adejuwon J.O., 2012, Rainfall seasonality in the Niger Delta Belt, Nigeria, Journal of Geography and Regional Planning, 5 (2), 51-60, DOI: 10.5897/JGRP11.096.

Adejuwon J.O., Balogun E.E., Adejuwon S.S., 1990, On the annual and seasonal patterns of rainfall fluctuations in sub-saharan West Africa, International Journal of Climatology, 10 (8), 839-848, DOI: 10.1002/joc.3370100806.

Ayansina A., Ogunbo S., 2009, GIS approach in assessing seasonal rainfall variability in Guinea savanna part of Nigeria, 7th FIG Regional Conference, Vietnam, 19-22 October 2009.

Ayoade J.O., 1988, Introduction to Climatology for the Tropics, Spectrum Books Ltd., Ibadan.

Ayoade J.O., 2004, Climate Change: A Synopsis of Its Nature, Causes, Effects and Management, Vantage Publishers Ltd., Ibadan.

Babatolu S.J., 2002, Climate Change and its Implications for Water Supply in the Niger Basin Development Authority Area of Nigeria, Ph.D. Thesis, University of Ilorin, Ilorin, Nigeria.

Barbro J., Deliang C., 2003, The influence of wind and topography on precipitation distribution in Sweden: Statistical analysis and modelling, International Journal of Climatology, 23 (12), 1523-1535, DOI: 10.1002/joc.951.

Bravar L., Kavvas M.L., 1991, On the physics of drought: I. A conceptual framework, Journal of Hydrology, 129 (1-4), 281-297, DOI: 10.1016/0022-1694(91)90055-M.

Christopherson R.W., 2012, Geosystems: An Introduction to Physical Geography, 8th ed., Pearson Education, Inc., Upper Saddle River, USA.

Christopherson R.W., Birkeland G.H., 2017, Geosystems: An Introduction to Physical Geography, 10th ed., Pearson Education, Inc., Upper Saddle River, USA.

Davy R., Gnatiuk N., Pettersson L., Bobylev L., 2018, Climate change impacts on wind energy potential in the European domain with a focus on the Black Sea, Renewable and Sustainable Energy Reviews, 81, 1652-1659, DOI: 10.1016/j.rser.2017.05.253.

Eludoyin O., 2009, Monthly variation in the 1985-1994 and 1995-2004 rainfall distribution over five selected synoptic stations in western Nigeria, Journal of Meteorology and Climate Science, 7, 11-22.

Hsu S.-H., Guo Y.-L., 2005, Effect of wind speed on the measurement of rainfall, Crop, Environment and Bioinformatics, 2 (1), 81-86.

Ifabiyi I.P., Omoyosoye O., 2011, Rainfall characteristics and Maize Yield in Kwara State, Nigeria, Journal of Applied Sciences, 1 (3), 60-65.

Igwenagu C.M., 2015, Trend analysis of rainfall pattern in Enugu State, Nigeria, European Journal of Statistics and Probability, 3 (3), 12-18.

Ikhile C.I., Aifesehi P.E.E., 2011, Geographical Distribution of average monthly rainfall in the western section of Benin-Owena River Basin, Nigeria, African Reseach Review, 5 (4), 493-500.

Iloeje N.P., 1981, A New Geography of Nigeria, New Revised Edition, Longman Publishers, London.

Odjugo P.A.O., 2010, General overview of climate change impacts in Nigeria, Journal of Human Ecology, 29 (1), 47-55, DOI: 10.31901/24566608.2010/29.01.05.

Oguntunde P.G., Abiodun B.J., Gunnar L., 2012, Spatial and temporal temperature trends in Nigeria, 1901-2000, Meteorology and Atmospheric Physics, 118, 95-105, DOI: 10.1007/s00703-012-0199-3.

Ojo O., 1977, Climates of West Africa, Heineman Publishers, Ibadan.

Olaniran O.J., 2002, Rainfall Anomalies: The Contemporary Understanding, 55th Inaugural Lecture Series, University of Ilorin, Ilorin, Nigeria.

Omogbai B.E., 2010, Rain days and their predictability in South Western region of Nigeria, Journal of Human Ecology, 31, 185-195, DOI: 10.1080/09709274.2010.11906314.

Oyewo O.P., 2005, Trend in Rainfall in Northern Nigeria, Unpublished B.Sc, Project, Department of Geography, University of Ilorin, Ilorin, Nigeria.

Analysis of heatwaves in Uzbekistan: characteristics, implications, and future climate projections

Bobur Yakhshiboev, Zhaozhong Feng

Nanjing University of Information Science and Technology, China

Abstract

Heatwaves (HWs) have emerged as some of the most serious climate-induced hazards worldwide. This research analyzes the occurrence, characteristics, and consequences of HWs across Uzbekistan between 1980 and 2020. The study primarily aims to identify heatwave thresholds, examine related meteorological patterns, and evaluate their influence on human health and agricultural systems. Using reanalysis data from the National Center for Environmental Prediction and the National Center for Atmospheric Research (NCEP/NCAR), heatwave thresholds were established based on temperature anomalies exceeding 5°C above the long-term July mean. Summer heat in Uzbekistan peaks in July; Bukhara and Khorezm are identified as the regions most affected by extreme temperatures. During the 40-year period, five HWs were documented in Bukhara and seven in Khorezm. Synoptic analysis revealed that persistent cyclonic activity dominated during these episodes, leading to stagnant and exceptionally warm atmospheric conditions. Mortality statistics from the United Nations indicate that although the overall death rate has declined since the late 1970s, the health risks associated with prolonged heat events remain substantial. Agricultural sensitivity was also evident, with increasing heat contributing to reduced crop yields and water stress, thus threatening food security. Furthermore, Coupled Model Intercomparison Project Phase 6 (CMIP6) model simulations under SSP1–2.6, SSP2–4.5, and SSP5–8.5 scenarios suggest that continued warming will likely heighten both the frequency and duration of HWs, posing greater risks to human well-being and agricultural resilience. These results underscore the need for enhanced early warning systems, improved weather forecasting, and climate-resilient policies in Uzbekistan. Strengthening community awareness and integrating scientific insights into policy frameworks are vital for minimizing the escalating impacts of HWs in a warming environment.

Keywords

Heatwaves, Uzbekistan, human health, agriculture, climate change.

Submitted 8 September 2025, revised 30 October 2025, accepted 7 November 2025

DOI: 10.26491/mhwm/214066

1. Introduction

Heatwaves (HWs) are widely recognized as one of the most hazardous extreme climate phenomena globally. The World Meteorological Organization (WMO 2016) defines a HW as a period of abnormally high temperatures persisting for at least two or more consecutive days (Chambers 2020). Additional researchers have broadened this criterion to encompass three or more consecutive days of anomalously elevated temperatures, frequently linked to significant social, environmental, and economic repercussions (Perkins-Kirkpatrick, Lewis 2020; Raei et al. 2018). Heatwaves generally arise when daily maximum temperatures exceed the long-term average by 5-10°C, occasionally accompanied by elevated humidity, and are strongly associated with negative health effects, agricultural losses, infrastructure impairment, and wildfires (Russo et al. 2017; Chen et al. 2019).

Worldwide, HWs have already inflicted catastrophic consequences. The HWs in Chicago during 1980 and 1995 were among the most lethal natural catastrophes in the United States in recent decades, resulting in

hundreds of deaths, especially among the elderly (Carlson 2008). The 2003 European heatwave resulted in more than 70,000 fatalities, predominantly among individuals over 75 years of age in France (Carlson 2008). These instances illustrate that HWs disproportionately affect vulnerable populations while also producing enduring consequences for agriculture and food security.

In Central Asia, especially Uzbekistan, HWs have increased in frequency and intensity over recent decades (USAID 2018b; World Bank 2021). The nation's arid and semi-arid continental climate, coupled with delicate ecosystems and limited water resources, heightens its susceptibility to excessive heat. Bukhara, Khorezm, and the Aral Sea basin are recognized as some of the most heat-affected areas, where HWs pose risks to public health, diminish agricultural productivity, and jeopardize sustainable development (UNFCCC 2016; World Bank 2020). Forecasts suggest that HWs in Uzbekistan might extend by 3-9 days and potentially by as much as 43 days by 2085 under high-emission scenarios (USAID 2018b). Such alarming projections highlight the urgent need for comprehensive scientific assessment and adaptation planning. This research examines the period from 1980 to 2020 and seeks to deliver a thorough evaluation of HWs in Uzbekistan. The primary objectives are (1) to ascertain heatwave thresholds and corresponding meteorological conditions; (2) to assess their effects on human health, agricultural output, and food security; (3) to investigate the correlation between HWs and climate change, including prospective scenarios based on CMIP6 projections; and (4) to delineate potential strategies and policies for mitigation and adaptation. A long-term view is crucial for identifying patterns and trends, as well as enhancing decision-making through superior forecasting and readiness.

This work addresses the information gap about HWs in Uzbekistan by merging observational datasets, reanalysis outputs, and climate model simulations. The findings are anticipated to offer significant insights for policymakers, health officials, and agricultural strategists in mitigating risks and bolstering resilience to excessive heat under a changing climate.

2. Data and methodology

2.1. Study area

Uzbekistan is a landlocked country in Central Asia, located between latitudes 37°N and 46°N and longitudes 56°E and 73°E. The area is approximately 447,000 km², bordered by Kazakhstan to the north, Kyrgyzstan and Tajikistan to the east, Afghanistan to the south, and Turkmenistan to the southwest. The country's geography is varied, comprising vast deserts (particularly the Kyzylkum Desert), rich river basins, and mountainous areas in the east. The climate is primarily arid to semi-arid continental, marked by cold winters and extensive, hot, dry summers (USAID 2018b; World Bank 2021). Average summer temperatures in Uzbekistan frequently surpass 30°C, with daily maxima attaining 45-49°C in arid areas (World Bank 2021). July is the warmest month, characterized by a heightened likelihood of HWs. The regions of Bukhara, Khorezm, and the vicinity of the Aral Sea are especially susceptible to high heat owing to their geographical positioning and dominant meteorological conditions. These regions also host

significant agricultural activities, including cotton and wheat cultivation, which are particularly vulnerable to extended periods of elevated temperatures and water shortages.

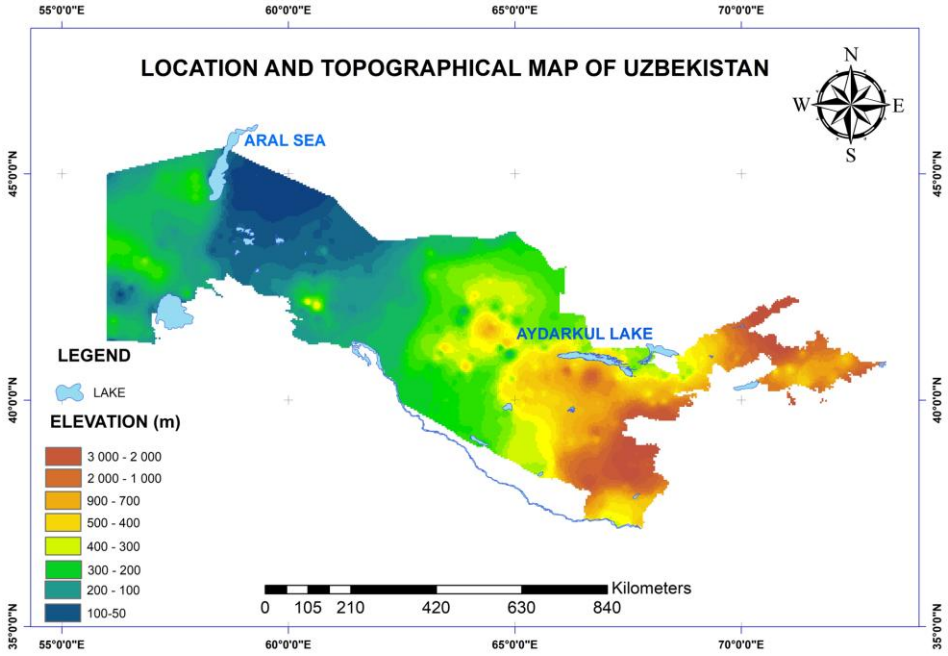

Fig. 1. Location and topographical map of Uzbekistan.

Uzbekistan's population is approximately 35 million (UZSTAT 2023), with prominent metropolitan centers including Tashkent, Samarkand, Bukhara, and Khorezm. Accelerated urbanization and inadequate adaptive infrastructure heighten the population's susceptibility to extreme heat. Furthermore, the ecological catastrophe in the Aral Sea region has intensified local climate extremes, making the northwest of the country a focal point for environmental stressors, including frequent HWs. Because of its geographic and meteorological attributes, Uzbekistan is a vital region for examining historical trends and future forecasts of HWs, along with their effects on human health, agricultural output, and food security (UNDP 2007; UNFCCC 2016). Uzbekistan's geographic position and the primary heat-prone areas are depicted in Figure 1.

2.2. Data

2.2.1. Reanalysis data

Two global reanalysis products were used to examine historical temperature variability and to identify HW occurrences across Uzbekistan. The ERA5 dataset from the European Centre for Medium-Range Weather Forecasts (ECMWF) provides high-resolution climate fields (0.25° × 0.25°) for the period 1980-2020, which were applied to analyze both spatial and temporal patterns of surface temperature and to create synoptic-scale sea-level pressure maps. The NCEP/NCAR Reanalysis produced by NOAA, with a coarser spatial resolution of 2.5° × 2.5° (Muñoz-Sabater et al. 2021), was also used for 1980-2020 to estimate HW thresholds and perform model comparison and validation (Copernicus Data Store). Heatwaves were identified when daily mean temperature anomalies exceeded 5°C above the long-term July average,

following the criteria of Barbier et al. (2018). Given the limited and discontinuous nature of ground-based observations in Uzbekistan, these reanalysis datasets were preferred for their consistent spatial coverage and temporal continuity, making them suitable for long-term climate analysis.

2.2.2. Climate projection data

Projected changes in temperature were analyzed using data from the Coupled Model Intercomparison Project Phase 6 (CMIP6), retrieved from the Canadian Climate Data Portal (https://climate-scenarios.canada.ca). The simulations span 1961-2067 and were interpolated to a 1° × 1° grid for consistency. The data were divided into four climatic intervals to represent historical and future conditions:

1. 1961-1992 (Historical I).
2. 1993-2005 (Historical II).
3. 2006-2036 (Future I).
4. 2037-2067 (Future II).

Three Shared Socioeconomic Pathways (SSPs) – SSP1–2.6, SSP2–4.5, and SSP5–8.5 – were applied to project warming trends and spatial variability (Miao et al. 2014; Araya-Osses et al. 2020; Navarro-Racines et al. 2020). Special emphasis was placed on Bukhara and Khorezm, identified as the regions most vulnerable to extreme heat events.

2.2.3. Socioeconomic data

Global socioeconomic datasets were incorporated to assess the potential human and agricultural consequences of rising temperatures. The United Nations World Population Prospects (1976-2100) dataset was used to analyze mortality rates (per 1,000 population) for Uzbekistan, excluding deaths attributed to COVID-19. Additionally, the World Bank Agriculture, Forestry, and Fishing dataset (1987-2020) was employed to investigate agricultural output and the economy's dependence on climate-sensitive sectors such as farming and irrigation.

2.2.4. Model validation data

Model performance was assessed using NCEP/NCAR reanalysis data as the observational baseline (Willmott et al. 2012; Duveiller et al. 2016). Three statistical indicators were computed to quantify the agreement between observed and simulated temperature fields:

- Correlation coefficient (R): measures the strength of linear association.
- Root Mean Square Error ($RMSE$): evaluates the magnitude of prediction errors.
- Index of Agreement (d): expresses the overall model consistency with observations.

These statistical metrics (R, $RMSE$, and d) were applied to assess the performance of CMIP6 simulations over Bukhara and Khorezm (Akoglu 2018). The characteristics of all datasets used in this study are summarized in Table 1.

Table 1. Data sources used in the study.

Dataset	Source	Period	Resolution	Purpose
ERA5	ECMWF	1980-2020	0.25° × 0.25°	Historical temperature and synoptic analysis
NCEP/NCAR	NOAA/PSL	1980-2020	2.5° × 2.5°	Heatwave detection and model validation
CMIP6 (SSP1–2.6, SSP2–4.5, SSP5–8.5)	IPCC/CCCS	1961-2067	1° × 1°	Future temperature projections
UN Mortality (WPP)	United Nations	1976-2100	National	Mortality trend related to climatic stress
World Bank Agriculture	World Bank	1987-2020	National	Agricultural productivity and climate impact

The combined datasets form a comprehensive foundation for analyzing both historical (1980-2020) and projected (1961-2067) temperature variability, as well as evaluating the socioeconomic implications of future HWs across Uzbekistan.

2.3. Methodology

The methodology employed in this study integrates statistical, synoptic, and climate projection techniques to analyze both historical and projected temperature variations and heatwave characteristics across Uzbekistan, with a particular focus on the Bukhara and Khorezm regions.

2.3.1. Spatial and temporal long-term mean of temperature (1980-2020)

To establish the baseline climatology and assess spatial-temporal variability of surface air temperature, the ERA5 reanalysis dataset provided by the ECMWF was utilized for the period 1980-2020. The ERA5 dataset offers high spatial and temporal resolution and has been widely validated for climatological studies (Muñoz-Sabater et al. 2021). Daily mean temperature data were processed and aggregated into monthly and seasonal means using MATLAB and Climate Data Operator (CDO) tools.

The long-term mean temperature for each grid cell was computed using Eq. (1):

$$\overline{\mathrm{T}} = \frac{1}{N}\sum_{i=1}^{N} T_i \quad (1)$$

where (T_i) is the monthly mean temperature for month i, and N represents the total number of months (480 for the 1980-2020 period).

Seasonal averages were calculated for the JJAS (June–July–August–September) period, which corresponds to the hottest part of the year in Central Asia. Spatial interpolation was performed using the Inverse Distance Weighting (IDW) method to visualize regional temperature gradients across Uzbekistan.

This climatological analysis provided the foundation for identifying the heat-prone regions and the warmest months, which served as a basis for subsequent heatwave detection and classification.

2.3.2. Heatwave identification and classification

Heatwave (HW) events were identified following the threshold-based approach of Barbier et al. (2018), where a 5°C temperature anomaly above the long-term July mean indicated a heatwave event. Similar definitions have been applied in previous global studies (Russo et al. 2017; Perkins-Kirkpatrick, Lewis 2020). Daily temperature data from ERA5 and NCEP/NCAR reanalysis (Kalnay et al. 2018) were used to calculate anomalies and to detect both heatwave (HW) and severe heatwave (SHW) occurrences during 1980-2020.

Each HW event was classified by its intensity and duration, as follows:

- $5°C \leq$ anomaly $< 7°C$ = HW;
- anomaly $\geq 7°C$ = SHW.

Sea-level pressure (SLP) and temperature fields from ERA5 were further analyzed to identify dominant synoptic patterns during HW periods. The 14-16 July 1986 HW over Khorezm was selected as a representative event to demonstrate the link between atmospheric circulation and surface temperature extremes.

2.3.3. Climate projection and future warming analysis

Future climate projections were derived from the Coupled Model Intercomparison Project Phase 6 (CMIP6) under three Shared Socioeconomic Pathway (SSP) scenarios – SSP1–2.6, SSP2–4.5, and SSP5–8.5 – representing low, moderate, and high greenhouse gas emission trajectories, respectively (Eyring et al. 2016).

Temperature outputs were interpolated to a $1° \times 1°$ grid and divided into four climatic periods:

1. 1961-1992 (Historical I).
2. 1993-2005 (Historical II).
3. 2006-2036 (Future I).
4. 2037-2067 (Future II).

Temporal and spatial analyses were conducted to assess projected changes in heatwave frequency, intensity, and distribution across Uzbekistan.

To evaluate model performance, NCEP/NCAR reanalysis data were used as the observational benchmark (Kalnay et al. 2018), and three standard statistical indicators were computed:

- Correlation coefficient (R) – linear agreement between observed and modeled data.
- Root Mean Square Error ($RMSE$) – magnitude of average model error.
- Index of Agreement (d) – measure of overall model-observation consistency (Willmott, Matsuura 2005).

Three statistical indicators – correlation coefficient (R), root mean square error ($RMSE$), and index of agreement (d) – were computed using Eqs. (2) – (4):

$$R = \frac{\sum(x_i - \bar{x})(y_i - \bar{y})}{\sqrt{\sum(x_i - \bar{x})^2 \sum(y_i - \bar{y})^2}} \quad (2)$$

$$RMSE = \sqrt{\sum(x_i - y_i)^2} \quad (3)$$

$$d = 1 - \frac{\sum(x_i - y_i)^2}{\sum(|y_i - \bar{x}| + |x_i - \bar{x}|)^2} \quad (4)$$

where (x_i) and (y_i) are observed (NCEP/NCAR) and modeled (CMIP6) temperatures, respectively; ($\bar{x}$) and ($\bar{y}$) denote their means; and *n* is the number of samples. As shown in Eqs. (2) – (4), these indicators collectively evaluate the linear relationship, model error magnitude, and overall agreement between observed and simulated temperatures. Validation was performed for Bukhara and Khorezm, identified as the regions most prone to extreme heat events.

2.3.4. Socioeconomic and agricultural impact assessment

To investigate the potential societal impacts of projected warming, the study integrated human mortality and agricultural datasets. Mortality rates (1976-2100) were obtained from the United Nations World Population Prospects; agricultural productivity indicators (1987-2020) were taken from the World Bank.

These datasets have been widely used in regional climate impact assessments (USAID 2018a; Liu et al. 2020).

This methodological framework integrates reanalysis-based statistical detection of HWs with CMIP6-driven future projections, providing a comprehensive foundation for understanding both historical and future HW behavior in Uzbekistan.

3. Results

3.1. Spatial and temporal variability of temperature (1980-2020)

ERA5 reanalysis data (1980-2020) reveal clear spatial and temporal variations in Uzbekistan's temperature pattern. The annual cycle (Fig. 2) shows July as the hottest month, with mean temperatures above 30°C in Bukhara and Khorezm, and occasional peaks exceeding 40°C in some years.

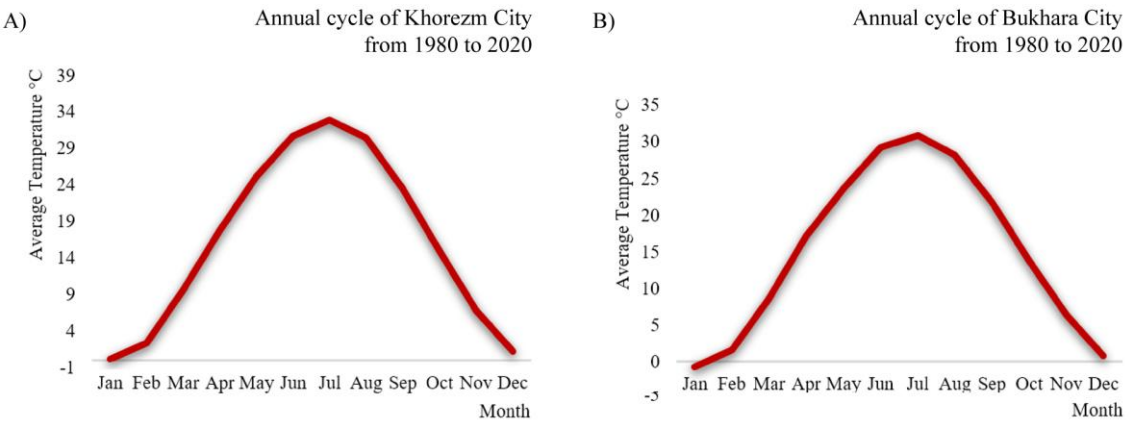

Fig. 2. Annual mean temperature (°C) for Uzbekistan's hottest cities: (a) Khorezm and (b) Bukhara (1980-2020).

Figure 3 illustrates the spatial distribution of temperature, where (a) shows the June–July–August–September (JJAS) seasonal mean and (b) represents the July long-term mean. The highest temperatures occur in the southwestern and central regions (Bukhara, Khorezm, Navoi), while the eastern highlands remain cooler. This baseline climatology supports the identification of heat-prone areas and defines the long-term July mean used for heatwave analysis.

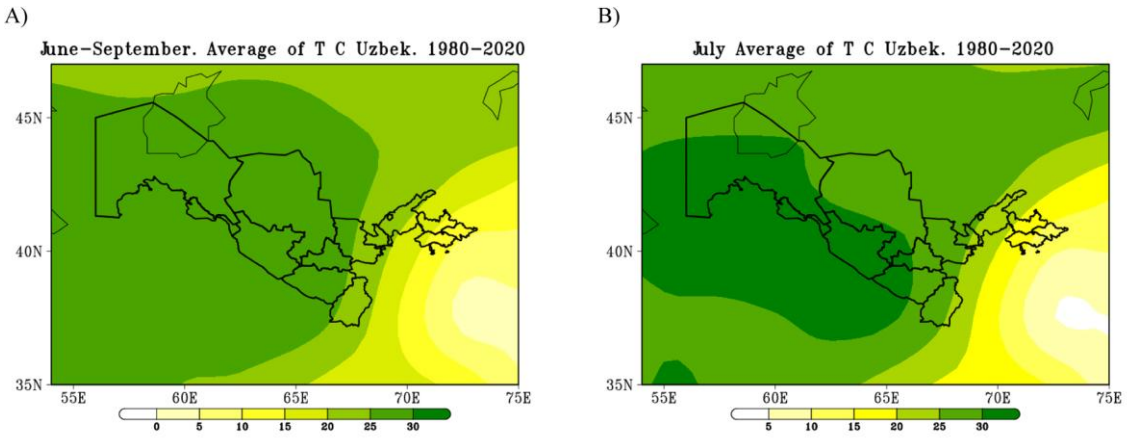

Fig. 3. Spatial distribution of average temperature (°C) over Uzbekistan (1980-2020): (a) JJAS seasonal mean and (b) July long-term mean.

3.2. Heatwave occurrence and classification (1980-2020)

These thresholds were taken as temperature anomalies from the July mean, as shown in Tables 1 and 2. The tables below present the detected HW and severe heatwave (SHW) events in Bukhara and Khorezm during 1980-2020. If the temperature anomaly equals +5°C, it is classified as a HW, whereas anomalies greater than +5°C indicate severe HWs. A total of five HWs were recorded in Bukhara and seven HWs in Khorezm (Tables 2-3). The most intense events reached anomalies of 8°C above the long-term mean.

Table 2. Heatwave statistics for Bukhara.

Bukhara city: Average temperature for July (1980-2020) is 30.84°C.			
Date	HW temp. °C	Anomaly	Intensity
29-31 July 1983	38.78	7.94	Severe
	39.00	8.16	
	36.08	5.24	
6-8 July 2005	36.53	5.69	Severe HW
	36.88	6.04	
	37.28	6.44	
15-17 July 2015	36.55	5.71	Severe HW
	37.37	6.5	
	36.25	5.4	
6-8 July 2017	35.75	5.0	HW
	35.97	5.0	
	35.85	5.0	

Table 3. Heatwave statistics for Khorezm.

Khorezm city: Average temperature for July (1980-2020) is 32.91°C			
Date	HW temp. °C	Anomaly	Intensity
23-25 July 1984	38.28	5.37	Severe HW
	40.21	7.30	
	39.15	6.24	
14-17 July 1986	38.28	5.37	Severe HW
	39.07	6.16	
	40.34	7.43	
	41.66	8.75	
14-17 July 1995	39.60	6.69	Severe HW
	38.68	5.77	
	39.63	6.72	
	38.85	5.94	
15-18 July 2002	38.07	5.16	Severe HW
	39.90	6.99	
	39.25	6.34	
	40.07	7.16	
5-7 July 2005	38.63	5.72	Severe HW
	40.50	7.59	
	41.50	8.59	
13-16 July 2015	39.82	6.71	Sever HW
	39.97	7.065	
	39.52	6.61	
	40.27	7.36	
19-22 July 2018	38.22	5.30	Severe HW
	39.57	6.66	
	40.87	7.96	

Heatwave events were detected using the 5°C anomaly threshold above the July mean. In Bukhara, five events were identified when daily temperature exceeded the mean by at least 5°C (Fig. 4). In Khorezm, seven events occurred under the same criterion (Fig. 5). Severe anomalies reached up to 8°C above the mean.

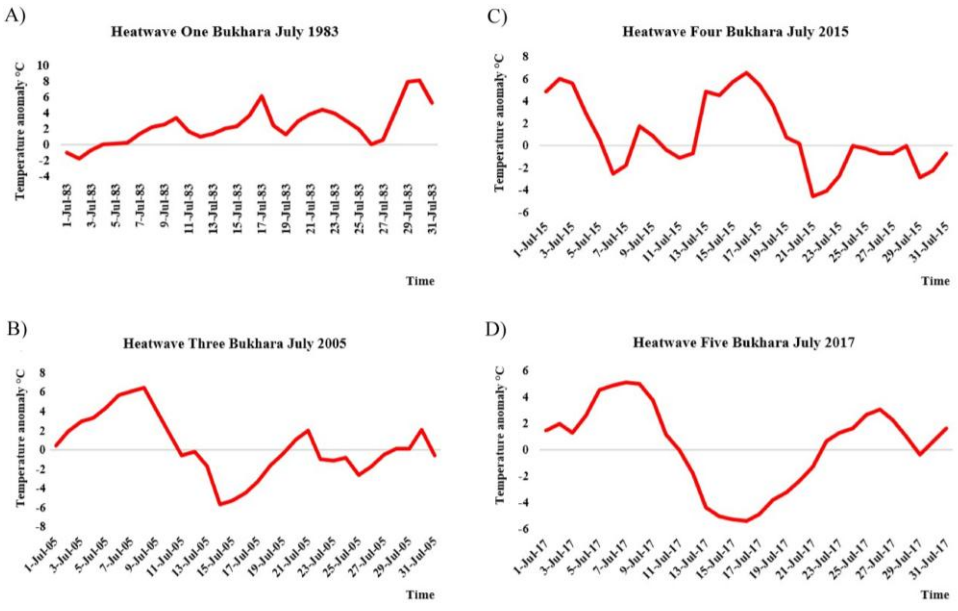

Fig. 4. Heatwave events over Bukhara when daily temperature exceeded the mean by ≥ 5°C.

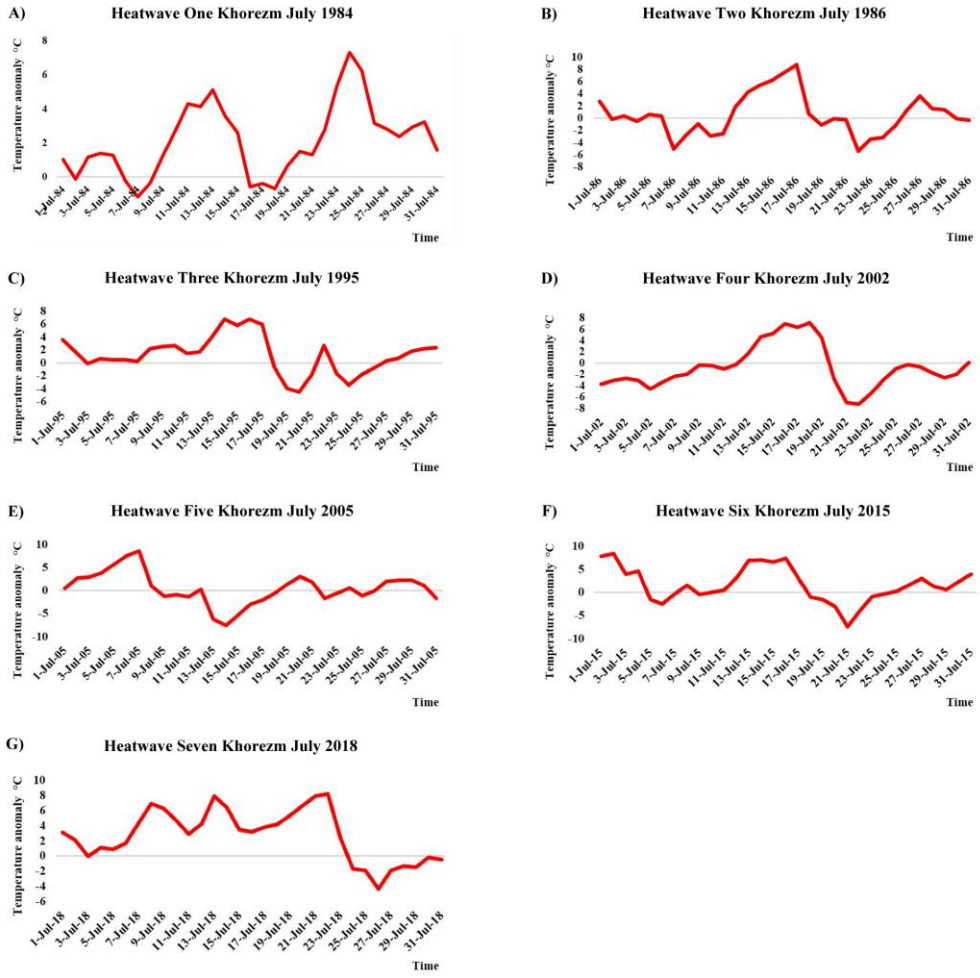

Fig. 5. Heatwave events over Khorezm when daily temperature exceeded the mean by ≥5°C.

3.3. Synoptic patterns and heatwave case study (July 1986)

The mean sea-level pressure and temperature distribution (Fig. 6) show that low-pressure systems dominate Uzbekistan during July, especially over Bukhara and Khorezm. These synoptic conditions are strongly associated with high surface temperatures and stagnant air masses, which favor HW development.

A representative severe heatwave event was observed from 14 to 16 July 1986 in Khorezm. During this period, mean daily temperature anomalies exceeded +5°C (Table 4), confirming a strong and persistent heatwave episode. The synoptic charts (Fig. 7) show a stationary low-pressure center and calm conditions, which reinforced surface heating across the region.

Table 4. Severe heatwave cases over Uzbekistan affected the city of Khorezm.

Date	Temperature °C	Temp. anomaly (July mean 32.91°C)	Intensity
14 July 1986	38.28	5.37	Severe HW
15 July 1986	39.07	6.16	Severe HW
16 July 1986	40.34	7.43	Severe HW

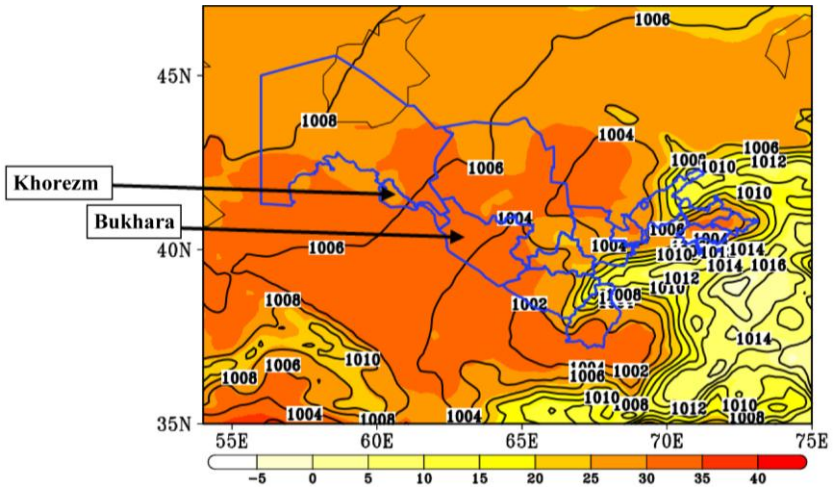

Fig. 6. July's long-term mean (1992-2020) shows sea-level pressure in hPa and temperature in degrees Celsius over Uzbekistan.

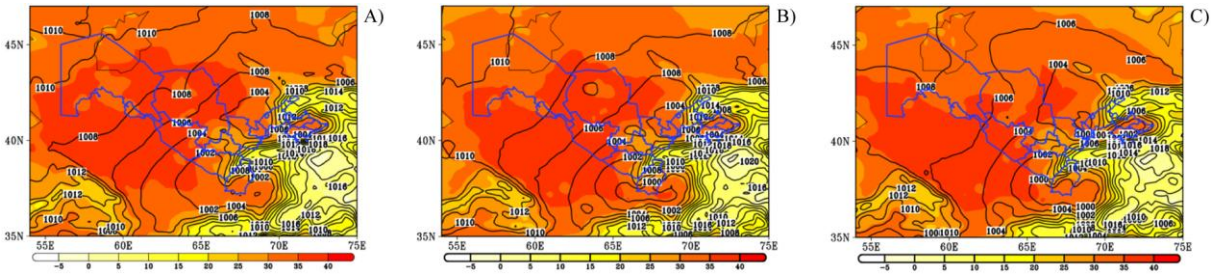

Fig. 7. Synoptic maps of the 14-16 July 1986 heatwave: (a) 14 July, (b) 15 July, (c) 16 July.

3.4. Model validation

Model performance was assessed using NCEP/NCAR reanalysis data as reference. Statistical indicators were used to evaluate CMIP6 temperature projections over Bukhara and Khorezm. Results indicate that the model performed better in Bukhara ($R = 0.28$, $RMSE = 0.76$, $d = 0.66$) than in Khorezm ($R = 0.04$, $RMSE = 0.97$, $d = 0.34$), showing moderate reliability, as shown in Table 5.

Table 5. Statistics used for model validation against NCEP/NCAR reanalysis dataset as observations.

	R	RMSE	Index of Agreement
Bukhara NCEP vs. Historical	0.28	0.759	0.655
Khoarizm NCEP vs. Historical	0.041	0.974	0.338

3.5. Future temperature projections (1961-2067)

The CMIP6 model outputs under three SSP scenarios (SSP1–2.6, SSP2–4.5, SSP5–8.5) indicate a clear warming trend throughout Uzbekistan. Four meteorological intervals were analysed using CMIP6 multi-model ensembles: 1961-1992, 1993-2005, 2006-2036, and 2037-2067. During the historical period from 1961 to 2005, July average temperatures rarely exceeded 30°C, except at Khorezm (Fig. 8a-b). In the SSP1–2.6 scenario (2036-2067), July averages in Bukhara and Khorezm are projected to increase by 2-3°C (Fig. 8c-d). Projections with SSP2–4.5 and SSP5–8.5 suggest considerable warming, with average July temperatures above 33°C across vast areas of Uzbekistan by 2067 (Fig. 9a-d).

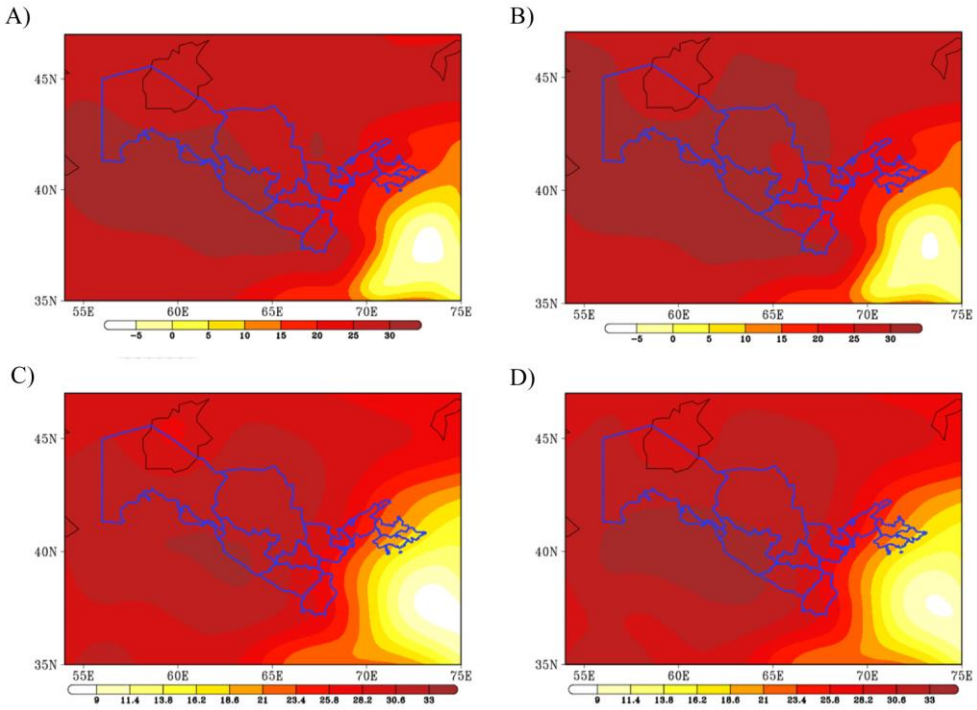

Fig. 8. Spatial distribution of mean air temperature (°C) during the historical periods, where (a) represents 1961-1992 and (b) represents 1993-2005. For the SSP2–4.5 scenario, (c) corresponds to 2006-2036, and (d) corresponds to 2037-2067.

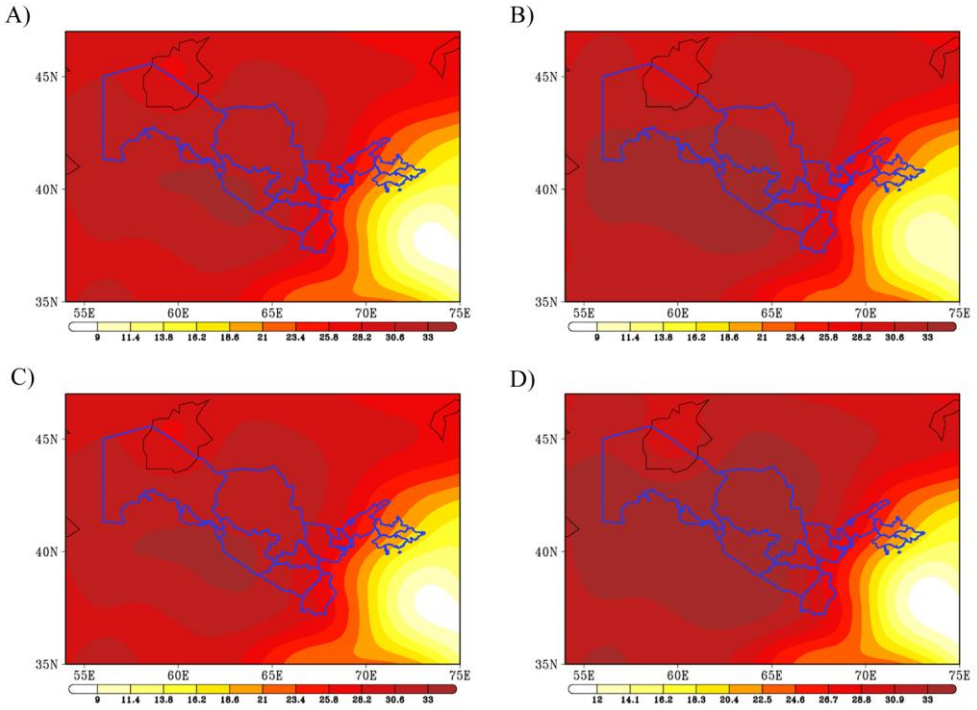

Fig. 9. Spatial distribution of projected mean air temperature (°C) under SSP2–4.5 and SSP5–8.5 scenarios. Panels (a) and (b) represent SSP2–4.5 for 2006-2036 and 2037-2067, respectively, while panels (c) and (d) represent SSP5–8.5 for the same periods.

Figures 10 and 11 present temperature projection time series for Bukhara and Khorezm, including the historical baseline (1976-2005) and future periods (2006-2067). City-level projections suggest that July temperatures in Khorezm may rise by more than 1.5°C (Fig. 12) and more than 3°C in Bukhara (Fig. 13).

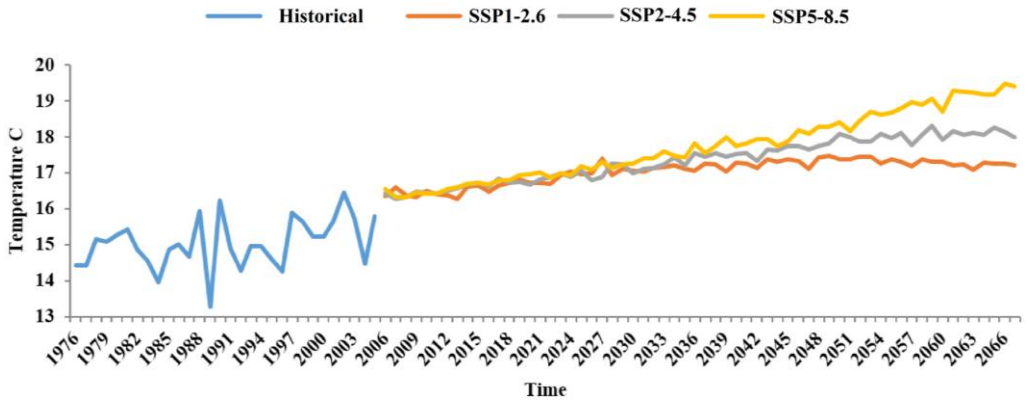

Fig. 10. Time series of projected temperature over Bukhara, covering the historical period (1976-2005) and future projections (2006-2067) under CMIP6 SSP scenarios.

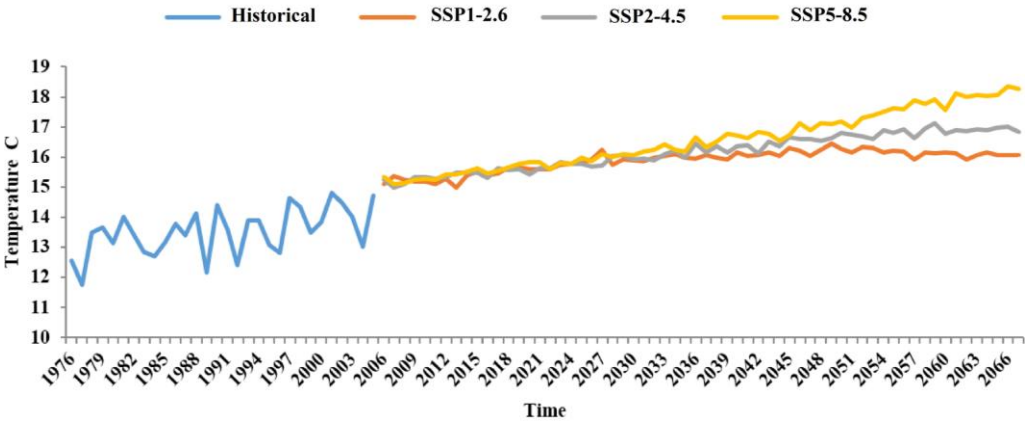

Fig. 11. Time series of projected temperature over Khorezm, showing the historical (1976-2005) and future (2006-2067) temperature projections under CMIP6 SSP scenarios.

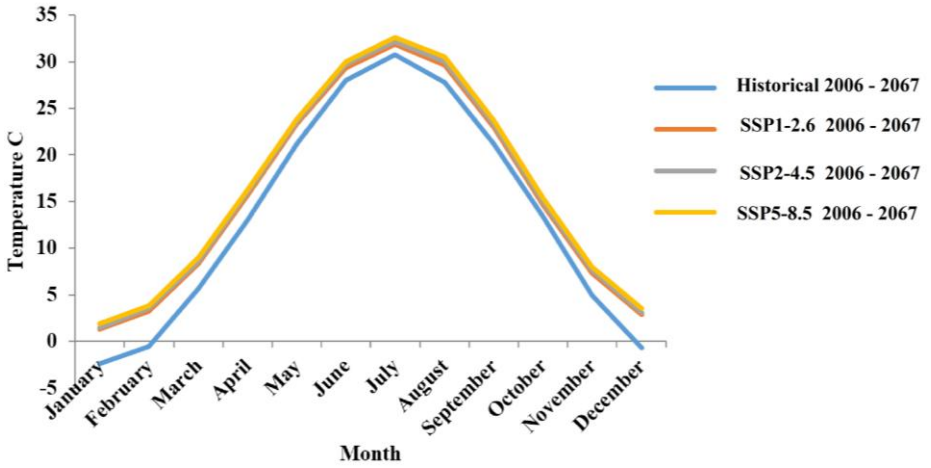

Fig. 12. Annual temperature cycle comparing historical, SSP1–2.6, SSP2–4.5, and SSP5–8.5 scenarios for Khorezm City.

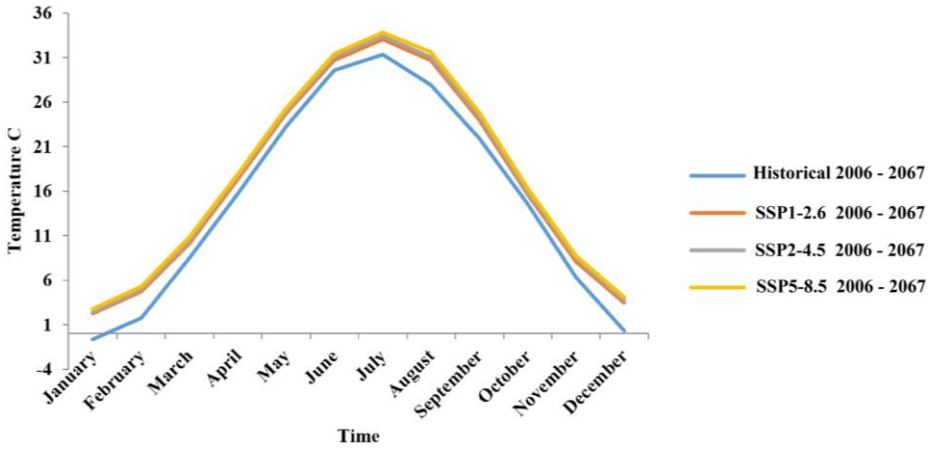

Fig. 13. Annual temperature cycle comparing historical, SSP1–2.6, SSP2–4.5, and SSP5–8.5 scenarios for Bukhara City.

3.6. Projected mortality and agricultural trends (1976-2100)

Projected mortality data from the United Nations World Population Prospects (UN WPP) show that mortality rates are expected to increase steadily until 2067, coinciding with the projected temperature rise (Fig. 15). The World Bank agricultural dataset (1987-2020) shows that years with higher temperatures are generally associated with reduced crop productivity and greater water stress, underlining the vulnerability of Uzbekistan's agricultural economy to climate extremes.

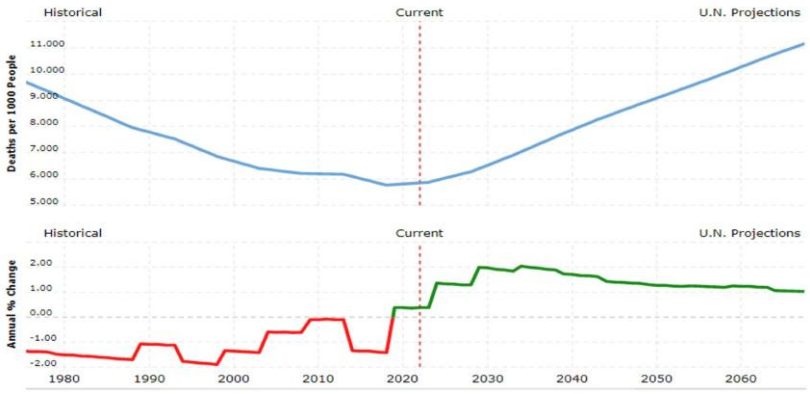

Fig. 14. Projected human mortality rate for Uzbekistan from 1976 to 2067.

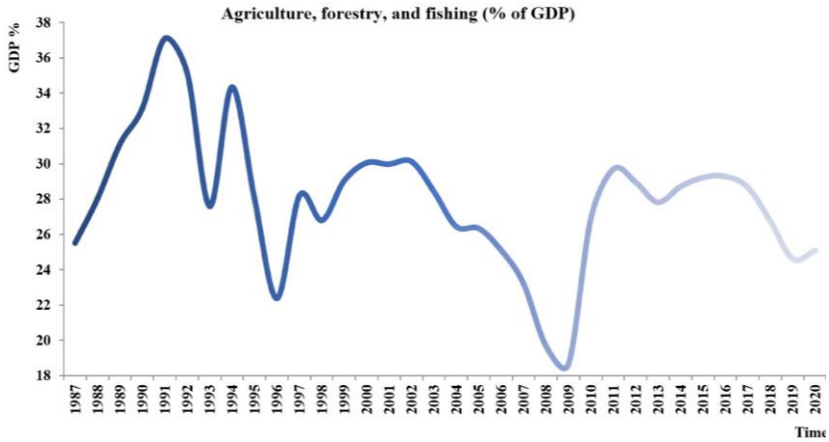

Fig. 15. Agricultural production, forestry, and fishing as a percentage of GDP for Uzbekistan from 1987 to 2020.

4. Discussion

The results indicate a clear warming pattern across Uzbekistan over the past four decades, consistent with regional trends in Central Asia (Liu et al. 2020). Similar findings have been reported in other regions of the world. For instance, Yaméogo (2024) found increasing extreme temperatures before, during, and after the rainy season in Burkina Faso, while Abatan et al. (2016) documented a rise in hot extremes and a decline in cold events across Nigeria. These African studies, like our results in Uzbekistan, confirm a persistent warming tendency in semi-arid and arid environments strongly influenced by large-scale atmospheric circulation.

Analysis of ERA5 data confirmed that July is the hottest month, with mean temperatures above 30°C in Bukhara and Khorezm, occasionally exceeding 40 °C. The June–September season is the main warm period, especially across the southwest and central plains, where low elevation and desert surfaces enhance heat accumulation. Comparable seasonal dynamics have also been reported in West Africa (Ankrah et al. 2023), where maximum and minimum temperatures have increased significantly under future climate scenarios, particularly during warm months.

Heatwave analysis (1980-2020) revealed five events in Bukhara and seven in Khorezm, mostly classified as severe (> +5°C anomaly). Though infrequent, HWs are intense due to stagnant atmospheric circulation and weak winds (Barbier et al. 2018; Chen et al. 2019). In the July 1986 case, a stationary cyclone caused calm winds and surface heat buildup, a pattern typical of Central Asian extremes (Kang et al. 2019). Similar patterns of prolonged summer heat and weak circulation were also observed in Serbia (Tošić et al. 2023), where warm days and tropical nights have increased notably during the past seven decades.

Model validation against NCEP/NCAR reanalysis showed moderate accuracy: good agreement for the index of agreement (d), but weak correlation (R). Despite local bias, CMIP6 models reliably captured the regional warming trend (Eyring et al. 2016; Chen et al. 2019). Future projections under SSP1–2.6, SSP2–4.5, SSP5–8.5 reveal a pronounced warming of 3.0 to 3.5°C by 2067 in Uzbekistan. The 30°C isotherm expands northward, indicating longer and stronger HWs (Kang et al. 2019). The eastern highlands remain cooler under persistent high-pressure influence. Projections of similar warming tendencies were also made for Europe; Tomczyk et al. (2022) reported continuous increases in maximum air temperature and the number of hot days across Poland throughout the twenty-first century.

Socioeconomic data highlight rising mortality and reduced agricultural productivity, consistent with higher temperatures and water scarcity (Sutton et al. 2013). Such impacts mirror regional trends of drought, evapotranspiration, and food insecurity (USAID 2018a; Liu et al. 2020).

Overall, Uzbekistan's climate is warming rapidly; HWs, though rare, are intensifying. Without adaptation, CMIP6 projections suggest increasing risks to human health, agriculture, and water resources. Integrated adaptation measures and regional cooperation are urgently needed to build long-term climate resilience.

5. Conclusion

The 40-year temperature analysis (1980-2020) confirmed that July is the hottest month in Uzbekistan, with Bukhara and Khorezm identified as the main regions prone to HWs. Using the NCEP/NCAR reanalysis dataset, a 5°C anomaly above the July mean was determined as the heatwave threshold. Based on this criterion, five events were detected in Bukhara and seven in Khorezm. Synoptic assessment revealed that stationary cyclonic systems dominated during extreme events, causing calm winds and intense surface heating, typical precursors of severe heat episodes in Central Asia.

Future climate projections from CMIP6 models (SSP1–2.6, SSP2–4.5, SSP5–8.5) indicate a persistent warming trend, with mean temperatures expected to rise by 3 to 3.5°C by 2067, especially in the southwestern lowlands. This warming will likely increase heatwave frequency and intensity, aggravate water scarcity, and reduce agricultural productivity.

Socioeconomic analyses show that mortality rates may rise because of intensified thermal stress, while agricultural yields decline in hotter years, highlighting the vulnerability of Uzbekistan's irrigation-dependent economy. Model validation demonstrated moderate but acceptable accuracy, particularly for Bukhara, supporting the use of CMIP6 outputs for regional assessments.

Overall, Uzbekistan's climate is warming rapidly, and severe but infrequent HWs represent growing threats to human health, agriculture, and water resources. To enhance resilience, it is essential to strengthen early-warning systems, promote climate-smart agricultural practices, and implement integrated national adaptation strategies across Uzbekistan and Central Asia.

References

Abatan A.A., Abiodun B.J., Lawal K.A., Gutowski Jr. W.J., 2016, Trends in extreme temperature over Nigeria from percentile-based threshold indices, International Journal of Climatology, 36 (6), 2527-2540., DOI: 10.1002/joc.4510.

Akoglu H., 2018, User's guide to correlation coefficients, Turkish Journal of Emergency Medicine, 18 (3), 91-93, DOI: 10.1016/j.tjem.2018.08.001.

Ankrah J., Monteiro A., Madureira H., 2023, Extreme temperature and rainfall events and future climate change projections in the coastal Savannah agroecological zone of Ghana, Atmosphere, 14 (2), DOI: 10.3390/atmos14020386.

Araya-Osses D., Casanueva A. Román-Figueroa C., Uribe J.M., Paneque M., 2020, Climate change projections of temperature and precipitation in Chile based on statistical downscaling, Climate Dynamics, 54 (9-10), 4309-4330, DOI: 10.1007/s00382-020-05231-4.

Barbier J., Guichard F., Bouniol D., Couvreux F., Roehrig R., 2018, Detection of intraseasonal large-scale heat waves: characteristics and historical trends during the Sahelian spring, Journal of Climate, 31 (1), 61-80, DOI: 10.1175/JCLI-D-17-0244.1.

Carlson A.E., 2008, Heat waves, global warming, and mitigation, UCLA Journal of Environmental Law and Policy, 26 (1), 169-215, DOI: 10.5070/L5261019556.

Chambers J., 2020, Global and cross-country analysis of exposure of vulnerable populations to heatwaves from 1980 to 2018, Climatic Change, 163 (1), 539-558, DOI: 10.1007/s10584-020-02884-2.

Chen X., Li N., Liu J., Zhang Z., Liu Y., 2019, Global heat wave hazard considering humidity effects during the 21st century, International Journal of Environmental Research and Public Health, 16 (9), DOI: 10.3390/ijerph16091513.

Duveiller G., Fasbender D., Meroni M., 2016, Revisiting the concept of a symmetric index of agreement for continuous datasets, Scientific Reports, 6 (1), DOI: 10.1038/srep19401.

Eyring V., Bony S., Meehl G.A., Senior C.A., Stevens B., Stouffer R.J., Taylor K.E., 2016, Overview of the Coupled Model Intercomparison Project Phase 6 (CMIP6) experimental design and organization, Geoscientific Model Development, 9 (5), 1937-1958, DOI: 10.5194/gmd-9-1937-2016.

Kalnay E., Kanamitsu M., Kistler R., Collins W., Deaven D., Gandin L., Iredell M., Saha S., White G., Woollen J., Zhu Y., Chelliah M., Ebisuzaki W., Higgins W., Janowiak J., Mo K.C., Ropelewski C., Wang J., Leetmaa A., Reynolds R., Jenne R., Joseph D., 2018, The NCEP/NCAR 40-Year Reanalysis Project, [in:] Renewable Energy, B. Sorensen (ed.), Routledge, 146-194, DOI: 10.4324/9781315793245-16

Kang H., Zhu B., Gao J., He Y., Wang H., Su J., Pan C., Zhu T., Yu B., 2019, Potential impacts of cold frontal passage on air quality over the Yangtze River Delta, China, Atmospheric Chemistry and Physics, 19 (6), 3673-3685, DOI: 10.5194/acp-19-3673-2019.

Liu Y., Geng X., Hao Z., Zheng J., 2020, Changes in climate extremes in Central Asia under 1.5 and 2°C global warming and their impacts on agricultural productions, Atmosphere, 11 (10), DOI: 10.3390/atmos11101076.

Miao C., Duan Q., Sun Q., Huang Y., Kong D., Yang T., Ye A., Di Z., Gong W., 2014, Assessment of CMIP5 climate models and projected temperature changes over Northern Eurasia, Environmental Research Letters, 9 (5), DOI: 10.1088/1748-9326/9/5/055007.

Muñoz-Sabater J., Dutra E., Agustí-Panareda A., Albergel C., Arduini G., Balsamo G., Boussetta S., Choulga M., Harrigan S., Hersbach H., Martens B., Miralles D.G., Piles M., Rodríguez-Fernández N.J., Zsoter E., Buontempo C., Thépaut J.-N., 2021, ERA5-Land: a state-of-the-art global reanalysis dataset for land applications, Earth System Science Data, 13 (9), 4349-4383, DOI: 10.5194/essd-13-4349-2021.

Navarro-Racines C., Tarapues J., Thornton P., Jarvis A., Ramirez-Villegas J., 2020, High-resolution and bias-corrected CMIP5 projections for climate change impact assessments, Scientific Data, 7 (1), DO: 10.1038/s41597-019-0343-8.

Perkins-Kirkpatrick S.E., Lewis S.C., 2020, Increasing trends in regional heatwaves, Nature Communications, 11 (1), DOI: 10.1038/s41467-020-16970-7.

Raei E., Nikoo M.R., AghaKouchak A., Mazdiyasni O., Sadegh M., 2018, GHWR, a multi-method global heatwave and warm-spell record and toolbox, Scientific Data, 5 (1), DOI: 10.1038/sdata.2018.206.

Russo S., Sillmann J., Sterl A., 2017, Humid heat waves at different warming levels, Scientific Reports, 7 (1), DOI: 10.1038/s41598-017-07536-7.

Sutton W.R., Srivastava J.P., Neumann J.E., Droogers P., Boehlert B., 2013, Reducing the Vulnerability of Uzbekistan's Agricultural Systems to Climate Change, A World Bank Study, 123 pp.

Tomczyk A.M., Piniewski M., Eini M.R., Bednorz E., 2022, Projections of changes in maximum air temperature and hot days in Poland, International Journal of Climatology, 42 (10), 5242-5254, DOI: 10.1002/joc.7530.

Tošić I., Tošić M., Lazić I., Aleksandrov N., Putniković S., Djurdjević V., 2023, Spatio-temporal changes in the mean and extreme temperature indices for Serbia, International Journal of Climatology, 43 (5), 2391-2410, DOI: 10.1002/joc.7981.

UNDP, 2007, Uzbekistan: Climate Change and Sustainable Development, United Nations Development Programme.

UNFCCC, 2016, Third National Communication of the Republic of Uzbekistan under the UN Framework Convention on Climate Change, UNEP, UZHYMET, Tashkent, 221 pp.

USAID, 2018a, Climate risk in Mozambique: country risk profil, available online at https://reliefweb.int/report/mozambique/climate-risk-profile-mozambique-fact-sheet (data access 12.11.2025).

USAID, 2018b, Climate risk in Uzbekistan: country risk profil, available online at. https://www.preventionweb.net/publication/climate-risk-profile-uzbekistan (data access 12.11.2025).

UZSTAT, 2023, Demographic Situation in the Republic of Uzbekistan, Statistics Agency Under the President of the Republic of Uzbekistan.

Willmott C.J., Matsuura K., 2005, Advantages of the mean absolute error (MAE) over the root mean square error (RMSE) in assessing average model performance, Climate Research, 30, 79-82, DOI: 10.3354/cr030079.

Willmott C.J., Robeson S.M., Matsuura K., 2012, A refined index of model performance, International Journal of Climatology, 32 (13), 2088-2094, DOI: 10.1002/joc.2419.

WMO, 2016, WMO Statement on the Status of the Global Climate in 2015, WMO-No. 1167, available online at https://digitallibrary.un.org/record/3894644?v=pdf (data access 12.11.2025).

World Bank, 2020, Climate change in Uzbekistan: Illustrated summary, Zoï Environment Network, The Regional Environmental Centre for Central Asia, available online at https://www.preventionweb.net/publication/climate-change-uzbekistan-illustrated-summary (data access 12.11.2025).

World Bank, 2021, Climate Risk Country Profile: Uzbekistan, World Bank Group, Asian Development Bank, available online at https://www.adb.org/publications/climate-risk-country-profile-uzbekistan (data access 12.11.2025).

Yaméogo J., 2024, Changes in the seasonal cycles of extreme temperatures in the Sudano-Sahelian domain in West Africa: a case study from Burkina Faso, Meteorology Hydrology and Water Management, 12 (2), 33-57, DOI: 10.26491/mhwm/194451.

Assessment of bias correction techniques for historical precipitation simulations in Sudan

Khalid Hilal

The author conducted this research independently

Kamar Salieva

Kazhydromet, Kazakhstan

Abstract

This study evaluates the performance of several bias correction techniques applied to CMIP6 precipitation simulations over Sudan for the period 1991-2014, using the high-resolution CHIRPS observational dataset as a reference. Four widely used bias correction methods: Empirical Quantile Mapping (EQM), Gamma Quantile Mapping (Gamma-QM), Local Intensity Scaling (LOCI), and the Delta Method were applied to ten CMIP6 models to assess their ability to reduce systematic biases and improve consistency with observed climatology. The raw simulations reveal pronounced seasonal biases, characterized by overestimation during the pre-monsoon season (MAM) and underestimation during the monsoon season (JJAS), whereas annual biases are moderate but exhibit notable spatial heterogeneity. Among the tested techniques, EQM and Gamma-QM consistently yield the most effective corrections, achieving median bias reductions of 94-100% across both annual and seasonal timescales, and markedly enhancing Kling–Gupta Efficiency (*KGE*) values. Among the evaluated models, EC-Earth3, GFDL-ESM4, and INM-CM4-8 demonstrate the best performance annually and during June-September, whereas NESM3 performs better during March-May, highlighting model-specific strengths in simulating seasonal precipitation variability. Spatial analyses further confirm that bias corrections effectively align precipitation variability with observations, with statistically significant improvements across most regions of Sudan. These findings highlight the critical role of quantile-based correction methods in producing reliable CMIP6 precipitation outputs over Sudan and establish a robust framework for assessing both model skill and bias correction performance in regions characterized by complex, seasonally varying rainfall regimes.

Keywords

Climate modeling, downscaling, quantile mapping, seasonal rainfall, ensemble simulations.

Submitted 30 August 2025, revised 13 November 2025, accepted 18 November 2025

DOI: 10.26491/mhwm/214425

1. Background and motivation

Precipitation is a fundamental component of the hydrological cycle, supporting agricultural productivity, water resource management, and ecosystem sustainability. Sudan exhibits pronounced climatic variability, ranging from hyper-arid desert conditions in the north to semi-humid savannahs in the south. Understanding precipitation patterns and variability is therefore essential for mitigating drought impacts, ensuring food security, and developing effective climate adaptation strategies in this highly climate-sensitive region. However, the sparse and uneven distribution of ground-based meteorological stations across Sudan limits the accurate reconstruction of historical precipitation records and constrains the assessment of climate-related risks (Funk et al. 2015).

Global Climate Models (GCMs), including those developed under the Coupled Model Intercomparison Project Phase 6 (CMIP6), provide valuable insights into past and future climate conditions. Nonetheless, these models often exhibit systematic biases when simulating regional precipitation, particularly in arid and

semi-arid regions (Eyring et al. 2016). Such biases can significantly affect the reliability of model-based precipitation estimates and increase uncertainties in hydrological modeling and climate impact assessments. To overcome these limitations, bias correction techniques are widely applied to statistically adjust GCM outputs, aligning them more closely with observed data (Gudmundsson et al. 2012; Maraun 2013).

Despite the growing use of bias correction methods, comprehensive evaluations focusing specifically on Sudan remain scarce (Gebrechorkos et al. 2019). The country's steep climatic gradients and high spatial and temporal rainfall variability pose unique challenges for model calibration and correction. While studies across East Africa have shown that bias adjustment improves model performance, systematic assessments for Sudan, where observational networks are particularly limited, are still lacking. This gap highlights the need for detailed regional analyses to identify the most effective bias correction techniques for improving precipitation simulations and supporting climate resilience planning (Siddig et al. 2022).

2. Objectives and scope

Bias correction techniques enhance the reliability of climate model outputs by reducing systematic errors and improving alignment with observed climatology. Such adjustments are especially important for General Circulation Model (GCM) analyses, where uncorrected biases can substantially limit the usefulness of model projections. This study evaluates the performance of four widely used bias correction methods: Empirical Quantile Mapping (EQM), Gamma Quantile Mapping (Gamma-QM), Local Intensity Scaling (LOCI), and the Delta Method. These methods were applied to monthly precipitation simulations from ten CMIP6 models over Sudan during the 1991-2014 historical period. The Climate Hazards Group InfraRed Precipitation with Station data (CHIRPS) is the observational benchmark for assessing each method's effectiveness. Model performance is quantified using multiple complementary statistical metrics, including the Pearson correlation coefficient, centered root-mean-square deviation (CRMSD), mean bias, and Kling–Gupta Efficiency (*KGE*). In addition to evaluating bias correction methods, the study identifies the best-performing CMIP6 models for annual and seasonal (March-May and June-September) periods, providing guidance on the most reliable simulations for capturing spatial and temporal precipitation variability across Sudan. This study is novel in its regional focus on Sudan and in systematically comparing quantile-based and scaling-based bias correction techniques. By integrating statistical performance metrics with spatial diagnostics, it enables a comprehensive evaluation of model performance, thus providing practical guidance for applying bias correction and selecting appropriate climate models for hydroclimatic studies across East Africa.

3. Study area and data

3.1. Study area

This study focuses on Sudan, the third-largest country in Africa, located between approximately 8°–23.5°N and 21°E–39°E. The country exhibits a pronounced climatic gradient, transitioning from hyper-arid desert conditions in the north to semi-arid and savanna environments in the south (Fig. 1), with eleva-

tion decreasing from the highlands in the east and south to the northern plains. Correspondingly, precipitation patterns are highly variable across the country, with northern regions receiving little rainfall and southern regions experiencing substantially higher totals, as shown by CHIRPS observations.

Rainfall in Sudan is strongly seasonal, primarily driven by the north-south migration of the Intertropical Convergence Zone (ITCZ), with most precipitation occurring between June and September (Nicholson 2018; RCCC 2022). This spatial and temporal variability has important implications for agriculture, water resources, and disaster risk management. Northern Sudan frequently faces prolonged droughts, while southern areas are more susceptible to intense rainfall events that can trigger seasonal flooding (RCCC 2022).

Sudan's sensitivity to climate variability and change, combined with environmental and socio-economic pressures, makes it a valuable case study for evaluating climate models and assessing the effectiveness of bias correction techniques in reproducing historical precipitation patterns (Jackson et al. 2020).

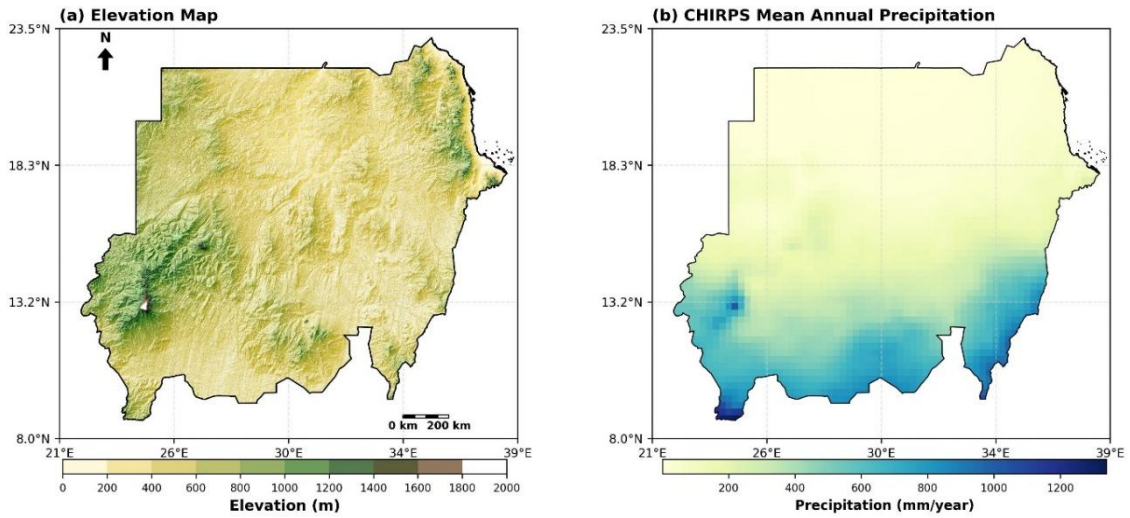

Fig. 1. Maps of Sudan with geographical coordinates. Panel (a) shows the shaded-relief elevation derived from the digital elevation model (DEM), and panel (b) shows the mean annual precipitation (mm/year) from CHIRPS, averaged over 1991-2014 at 0.25° spatial resolution.

3.2. Data

This study employs both observational and climate model datasets to evaluate bias correction techniques for monthly precipitation over Sudan. Observational data are sourced from the CHIRPS dataset, a high-resolution gridded product that integrates satellite-derived precipitation estimates with in-situ rain gauge measurements (Funk et al. 2015). CHIRPS provides near-global coverage at 0.05° spatial resolution, making it particularly valuable in regions with sparse or unevenly distributed observational networks, such as Sudan (Nicholson 2018; ICPAC 2020). Its reliability has been demonstrated in multiple studies across East Africa, including evaluations of historical precipitation variability, seasonal rainfall patterns, and extreme events, establishing CHIRPS as a robust benchmark for climate model evaluation in the region (ICPAC 2020).

For this analysis, monthly CHIRPS precipitation data from January 1991 to December 2014 were aggregated to a 0.25° resolution to match the climate model outputs. Precipitation values are expressed in mm month^{-1}, and the data were spatially clipped to Sudan's national boundaries using a country-level shapefile. The combination of high spatial resolution, integration of ground-based observations, and demonstrated reliability makes CHIRPS a suitable reference for assessing CMIP6 precipitation simulations and the effectiveness of bias correction techniques over Sudan. Although CHIRPS is available through 2020, the evaluation was restricted to 1991-2014 to align with the CMIP6 historical simulations.

Table 1. CMIP6 models used in this study, with their institutions, countries, approximate horizontal resolution, sensitivities and key reference.

No.	Model ID	Institute/Country	Resolution (°)	Sensitivity	Reference
1	AWI-CM-1-1-MR	Alfred Wegener Institute / Germany	~1.0°	Strong ocean–sea-ice coupling, affecting moisture transport and tropical rainfall.	Semmler et al. (2019)
2	EC-Earth3	EC-Earth Consortium / Europe	~1.0°	Updated convection and aerosol–cloud schemes, improving monsoon rainfall representation.	Döscher et al. (2022)
3	GFDL-ESM4	NOAA Geophysical Fluid Dynamics Laboratory / USA	~1.0°	Improved cloud microphysics, radiation, and land–atmosphere coupling shaping East African rainfall.	Held et al. (2019)
4	HadGEM3-GC31-LL	Met Office Hadley Centre / UK	~1.25°	Complex convection and cloud schemes; high sensitivity in ITCZ/tropical rainfall.	Williams et al. (2018)
5	INM-CM4-8	Institute for Numerical Mathematics / Russia	~2.0°	Simplified cloud and convection processes leading to weaker precipitation feedback.	Volodin et al. (2018)
6	KACE-1-0-G	Korea Meteorological Administration / South Korea	~1.25°	Updated KIM convection scheme enhancing tropical rainfall timing and intensity.	Byun et al. (2019)
7	MIROC6	AORI / NIES / JAMSTEC / Japan	~1.4°	Enhanced entrainment–detrainment convection, improving monsoon precipitation.	Tatebe et al. (2019)
8	MRI-ESM2-0	Meteorological Research Institute / Japan	~1.1°	Advanced cloud microphysics and precipitation formation, improving rainfall distribution.	Yukimoto et al. (2019)
9	NESM3	Nanjing Univ. of Information Science / China	~1.0°	Strong cloud feedback and updated boundary-layer scheme affecting monsoon variability.	Cao et al. (2018)
10	TaiESM1	Research Center for Environmental Changes / Taiwan	~1.0°	Enhanced aerosol–cloud–convection interactions influencing spatial rainfall patterns.	Lee et al. (2020)

Climate data were obtained from ten carefully selected CMIP6 global climate models, chosen based on spatial resolution, data availability, and relevance to East Africa (Eyring et al. 2016). Model outputs were converted to mm month^{-1}, regridded to 0.25° spatial resolution, and clipped to Sudan's national boundary to ensure consistency with CHIRPS observations (Gudmundsson et al. 2012). These ten models correspond to a subset of 23 CMIP6 models previously evaluated over the IGAD region, including Sudan, and identified in the literature as demonstrating relatively high skill in reproducing precipitation totals, seasonal cycles, and extreme events (Ayugi et al. 2022). Their documented performance makes them particularly suitable for climate impact assessments and hydrological studies in the region.

4. Methodology

4.1. Bias correction methods

To address systematic biases in CMIP6 precipitation outputs, four bias correction techniques were applied at a monthly time scale: Empirical Quantile Mapping (EQM), Gamma Quantile Mapping (Gamma-QM), Local Intensity Scaling (LOCI), and the Delta Method. These methods span both parametric and non-parametric approaches, capturing a broad methodological spectrum relevant to precipitation adjustment (Teutschbein, Seibert 2012).

Empirical Quantile Mapping (EQM)

EQM is a non-parametric bias correction approach that aligns the empirical cumulative distribution function (CDF) of the simulated precipitation with that of the observations (Maraun 2016). The corrected precipitation is computed as:

$$P_{corrected} = F_{obs,emp}^{-1}\left[F_{mod,emp}(P_{raw})\right] \quad (1)$$

where $F_{mod,emp}$ and $F_{obs,emp}^{-1}$ represent the empirical CDF of the model and the inverse empirical CDF of the observations, respectively.

Gamma Quantile Mapping (Gamma-QM)

Gamma-QM is a parametric technique that assumes precipitation follows a gamma distribution.
The distribution parameters are estimated via maximum likelihood for both model and observations.
The correction is expressed as:

$$P_{corrected} = F_{obs,\Gamma}^{-1}\left[F_{mod,\Gamma}(P_{raw})\right] \quad (2)$$

where $F_{\mathrm{mod},\Gamma}$ and $F_{\mathrm{obs},\Gamma}^{-1}$ denote the gamma CDF of the modeled and observed precipitation, respectively. This method preserves the skewness typical of precipitation distributions (Li et al. 2010).

Local Intensity Scaling (LOCI)

LOCI preserves the occurrence of dry months while correcting precipitation intensity. For months where $P_{raw} < T$ (with $T = 1$ mm/month in this study), precipitation remains zero; otherwise, it is scaled by:

$$P_{\text{corrected}} = \begin{cases} 0, & P_{raw} < T \\ P_{raw} \times F, & P_{raw} \geq T \end{cases} \quad (3)$$

where the scaling factor is:

$$F = \frac{\mu_{\mathrm{obs},>T}}{\mu_{\mathrm{mod},>T}} \quad (4)$$

where $\mu_{obs,>T}$ and $\mu_{mod,>T}$ are the wet-month average precipitation values from observations and models, respectively (Schmidli et al. 2006). This approach preserves dry-month statistics, corrects systematic intensity biases, and is particularly suitable for arid and semi-arid regions such as Sudan.

Delta Method

A straightforward bias adjustment method applying a monthly multiplicative correction:

$$P_{corrected} = P_{raw} \times \frac{\overline{P}_{obs}}{\overline{P}_{mod}} \quad (5)$$

where $\overline{P}_{mod}$ and $\overline{P}_{mod}$ are the long-term monthly means from observations and the model, respectively. Only wet months (≥0.001 mm/month) are adjusted, thereby preserving the dry-season structure (Hay et al. 2000; Teutschbein, Seibert 2012).

4.2. Performance evaluation metrics

To quantify the effectiveness of the bias correction techniques, a set of complementary statistical measures was employed to compare simulated precipitation against the CHIRPS observational reference. The Pearson correlation coefficient (r) evaluates the strength and direction of the linear association between modeled and observed values. The Root Mean Square Error ($RMSE$) captures the overall magnitude of deviations, reflecting the typical difference between simulations and observations. The Mean Bias (MB) indicates the systematic tendency of models to overestimate or underestimate precipitation relative to observations.

The Pearson correlation coefficient (r) quantifies the strength and direction of the linear relationship between simulated (x_i) and observed (y_i) precipitation:

$$r = \frac{\sum_{i=1}^{n}(x_i-\bar{x})(y_i-\bar{y})}{\sqrt{\sum_{i=1}^{n}(x_i-\bar{x})^2}\sqrt{\sum_{i=1}^{n}(y_i-\bar{y})^2}} \quad (6)$$

where $(\bar{x})$ and $(\bar{y})$ are the mean values of the simulated and observed precipitation, respectively. This metric evaluates the temporal agreement between simulations and observations.

The Root Mean Square Error ($RMSE$) provides a measure of the average magnitude of deviations between simulations and observations, reflecting the overall accuracy of the model:

$$\mathrm{RMSE} = \sqrt{\frac{1}{n}\sum_{i=1}^{n}(x_i - y_i)^2} \quad (7)$$

The Mean Bias (MB) indicates systematic overestimation or underestimation by the model:

$$MB = \frac{1}{n}\sum_{i=1}^{n}(x_i - y_i) \quad (8)$$

A key integrative metric, the Kling–Gupta Efficiency (*KGE*), synthesizes three critical aspects of a model: performance correlation, variability, and mean bias, into a single score. Using the revised formulation (Kling et al. 2012), the *KGE* is calculated as:

$$KGE = 1 - \sqrt{(r-1)^2 + (\alpha-1)^2 + \left(\frac{\sigma_{sim}/\mu_{sim}}{\sigma_{obs}/\mu_{obs}} - 1\right)^2} \quad (9)$$

Here, $\boldsymbol{r}$ represents the Pearson correlation coefficient, which quantifies the linear association between simulated and observed precipitation. The term $\boldsymbol{\alpha} = \frac{\boldsymbol{\sigma}_{\text{sim}}}{\boldsymbol{\sigma}_{\text{obs}}}$ denotes the variability ratio, reflecting the relative spread of simulated precipitation compared to observations. The third component, expressed as $\frac{\boldsymbol{\sigma}_{\text{sim}}/\boldsymbol{\mu}_{\text{sim}}}{\boldsymbol{\sigma}_{\text{obs}}/\boldsymbol{\mu}_{\text{obs}}}$, is the ratio of the coefficients of variation (*CV*) of simulated to observed precipitation, thereby incorporating the combined influence of variability and bias. This formulation ensures that deviations in correlation, variability, or normalized variability (via *CV* ratio) are equally weighted, providing a more balanced assessment of model performance.

4.3. Uncertainty quantification and robustness assessment

To assess the reliability of the performance metrics and the robustness of bias correction methods, a non-parametric bootstrapping approach was implemented with 1,000 resampled datasets to estimate 95% confidence intervals, providing a rigorous evaluation of statistical uncertainty for each metric (Efron, Tibshirani 1993). In addition, sensitivity analyses were conducted to examine both seasonal (March-May and June-September) and spatial variability in method performance across Sudan (Saltelli et al. 2008). Statistical significance testing was applied to determine whether observed improvements in bias-corrected outputs relative to raw simulations were meaningful, ensuring that conclusions drawn are robust and defensible (Wilks 2011).

5. Results

5.1. Model evaluation

The initial evaluation of raw CMIP6 precipitation simulations over Sudan was conducted through direct comparison with CHIRPS observational data for the period 1991-2014. Four complementary statistical metrics were computed to quantify model performance: Centered Root Mean Square Difference (CRMSD), mean bias, Pearson correlation coefficient (*r*), and Kling–Gupta Efficiency (Wilks 2011; Kling et al. 2012). CRMSD measures the magnitude of pattern errors after removing the mean bias, bias quantifies systematic overestimation or underestimation, the correlation coefficient assesses the temporal agreement between model and observations, and *KGE* integrates correlation, variability, and bias into a single skill metric.

Substantial variability was observed among the ten CMIP6 models when expressed relative to the CHIRPS mean precipitation. Correlation coefficients ranged from 0.72 to 0.95, with EC-Earth3 (r = 0.95), NESM3 (r = 0.93), INM-CM4-8 (r = 0.92), KACE-1-0-G (r = 0.92), and MIROC6 (r = 0.92) exhibiting

the strongest temporal agreement. Relative CRMSD values, expressed as a percentage of the CHIRPS mean, ranged between 10.87% (EC-Earth3) and 25.31% (MRI-ESM2-0), highlighting marked differences in the models' ability to reproduce observed temporal variability. Mean bias analysis revealed that most models tended to underestimate rainfall, particularly AWI-CM-1-1-MR (–28.45%), HadGEM3-GC31-LL (–22.50%), and KACE-1-0-G (–16.15%), whereas GFDL-ESM4 (+5.24%) and INM-CM4-8 (+2.28%) slightly overestimated precipitation. KGE scores ranged from 0.58 (MRI-ESM2-0) to 0.89 (EC-Earth3), emphasizing pronounced inter-model differences in overall simulation skill.

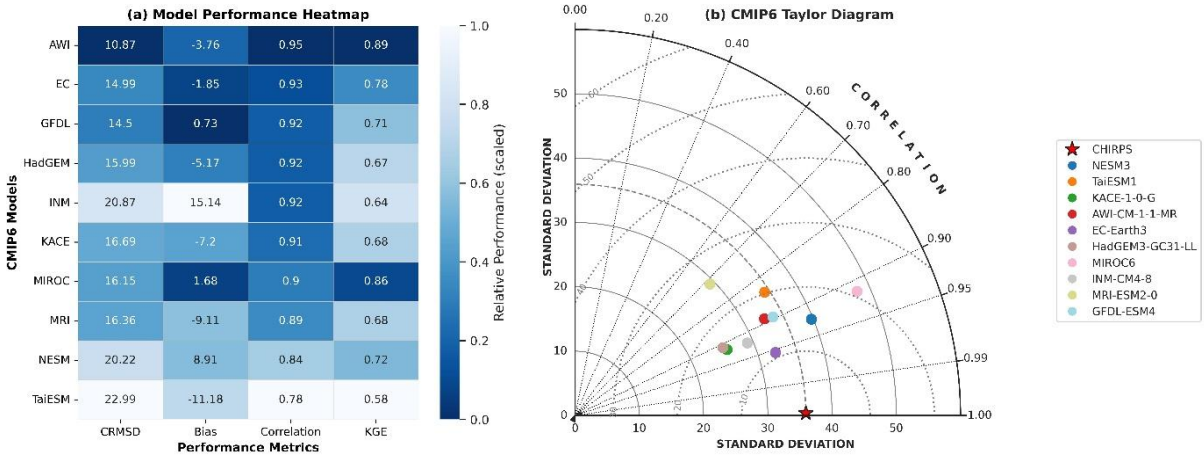

Fig. 2. CMIP6 model evaluation over Sudan (1991-2014). (a) Model Performance Heatmap: centered root-mean-square difference (CRMSD), mean bias magnitude, Pearson correlation coefficient (r), and Kling–Gupta Efficiency (*KGE*) for raw precipitation simulations. Metrics were rescaled to 011 to allow direct comparison; lighter colours indicate better relative performance. Original unscaled values are annotated within each cell. (b) CMIP6 Taylor Diagram: standard deviation, correlation coefficient, and CRMSD of each model relative to CHIRPS observations. Models closer to the reference point (CHIRPS) exhibit higher agreement in precipitation pattern and magnitude. EC-Earth3 achieved the highest correlation and lowest CRMSD, whereas MRI-ESM2-0 displayed the lowest correlation and highest CRMSD among the evaluated models.

These results are summarized in the heatmap presented in Figure 2a, which displays the four performance metrics for each model. To enable direct comparison across metrics with differing units and ranges, all values were rescaled to a standardized 0-1 scale, where lighter colours indicate better relative performance (i.e., lower CRMSD and bias magnitude, higher correlation and *KGE*), and darker colours denote poorer performance. Numeric annotations within each cell represent the original unscaled metric values. Complementing the heatmap, Figure 2b shows a Taylor diagram (Taylor 2001) that simultaneously illustrates the standard deviation, CRMSD, and correlation of each model relative to CHIRPS. Models positioned closer to the reference point indicate superior agreement with observed precipitation patterns and magnitudes. EC-Earth3 achieved both the highest correlation and the lowest CRMSD, indicating strong fidelity in reproducing observed variability. Conversely, MRI-ESM2-0 exhibited the weakest correlation and largest CRMSD, reflecting limited skill. Intermediate-performing models such as KACE-1-0-G, MIROC6, and

INM-CM4-8 clustered near the reference point, displaying modest pattern errors but satisfactory correlation strength.

Together, the heatmap and Taylor diagram provide a comprehensive assessment of raw CMIP6 precipitation performance over Sudan. The observed inter-model differences in magnitude, pattern, and combined skill metrics underscore the necessity for bias correction before employing these simulations for impact assessments or climate adaptation planning.

5.2. Bias characteristics

The raw CMIP6 ensemble precipitation over Sudan exhibits substantial annual, seasonal, and spatial biases relative to CHIRPS observations (Fig. 3). At the annual scale (ANN), the median bias is modestly positive at 7.14%, with a wide variability ranging from –82.20% to +100% (standard deviation: 48.01%). Overestimation dominates 60.4% of the country, primarily in the southern regions, while underestimation affects 39.6%, mainly across the northern and western arid zones. This indicates a spatially mixed bias pattern at the annual scale.

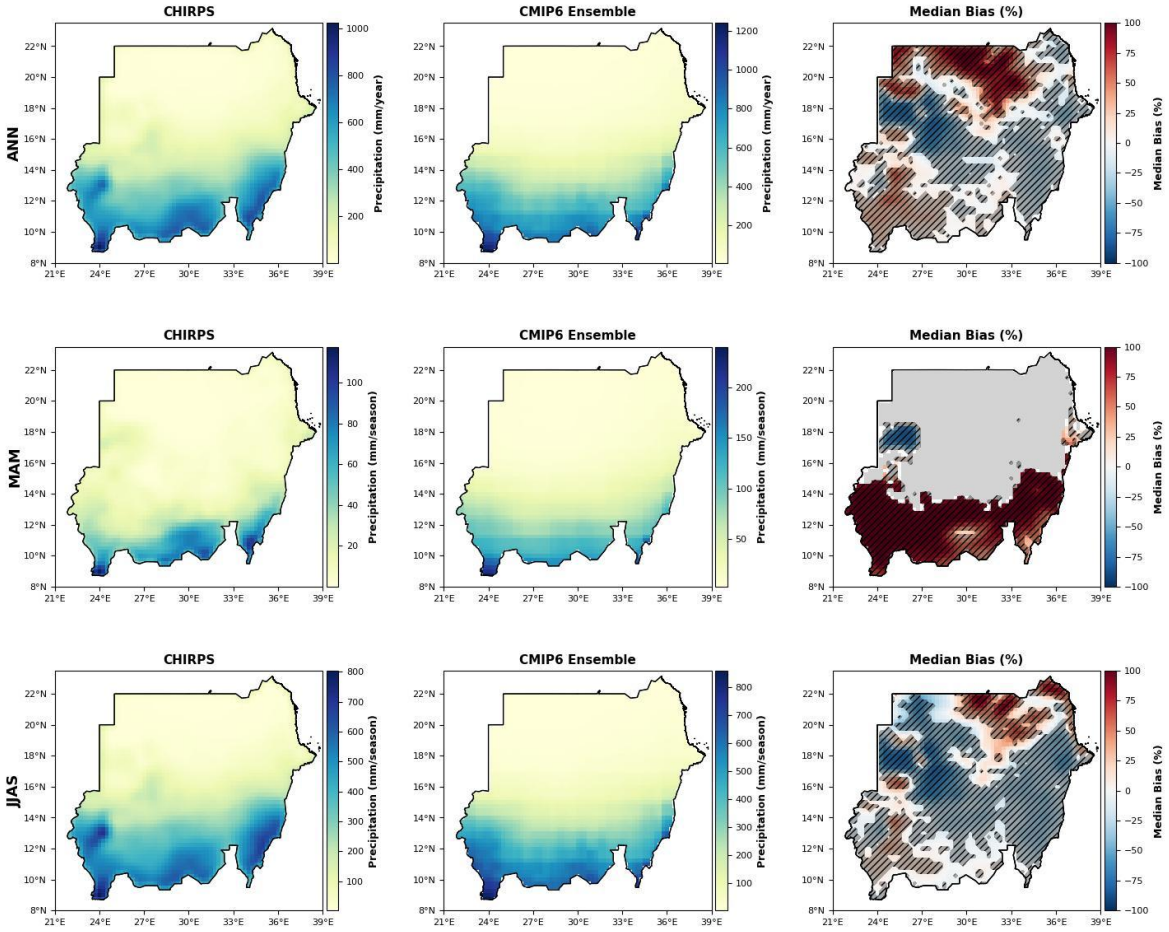

Fig. 3. Seasonal precipitation over Sudan for the annual (ANN), pre-monsoon (March-May; MAM), and monsoon (June-September; JJAS) seasons during 1991-2014. Panels from left to right show CHIRPS observations, raw CMIP6 ensemble mean precipitation, and the corresponding median bias (CMIP6 − CHIRPS) in percent (%). Hatching indicates areas where the bias is statistically significant ($p < 0.05$), determined using two-sample t-tests.

5.3. Bias correction effectiveness

The performance of four bias-correction techniques: Local Intensity Scaling (LOCI), Delta Change (Delta), Empirical Quantile Mapping (EQM), and Gamma Quantile Mapping (Gamma-QM) was assessed for ten CMIP6 precipitation models over Sudan during 1991-2014, using CHIRPS observations as the reference. Model fidelity was evaluated through Pearson correlation (r), Kling–Gupta Efficiency (*KGE*), and the centered root-mean-square difference (CRMSD). Figure 4 summarizes inter-model performance across methods. Both EQM and Gamma-QM deliver the strongest and most consistent improvements. Mean correlation (mean ± standard deviation across models) increases from 0.91 ± 0.01 in the raw ensemble to 0.98 ± 0.01 after EQM and 0.98 ± 0.01 after Gamma-QM. Correspondingly, mean CRMSD decreases from 17.7 ± 6.5 mm in the raw simulations to 7.7 ± 0.4 mm (EQM) and 7.9 ± 0.5 mm (Gamma-QM). The average *KGE* rises sharply from 0.72 ± 0.22 in the uncorrected models to 0.98 ± 0.01 following both quantile-based corrections, indicating a near-complete recovery of observed precipitation variability and bias structure. LOCI yields moderate but robust gains, increasing mean correlation to 0.96 ± 0.01 and *KGE* to 0.94 ± 0.03, while reducing CRMSD to 9.6 ± 1.1 mm. In contrast, the Delta method exhibits greater inter-model variability, with mean correlation 0.93 ± 0.06, mean *KGE* 0.91 ± 0.07, and CRMSD 12.7 ± 4.6 mm. Although Delta performs comparably to LOCI for several models, its linear scaling approach fails to capture nonlinear precipitation biases fully, resulting in less uniform improvements.

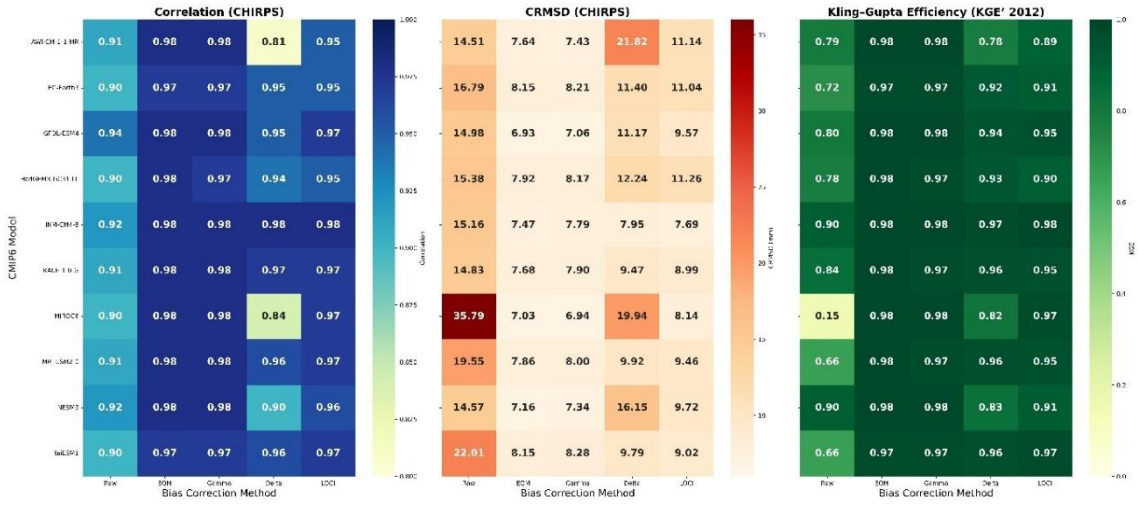

Fig. 4. Heatmaps illustrating Pearson correlation coefficient, Centered Root Mean Square Difference (CRMSD), and Kling–Gupta Efficiency (*KGE*) for ten CMIP6 climate models before and after bias correction by LOCI, Delta, EQM, and Gamma methods. Results are benchmarked against CHIRPS observations over Sudan (annual mean, 1991-2014). Superior performance is indicated by higher correlation and *KGE*, and lower CRMSD values, with EQM and Gamma methods showing consistently better skill.

Overall, these results demonstrate that quantile-based bias-correction approaches (EQM and Gamma-QM) are the most effective for CMIP6 precipitation simulations over Sudan. They minimize amplitude errors, enhance temporal coherence with CHIRPS observations, and substantially improve both statistical

reliability and physical realism. Such corrections are therefore essential for downstream hydrological and climate-impact analyses in the region.

5.4. Uncertainty assessment via bootstrapping

The robustness of each bias-correction method was evaluated using non-parametric bootstrapping with 1,000 replicates across three seasonal periods: annual, pre-monsoon, and monsoon. Four evaluation metrics were considered: bias, root mean square error (*RMSE*), Pearson correlation coefficient (*r*), and Kling–Gupta efficiency (*KGE*). The corresponding bootstrapped medians with 95% confidence intervals (*CI*s) are summarized in Table 2.

Table 2. Bootstrapped (median ±95% CI) evaluation of CMIP6 precipitation over Sudan for Raw and bias-corrected methods (Delta, EQM, Gamma-QM, LOCI) across ANN, MAM, and JJAS periods. Metrics shown include Kling–Gupta Efficiency (*KGE*), *RMSE*, Bias, and ΔBias (%), which represents the percentage reduction in absolute bias relative to the Raw simulation.

Method	Period	*KGE*	*RMSE*	Bias	ΔBias (%)
Raw	ANN	0.78 (0.00–0.93)	14.17 (11.79–39.55)	−0.48 (−7.54–18.91)	0
Delta	ANN	0.98 (0.81–0.99)	2.19 (1.27–19.36)	0.11 (−3.62–1.05)	77
EQM	ANN	1.00 (0.99–1.00)	0.11 (0.04–0.64)	−0.03 (−0.34–−0.01)	94
Gamma	ANN	1.00 (0.99–1.00)	0.13 (0.02–1.33)	0.03 (−0.02–0.41)	94
LOCI	ANN	0.98 (0.92–1.00)	1.65 (0.87–3.83)	−0.54 (−2.70–0.19)	−13
Raw	MAM	0.41 (0.00–0.83)	16.52 (11.13–42.07)	5.18 (−9.40–23.90)	0
Delta	MAM	0.99 (0.72–1.00)	0.78 (0.08–15.14)	−0.14 (−3.24–−0.01)	97
EQM	MAM	1.00 (0.96–1.00)	0.05 (0.01–1.55)	−0.02 (−0.74–−0.01)	100
Gamma	MAM	1.00 (0.99–1.00)	0.09 (0.03–0.73)	0.02 (−0.07–0.13)	100
LOCI	MAM	0.95 (0.76–0.99)	2.03 (1.33–7.12)	−0.03 (−4.50–1.10)	99
Raw	JJAS	0.81 (0.19–0.90)	37.21 (27.57–75.34)	−8.33 (−22.85–35.53)	0
Delta	JJAS	0.99 (0.84–1.00)	1.82 (0.08–39.68)	−0.52 (−7.99–−0.02)	94
EQM	JJAS	1.00 (1.00–1.00)	0.31 (0.01–0.89)	−0.07 (−0.35–0.00)	99
Gamma	JJAS	1.00 (1.00–1.00)	0.13 (0.03–0.40)	0.00 (−0.06–0.16)	100
LOCI	JJAS	0.97 (0.95–1.00)	3.98 (0.93–5.95)	−1.68 (−3.26–0.24)	80

The bootstrapped results indicate that quantile-based methods (EQM and Gamma-QM) consistently achieve the highest reduction in absolute bias (ΔBias %) across all seasons. For the annual period, EQM achieved the largest improvement with ΔBias = 94%, closely followed by Gamma-QM (ΔBias = 94%). During the pre-monsoon season, both EQM and Gamma-QM fully corrected the mean bias (ΔBias = 100%), reflecting near-perfect alignment with CHIRPS observations. In the monsoon period, Gamma-QM slightly outperformed EQM (ΔBias = 100% vs. 99%), demonstrating robust performance during the main rainy season.

Other methods, such as LOCI and Delta, generally improved model performance but were less consistent. Notably, LOCI slightly increased the absolute bias in the annual period (ΔBias = –13%). Overall, these findings highlight the superiority of EQM and Gamma-QM for correcting precipitation biases in regions with complex seasonal variability, such as Sudan, while simultaneously improving *KGE*, *RMSE*, and bias relative to the raw CMIP6 simulations.

5.5. Annual and seasonal evaluation

Figure 5 presents the spatial distribution of seasonal precipitation biases for the ensemble raw and EQM-corrected CMIP6 simulations over Sudan, including maps of bias differences and the statistical significance of the corrections. The raw simulations reveal a mean annual bias close to zero, with a median of 2.16% and substantial spatial heterogeneity (standard deviation: 69.69%). During March-May, biases are dominated by overestimation, with a median of 8.86% and standard deviation of 23.64%, while the June-September period exhibits underestimation, with a median of –6.31% and a standard deviation of 65.22%. Following EQM bias correction, median biases across all seasons are effectively reduced nearly to zero (March-May: –0.21%, June-September: –0.15%, annual: –0.71%), and the spread of residual biases is substantially narrowed (EQM standard deviations: annual 1.01%, March-May 0.43%, June-September 0.71%). The ΔBias (%), representing the relative improvement after EQM correction, shows a median reduction of 96.18% for the annual period, 98.42% for March-May, and 98.75% for June-September, indicating a marked enhancement in model-observation agreement.

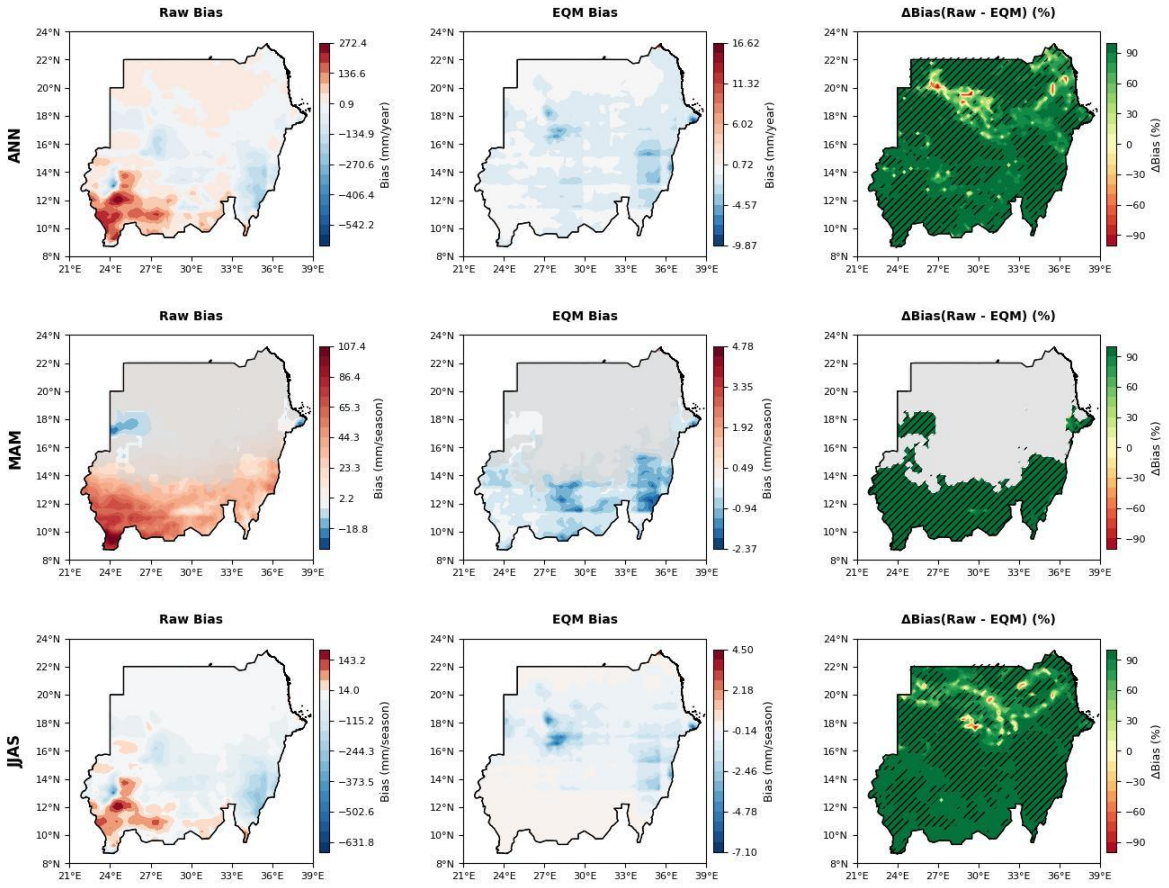

Fig. 5. Spatial distribution of annual and seasonal precipitation biases over Sudan (1991-2014) for the ensemble raw CMIP6 simulations and EQM bias-corrected outputs. Columns represent (from left to right) the raw bias, EQM-corrected bias, and the percentage reduction in bias (ΔBias %) following EQM correction. Units are mm/year for the annual (ANN) row and mm/season for seasonal rows (MAM: March–May, JJAS: June–September). Grey shading in MAM highlights arid northern and central regions with observed precipitation below 10 mm/season, excluded from the ΔBias calculation. Hatching indicates areas where bias reduction is statistically significant ($p < 0.05$).

The observed seasonal biases likely arise from a combination of factors inherent to global climate models, including limitations in convective parameterizations, representation of orographic effects, and model resolution constraints, all of which influence the simulation of precipitation intensity and spatial distribution. The pronounced overestimation during the pre-monsoon season may reflect difficulties in simulating the onset of the rainy season, whereas the underestimation during the monsoon season could be related to deficiencies in representing the full intensity and extent of monsoonal rainfall.

While the EQM bias correction method substantially mitigates these systematic biases, it is important to note that bias correction techniques primarily adjust the statistical properties of model outputs and do not address the underlying model physics. Consequently, residual biases and uncertainties may persist, especially under future climate conditions or outside the calibration period. Moreover, the spatial patterns of bias correction effectiveness vary, emphasizing the need for continued model development alongside the application of bias correction approaches.

5.6. Evaluation of model performance

The performance of ten CMIP6 models in reproducing observed precipitation climatology over Sudan was evaluated for annual and seasonal periods. Empirical Quantile Mapping (EQM) was applied to assess its influence on model fidelity. Model skill was quantified using correlation, centered root-mean-square difference expressed as a percentage of observed mean precipitation (CRMSD%) and normalized standard deviation relative to CHIRPS. Both raw and EQM-corrected simulations were analyzed to determine the magnitude of improvement following bias correction.

At the annual scale, EQM substantially reduces model errors, with CRMSD decreases ranging from 35% to 48% compared to the raw simulations (Fig. 6a). EC-Earth3, GFDL-ESM4, and INM-CM4-8 exhibit the strongest improvements, achieving correlations of 0.97 and CRMSD values below 10% of the observed annual mean, indicating a highly realistic representation of spatial rainfall variability.

During the pre-monsoon season, model performance shows greater variability (Fig. 6b). EQM reduces CRMSD for all models, with the best-performing models (NESM3, EC-Earth3, and GFDL-ESM4) achieving CRMSD levels of 12-18% of observed seasonal precipitation and correlations between 0.81 and 0.91. These results highlight the effectiveness of EQM in correcting models that initially underestimated early-season rainfall.

For the main monsoon season, EQM correction again improves simulation fidelity (Fig. 6c). EC-Earth3, GFDL-ESM4, and INM-CM4-8 continue to rank highest, with correlations of 0.87-0.88 and CRMSD values of 15-20% relative to CHIRPS. Although correlations are slightly lower than at the annual scale, these models consistently capture the spatial distribution of monsoon rainfall.

Overall, converting the evaluation to a percentage-based framework demonstrates that EQM significantly enhances CMIP6 precipitation simulations by reducing systematic biases and improving spatial pattern agreement across Sudan's diverse climatic zones.

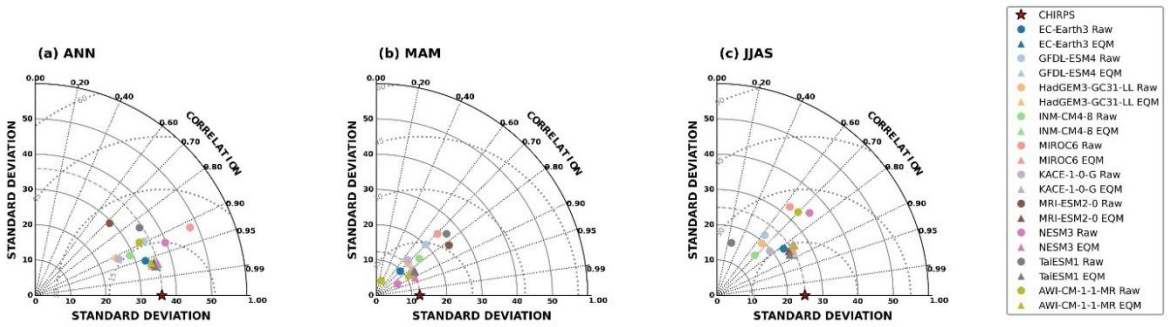

Fig. 6. Taylor diagrams for ten CMIP6 models before and after EQM bias correction during (a) annual, (b) March-May, (c) June-September. Each diagram compares model performance with CHIRPS precipitation over Sudan in terms of correlation (radial distance), CRMSD (curved distance from the reference point), and standard deviation (distance from the origin). Star markers denote CHIRPS; circles represent raw models; triangles represent EQM-corrected models.

Overall, the Taylor diagram analysis (Fig. 6) demonstrates that EQM bias correction substantially improves the statistical agreement of CMIP6 ensemble simulations with observations across all seasons. EC-Earth3, GFDL-ESM4, and INM-CM4-8 are consistently the top performers annually and during the monsoon season, while NESM3 excels during the pre-monsoon season. These results highlight both the effectiveness of statistical bias correction and the relative strengths of individual models in capturing seasonal precipitation dynamics over Sudan.

6. Discussion

The evaluation of CMIP6 precipitation simulations over Sudan reveals substantial variability in model skill, highlighting the challenges of representing rainfall in arid and semi-arid climates. Raw model outputs exhibit systematic biases, often overestimating rainfall during the pre-monsoon season and underestimating it during the main monsoon (Ayugi et al. 2022; Omay et al. 2023). Although annual biases appear smaller on average, they conceal significant spatial heterogeneity, reflecting compensating errors across northern, central, and southern Sudan. These discrepancies indicate that even the latest CMIP6 models struggle to capture convective rainfall initiation, monsoon propagation, and regional orographic influences: issues that have been documented in other CMIP6 evaluation studies (Vogel et al. 2018; Toolan et al. 2025).

Application of bias correction methods markedly improves simulation fidelity, although effectiveness varies by technique and season. Quantile-based approaches consistently produce the largest reductions in bias while improving temporal correlation and overall model performance (Ayugi et al. 2022; Tiku et al. 2025). These methods effectively mitigate seasonal biases during MAM and JJAS, reducing annual biases substantially. In contrast, simpler methods with linear or intensity-scaling assumptions achieve only moderate improvements and fail to capture the nonlinearity of precipitation distributions during early-season rainfall (Switanek et al. 2017). These findings underscore the importance of advanced, distribution-focused bias correction in regions with highly seasonal and spatially variable rainfall.

Spatially explicit analyses further demonstrate that bias correction reduces not only the magnitude of errors but also improves the representation of precipitation variability in regions critical for water resources and agriculture. By excluding arid northern areas with negligible precipitation (<40% of the seasonal mean), and focusing on statistically significant improvements, this study ensures that methodological enhancements are both hydrologically meaningful and regionally robust. Such a spatially refined evaluation represents an advancement over prior studies, which often assess only mean biases without accounting for spatial heterogeneity or significance (Ayugi et al. 2022; Omay et al. 2023).

Finally, integrating bias reduction with rigorous model evaluation helps identify both the most reliable models and the most effective correction methods. This framework demonstrates that even after statistical correction, intrinsic model characteristics continue to influence seasonal performance. By combining bias correction with model skill assessment, this study provides a robust approach for improving precipitation simulations over Sudan and other regions with complex rainfall patterns (Tiku et al. 2025).

7. Conclusions

This study evaluated the performance of multiple bias correction techniques – LOCI, Delta, EQM, and Gamma-QM – in improving CMIP6 precipitation simulations over Sudan for 1991-2014, using CHIRPS observations as the reference. Raw CMIP6 models exhibited systematic spatial biases, primarily linked to misrepresentation of the Intertropical Convergence Zone (ITCZ) and limitations in convective parameterizations.

Among the tested methods, quantile-based approaches (EQM and Gamma-QM) consistently achieved the largest improvements across statistical metrics (correlation, CRMSD, bias, and *KGE*), reducing mean bias by up to 90 % and enhancing temporal agreement with observations. LOCI and Delta methods provided moderate improvements, largely correcting mean precipitation, but were less effective in capturing distributional variability. Bias correction effectiveness varied seasonally and spatially, performing best in humid southern regions and during the monsoon season, while residual uncertainties persisted in arid northern areas due to low rainfall and observational limitations.

By integrating multi-metric evaluation, robust bootstrapping, and spatially explicit significance testing, this study demonstrates that advanced, distribution-focused bias correction substantially enhances model fidelity, reproducing realistic spatial and temporal variability across annual and seasonal timescales. These findings provide clear guidance for selecting reliable models and appropriate correction techniques in climate impact assessments and water-resource planning.

Future work should extend these approaches to daily-scale analyses, incorporate multi-reference datasets, and explore dynamical downscaling or hybrid correction frameworks to further improve model realism under changing climate conditions, and to assess the persistence of correction effectiveness under non-stationary climates.

References

Ayugi B.O., Shilenje Z.W., Babaousmail H., Lim Kam Sian K.T.C., Mumo R., Dike V.N., Iyakaremye V., Chehbouni A., Ongoma V., 2022, Projected changes in meteorological drought over East Africa inferred from bias-adjusted CMIP6 models, Natural Hazards, 113 (2), 1151-1176, DOI: 10.1007/s11069-022-05341-8.

Byun Y.-H., Lim Y.-J., Sung H.-M., Kim J., Sun M., Kim B.-H., Lee J.-H., Moon H., 2019, NIMS-KMA KACE1.0-G model output prepared for CMIP6 CMIP historical, Earth System Grid Federation, DOI: 10.22033/ESGF/CMIP6.8378.

Cao J., Wang B., Yang Y.-M., Ma L., Li J., Sun B., Bao Y., He J., Zhou X., Wu L., 2018, The NUIST Earth System Model (NESM) version 3: Description and preliminary evaluation, Geoscientific Model Development, 11 (7), 2975-2993, DOI: 10.5194/gmd-11-2975-2018.

Döscher R., Acosta M., Alessandri A., Anthoni P., Arsouze T., Bergman T., Bernardello R., Boussetta S., Caron L,-P., Carver G., Castrillo M., Catalano F., Cvijanovic I., Davini P., Dekker E., Doblas-Reyes F.J., Docquier D., Echevarria P., Fladrich U., Fuentes-Franco R., Gröger M., v. Hardenberg J., Hieronymus J., Pasha Karami M., Keskinen J.-P., Koenigk T., Makkonen R., Massonnet F., Ménégoz M., Miller P.A., Moreno-Chamarro E., Nieradzik L., van Noije T., Nolan P., O'Donnell D., Ollinaho P., van den Oord G., Ortega P., Tintó Prims O., Ramos A., Reerink T., Rousset C., Ruprich-Robert Y., Le Sager P., Schmith T., Schrödner R., Serva F., Sicardi V., Sloth Madsen M., Smith B., Tian T., Tourigny E., Uotila P., Vancoppenolle M., Wang S., Wårlind D., Willén U., Wyser K., Yang S., Yepes-Arbós X., Zhang Q., 2022, The EC-Earth3 Earth system model for the Coupled Model Intercomparison Project 6, Geoscientific Model Development, 15 (1), 2973-3020, DOI: 10.5194/gmd-15-2973-2022.

Efron B., Tibshirani R.J., 1993, An Introduction to the Bootstrap, Chapman & Hall/CRC, New York, 456 pp., DOI: 10.1201/9780429246593.

Eyring V., Bony S., Meehl G.A., Senior C.A., Stevens B., Stouffer R.J., Taylor K.E., 2016, Overview of the Coupled Model Intercomparison Project Phase 6 (CMIP6) experimental design and organization, Geoscientific Model Development, 9 (5), 1937-1958, DOI: 10.5194/gmd-9-1937-2016.

Funk C., Peterson P., Landsfeld M., Pedreros D., Verdin J., Shukla S., Husak G., Rowland J., Harrison L., Hoell A., Michaelsen J., 2015, The climate hazards infrared precipitation with stations – a new environmental record for monitoring extremes. Scientific Data, 2, DOI: 10.1038/sdata.2015.66.

Gebrechorkos S.H., Hülsmann S., Bernhofer C., 2019, Long-term trends in rainfall and temperature using high-resolution climate datasets in East Africa, Scientific Reports, 9, DOI: 10.1038/s41598-019-47933-8.

Gudmundsson L., Bremnes J.B., Haugen J.E., Engen-Skaugen T., 2012, Technical note: Downscaling RCM precipitation to the station scale using statistical transformations – a comparison of methods, Hydrology and Earth System Sciences, 16 (9), 3383-3390, DOI: 10.5194/hess-16-3383-2012.

Hay L.E., Wilby R.L., Leavesley G.H., 2000, A comparison of delta change and downscaled GCM scenarios for three mountainous basins in the United States, Journal of the American Water Resources Association, 36 (2), 387-397, DOI: https://doi.org/10.1111/j.1752-1688.2000.tb04276.x.

Held I.M., Gou H., Adcroft A., Dunne J.P., Horowitz L.W., Krasting J., Shevliakova E., Winton M., Zhao M., Bushuk M., Wittenberg A.T., Wyman B., Xiang B., Zhang R., Anderson W., Balaji V., Donner L., Dunne K., Durachta J., Gauthier P.P.G., Ginoux P., Golaz J.-C., Griffies S.M., Hallberg R., Harris L., Harrison M., Hurlin W., John J., Lin P., Lin S.-J., Malyshev S., Menzel R., Milly P.C.D., Ming Y., Naik V., Paynter D., Paulot F., Ramaswamy V., Reichl B., Robinson T., Rosati A., Seman C., Silvers L.G., Underwood S., Zadeh N., 2019, Structure and performance of GFDL's CM4.0 climate model, Journal of Advances in Modeling Earth Systems, 11 (11), 3691-3727, DOI: 10.1029/2019MS001829.

ICPAC, 2020, State of the Climate of the Greater Horn of Africa 2020, IGAD Climate Prediction and Applications Centre, Nairobi, Kenya, available online at: https://www.icpac.net/ (data access 19.11.2025).

Jackson L.S., Declan L.F., Kendon E.J., Marsham H., Parker D.J., Stratton R.A., Tomassini L., Tucker S., 2020, The effect of explicit convection on couplings between rainfall, humidity, and ascent over Africa under climate change, Journal of Climate, 33 (19), 8315-8337, DOI: 10.1175/JCLI-D-19-0322.1.

Kling H., Fuchs M., Paulin M., 2012, Runoff conditions in the upper Danube basin under an ensemble of climate change scenarios, Journal of Hydrology, 424-425, 264-277, DOI: 10.1016/j.jhydrol.2012.01.011.

Lee W.-L., Wang Y.-C., Shiu C.-J., Tsai I., Tu C.-Y., Lan Y.-Y., Chen J.-P., Pan H.-L., Hsu H.-H., 2020, Taiwan Earth System Model Version 1: description and evaluation of mean state, Geoscientific Model Development, 13 (8), 3887-3904, DOI: 10.5194/gmd-13-3887-2020.

Li H., Sheffield J., Wood E.F., 2010, Bias correction of monthly precipitation and temperature fields from Intergovernmental Panel on Climate Change AR4 models using equidistant quantile matching, Journal of Geophysical Research: Atmospheres, 115 (D10), DOI: 1029/2009JD012882.

Maraun D., 2013, Bias correction, quantile mapping, and downscaling: revisiting the inflation issue, Journal of Climate, 26, 2137-2143, DOI: 10.1175/JCLI-D-12-00821.1.

Maraun D., 2016, Bias correcting climate change simulations – a critical review, Current Climate Change Reports, 2 (4), 211-221, DOI: 10.1007/s40641-016-0050-x.

Nicholson S.E., 2018, The ITCZ and the seasonal cycle over equatorial Africa, Bulletin of the American Meteorological Society, 99 (2), 337-348, DOI: 10.1175/BAMS-D-16-0287.1.

Omay P.O., Muthama N.J., Oludhe C., Kinama J.M., Artan G., Atheru Z., 2023, Evaluation of CMIP6 historical simulations over IGAD region of Eastern Africa, Discover Environment, 11 (1), DOI: 10.1007/s44274-023-00012-2.

RCCC, 2022, Sudan Climate Profile, Country-Level Summary, Red Cross Climate Centre, available online at https://www.climatecentre.org/wp-content/uploads/RCCC-Country-profiles-Sudan-2022-Final-1.pdf (data access 19.11.2025).

Saltelli A., Ratto M., Andres T., Campolongo F., Cariboni J., Gatelli D., Saisana M., Tarantola S., 2008, Global Sensitivity Analysis: The Primer, John Wiley & Sons, Chichester, UK, 292 pp., DOI: 10.1002/9780470725184.

Schmidli J., Frei C., Vidale P.L., 2006, Downscaling from GCM precipitation: a benchmark for dynamical and statistical downscaling methods, International Journal of Climatology, 26 (5), 679-689, DOI: 10.1002/joc.1287.

Semmler T., Danilov S., Rackow T., Sidorenko D., Barbi D., Hegewald J., Pradhan H.K., Sein D., Wang Q., Jung T., 2019, AWI AWI-CM1.1MR model output prepared for CMIP6 ScenarioMIP ssp370. World Data Center for Climate (WDCC) at DKRZ, DOI: WDCC/AR6.C6SPAWAWMs370.

Siddig M.S.A., Ibrahim S., Yu Q., Abdalla A., Osman Y., Atiem I.A., 2022, Bias adjustment of four satellite-based rainfall products using ground-based measurements over Sudan, Water, 14 (9), DOI: 10.3390/w14091475.

Switanek M. B., Troch P. A., Castro C. L., Leuprecht A., Chang H.-I., Mukherjee R., Demaria E.M., 2017, Scaled distribution mapping: a bias correction method that preserves raw climate model projected changes, Hydrology and Earth System Sciences, 21 (6), 2649-2666, DOI: 10.5194/hess-2016-435.

Tatebe H., Ogura T., Nitta T., Komuro Y., Ogochi K., Takemura T., Sudo K., Skiguchi M., Abe M., Saito F., Chikira M., Watanabe S., Mori M., Hirota N., Kawatani Y., Mochizuki T., Yoshimura K., Takata K., O'ishi R., Yamazaki D., Suzuki T., Kurogi M., Kataoka T., Watanabe M., Kimoto M., 2019, Description and basic evaluation of simulated mean state, internal variability, and climate sensitivity in MIROC6. Geoscientific Model Development, 12 (7), 2727-2765, DOI: 10.5194/gmd-12-2727-2019.

Taylor K.E., 2001, Summarizing multiple aspects of model performance in a single diagram, Journal of Geophysical Research: Atmospheres, 106 (D7), 7183-7192, DOI: 10.1029/2000JD900719.

Teutschbein C., Seibert J., 2012, Bias correction of regional climate model simulations for hydrological climate-change impact studies: Review and evaluation of different methods, Journal of Hydrology, 456-457, 12-29, DOI: 10.1016/j.jhydrol.2012.05.052.

Tiku T.W., Tarekegn G.B., Sahlu D., Tashebo G.B., Enyew F.B., Umer Y., Debele S.E., 2025, Evaluating CMIP6 precipitation simulations across different rainfall regimes in the Amhara region, Ethiopia, Theoretical and Applied Climatology, 5 (3), 689-704, DOI: 10.1016/j.nhres.2025.03.002.

Toolan C.A., Amooli J.A., Wilvox L.J., Samset B.H., Turenr A.G., Westervelt D.M., 2025, Strong intermodel differences and biases in CMIP6 simulations of PM2.5, aerosol optical depth, and precipitation over Africa, Atmospheric Chemistry and Physics, 25 (18), 10523-10557, DOI: 10.5194/acp-25-10523-2025.

Vogel P., Knippertz P., Fink A.H., Schlueter A., Gneiting T., 2018, Skill of global raw and postprocessed ensemble predictions of rainfall over northern tropical Africa, Weather and Forecasting, 33, 369-388, DOI: 10.1175/WAF-D-17-0127.1.

Volodin E.M., Mortikov E.V., Kostrykin S.V., Galin V.Y., Lykossov V.N., Gritsun A.S., Diansky N.A., Gusev A.V., Iakovlev N.G., Shestakova A.A., Emelina S.V., 2018, Simulation of the modern climate using the INM-CM48 climate model, Russian Journal of Numerical Analysis and Mathematical Modelling, 33 (6), 367-374, DOI: 10.1515/rnam-2018-0032.

Wilks D.S., 2011, Statistical Methods in the Atmospheric Sciences (3rd ed.). Academic Press, San Diego.

Williams K.D., Copsey D., Blockley E.W., Bodas-Salcedo A., Calvert D., Comer R., Davis P., Graham T., Hewitt H.T., Hill R., Hyder P., Ineson S., Johns T.C., Keen A.B., Lee R.W., Megann A., Milton S.F., Rae J.G.L., Roberts M.J., Scaife A.A., Schiemann R., Storkey D., Thorpe L., Watterson I.G., Walters D.N, West A., Wood R.A., Woolings R., Xavier P.K., 2018, The Met Office Global Coupled Model 3.0 and 3.1 (GC3.0 & GC3.1) configurations, Journal of Advances in Modeling Earth Systems, 10 (2), 357-380, DOI: 10.1002/2017MS001115.

Yukimoto S., Koshiro T., Kawai H., Koshiro T., Oshima N., Yoshida K., Urakawa S., Tsujino H., Deushi M., Tanaka T., Hosaka M., Yabu S., Yoshimura H., Shindo E., Mizuta R., Obata A., Adachi Y., Ishii M., 2019, The Meteorological Research Institute Earth System Model Version 2.0, MRI-ESM2.0: Description and Basic Evaluation of the Physical Component, Journal of the Meteorological Society of Japan, 97 (5), 931-965, DOI: 10.2151/jmsj.2019-051.

Assessment of climate change impacts on extreme precipitation in the Okpara Basin at Nanon (Benin)

Ezéchiel Obada[1,2], Halissou Yarou[1,2], Eliézer Iboukoun Biao[1,2], Freddy Zinsè Hounnondaho[1,3], Josué Zandagba[1,2], Adéchina Eric Alamou[1,2]

[1] Laboratoire de Géoscience, de l'Environnement et Applications (LaGEA), Université Nationale des Sciences, Technologies, Ingénierie et Mathématiques (UNSTIM), Bénin

[2] Laboratoire d'Hydrologie Appliquée (LHA), Institut Nationale de l'Eau (INE), UAC, Bénin

[3] Ecole Doctorale des Sciences, Technologies, Ingénierie et Mathématiques (ED-STIM), Université Nationale des Sciences, Technologies, Ingénierie et Mathématiques (UNSTIM), Bénin

Abstract

Extreme weather events have significant impacts on society, water resources, health, and agriculture. In this research, we analyze recent (1951-2020) and projected (2030-2099) trends in extreme precipitation indices within the Okpara Basin at the Nanon outlet. To achieve this, eight indices of extreme precipitation indices recommended by the Expert Team on Climate Change Detection and Indices (ETCCDI) were calculated using daily observations and outputs from SSP245 and SSP585 scenarios based on the AWI-CM, INM-CM, and EC-Earth3 models. The Mann-Kendall and Student's t-test methods were applied to examine trends and changes in time series of extreme indices. The findings reveal that over the historical period, consecutive wet days (CWD) and the number of wet days (R1mm) showed non-significant increasing trends. The consecutive dry days (CDD), RX5day, R95p, and R99p indices indicated non-significant downward trends. Over the projected period, the CWD and CDD indices exhibit downward or upward trends depending on the scenario and climate model: the RX1day, RX5day, R95p, R99p, R1mm, and PRCPTOT indices display upward trends for all scenarios and models. An intensification of wet conditions is therefore expected in the basin, and it is important for basin managers, planners, and decision-makers to develop strategies to prevent and properly manage possible water-related crises in the basin.

Key words

Extreme precipitation, climate change, climate models, SSP scenarios, Benin.

Submitted 17 May 2025, revised 25 September 2025, accepted 25 November 2025

DOI: 10.26491/mhwm/214714

1. Introduction

Long-term changes are coupled with extreme weather events, which are difficult to identify and classify, and therefore difficult to simulate and even more difficult to predict (Royer 2024). Climate events are classified as extreme when a meteorological or climatic variable exceeds (or falls below) a threshold close to the upper (or lower) limit of the range of values observed for that variable (ONERC 2018). Climate extremes and their impacts are now recognised as one of the greatest challenges facing the world through its people, environment, and economies (IPCC 2021).

Extreme precipitation has become increasingly frequent as the climate changes. These events have multiple impacts on humans and the environment. Extreme precipitation causes flooding, soil erosion, reduced agricultural productivity, and crop and livestock losses. It can also cause extensive damage to infrastructure, leading to economic losses and sometimes loss of life. Significant efforts have been made worldwide to anticipate the consequences of extreme precipitation. Future climate simulations under

various scenarios are developed to analyze future precipitation trends. These scenarios range from SRES (Special Report on Emission Scenarios) scenarios (IPCC 2007) to SSPs (Shared Socioeconomic Pathways) scenarios, including RCPs (Representative Concentration Pathways) scenarios. Numerous studies at global, regional, and local levels have examined trends and changes in precipitation and other meteorological variables using these simulations. Efforts have also been made to develop extreme climate indices. For example, the Expert Team on Climate Change Detection and Indices (ETCCDI) has recommended several extreme precipitation indices (Zhang et al. 2011). These indices have enabled significant progress in the study of the future climate.

In West Africa, Odoulami and Akinsanola (2018) detected a significant downward trend in the number of dry days and a significant upward trend in the number of wet days in the Sahel. Diatta et al. (2020) indicated a downward trend in dry conditions in the Sahel and Sahara, while an upward trend was observed in the west and south of the Sahel. Atiah et al. (2020) indicated a significant downward trend in wet indices around Lake Volta and in central Ghana, whereas upward trends were detected over northern Ghana. In Benin, Attogouinon et al. (2017) reported no strong trends in extreme precipitation indices in the upper Ouémé basin. N'tcha M'po et al. (2017) showed that the number of days with heavy and very heavy precipitation, the number of consecutive wet days, the number of wet days per year, and total precipitation are declining at most of the precipitation stations in the Ouémé basin. Hounguè et al. (2019) reported an intensification of heavy precipitation, a simple daily intensity index (SDII), and a decrease in consecutive wet days (CWD) on the Ouémé delta in Benin. Obada et al. (2021) studied the spatio-temporal variability of extreme precipitation across Benin. The intensification of these phenomena, coupled with constant population growth and urbanization, suggests that flooding in Benin's watersheds will worsen. However, these studies were based on observed data and simulations based on RCPs scenarios, and no study has been conducted on the future evolution of precipitation in the Okpara basin, despite its proven importance in supplying water to the city of Parakou. Shared Socioeconomic Pathways (SSPs) are climate change scenarios that describe alternative global socioeconomic futures up to 2100, detailing different trajectories for population, economic development, technology, and environmental policy. Combined with greenhouse gas emissions, they provide context for climate models and inform policy responses. As with the RCP scenarios, it is important to know: What is the trend in extreme precipitation in the Okpara basin under these scenarios? What are the changes in extreme precipitation indices compared to the recent past, and what are the implications for the environment and populations? The purpose of this study is to examine trends and changes in extreme precipitation indices in the Okpara basin in Nanon under SSP scenarios. This study is important because prior knowledge of the impact of climate change on extreme precipitation will raise awareness, lead to more rigorous climate change policies, and improve preparedness for the consequences of extreme precipitation. Knowledge of the impacts of climate change on extreme precipitation in the future would therefore be a major asset in the process of sustainable development and environmental protection in a region highly vulnerable to climate change.

2. Methods

2.1. Study area and data

The Okpara watershed at the Nanon outlet is characterized by a crystalline peneplain interspersed with hard-rock hills. It spans 2,070 km² and encompasses all or parts of five communes in the Borgou Department: Tchaourou, N'Dali, Pèrèrè, Nikki, and Parakou (PNE-Bénin 2008). Geographically, it is situated between 9°4'59" and 9°52'40.61" N, and 4°6'49.5" and 4°37'11.5" E (Fig. 1).

Observed daily precipitation (1951-2020) from five in situ stations (Ina, Nikki, Okpara, Parakou, and Tchaourou) was obtained from the Agence Nationale de la Météorologie (Météo-Bénin). The observed data are supplemented with simulations from climate models. In the Inter-model Comparison Project Phase 6 (CMIP6), a combination of Representative Concentration Pathway (RCP) and Shared Socioeconomic Pathway (SSP) scenarios (Riahi et al. 2017) was developed. Among these scenarios, historical, SSP245, and SSP585 scenarios from the AWI-CM, INM-CM, and EC-Earth3 climate models (Table 1) were used. These models were selected for their high spatial resolution and ability to reproduce extreme rainfall events in West Africa (Agyekum et al. 2022; Lebeza et al. 2024).

Table 1. Characteristics of the climate models used.

CMIP6	Institution	Atmosphere lat/lon (°)
AWI-CM-1-1-MR	Alfred Wegener Institute	0.9×0.9
INM-CM4-8	Institute for Numerical Mathematics (INM), Russia	1.5×2.0
EC-Earth3-CC	EC-EARTH consortium, The Netherlands/Ireland	0.7×0.7

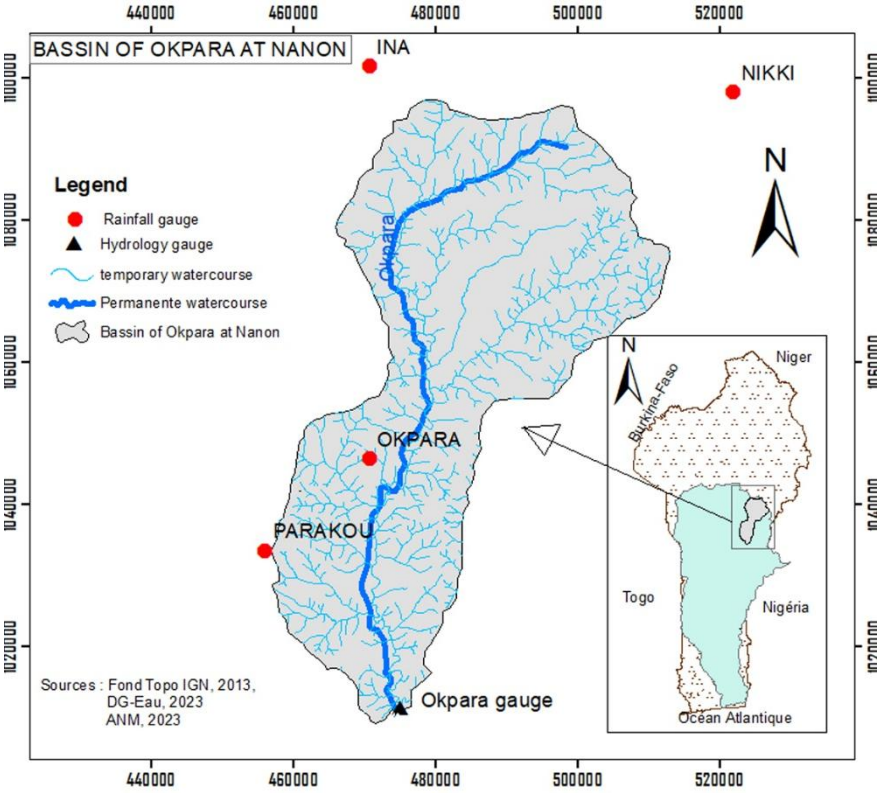

Fig. 1. Geographical location of the Okpara basin in Nanon.

2.2. Methods

Prior to using climate model data, bias correction needs to be applied at local scales (Wörner et al. 2019). Bias correction addresses biases in model output that result from how physical processes are captured in the original climate models, their boundary and initial conditions, and the effects of the numerical algorithms used for solving the partial differential equations within the model (Alamou et al. 2022). Bias correction also removes errors due to the large spatial scale of grid cell models that can vary with local climate specificity (Alamou et al. 2022). The ISI-MIP method (Hempel et al. 2013) is used in this study to bias-correct climate model simulations (historical, SSP245, and SSP585).

To assess trends in precipitation and temperature indices, the Mann-Kendall test (Mann 1945; Kendall 1975) was used. The non-parametric Mann-Kendall test is commonly used to detect monotonic trends in series of meteorological, hydrological, and environmental data (Bera 2017; Yu et al. 2017). The main advantages of the Mann-Kendall test are (1) low sensitivity in homogeneous time series (Jaagus 2006) and (2) there is no assumption of normally distributed residuals (Tabari, Talaee 2011).

To find whether the means of the projected periods are statistically different from the mean of the reference period, Student's t-test was used. Under the null hypothesis of equal sample means and the alternative hypothesis of unequal sample means, the t-statistic is calculated as in Obada et al. (2021).

2.3. Extreme precipitation indices

To characterize extreme precipitation events in the Okpara Basin at Nanon, we investigated eight indices of extreme precipitation recommended by the Expert Team on Climate Change Detection and Indices (ETCCDI) (Zhang et al. 2011) (Table 2).

Table 2. List of extreme climate indices used.

Index	Name	Définition	Unit
RX1day	Maximum daily precipitation year	Annual maximum daily precipitation	mm
Rx5day	Maximum precipitation of 5 consecutive days year	Annual maximum of 5 consecutive days with precipitation	mm
R1mm	Number of wet days	Number of days with precipitation (PRCP > = 1 mm) in each year	day
CDD	Consecutive dry days	Maximum length dry drays (PRCP < 1 mm) in each year	day
CWD	Consecutive wet days	Maximum length of wet days (PRCP > = 1 mm) in each year	day
R95p	Very wet days	When annual precipitation is > 95th percentile	mm
R99p	Extremely wet days	When annual precipitation is > 95th percentile	mm
PRCPTOT	Total annual precipitation of wet days	Total annual precipitation in wet periods (RR > = 1 mm)	mm

3. Results

3.1. Performance of the bias correction

Figures 2 and 3 show the performance of bias correction on precipitation indices. On the one hand, these results show that the ISI-MIP method used to correct the data performed well. The figures show that the

differences between the raw data from the climate models and the observed data are reduced after the biases have been corrected. Correcting for bias brings the model simulations closer to the observed data. In this way, climate model projections can be used with maximum confidence to study the future evolution of temperature and precipitation extremes in the basin.

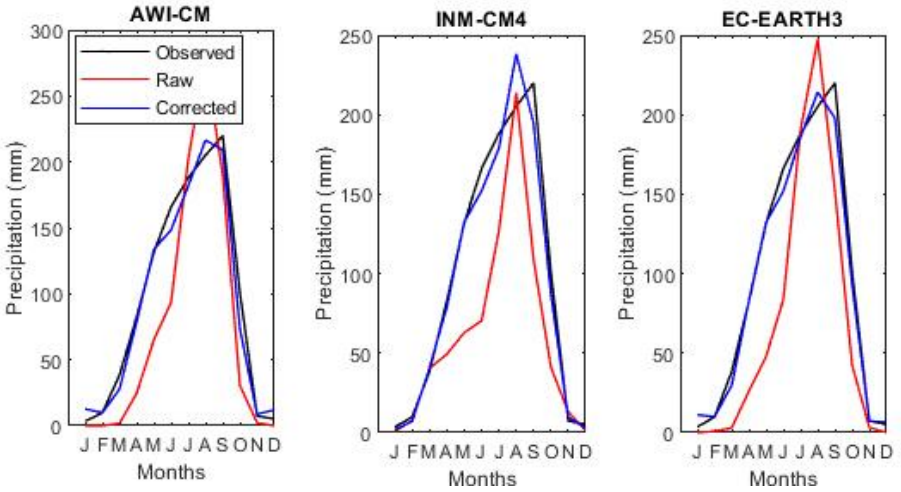

Fig. 2. Performance of the correction method on monthly precipitation.

3.2. Recent trends in precipitation indices in the Nanon basin

Figure 3 shows the spatial distribution of the frequency indices: consecutive dry days (CDD), consecutive wet days (CWD), and number of wet days (R1mm). The first line of this figure shows that the CDD varies between 44.3 and 164.7 days, with an average of 109.4 ± 20.7 days over the period 1951 to 2020. It shows an increasing gradient with latitude. This index shows a significant upward trend at the 95% threshold throughout the basin, with higher trends recorded to the east of the basin. On average, this trend is about 4 days per decade in the basin. Furthermore, the CDD index shows, through Hubert's test at the 1% Scheffé test significance level, a breakpoint in 1961 dividing the study period into two sub-periods (1951-1961 and 1961-2020). These two sub-periods have respective averages of 85.291 and 114.431 days.

The CWD varies between 2.9 and 13.2 days, with an average of 5.8 ± 1.4 days. This index decreases as latitude increases, shows an average upward trend of 0.1 days/decade in the basin, and is only significant in the extreme north. There is no break in the CWD.

The R1mm index varies between 46.2 and 102.3 days, with an average of 75.8 ± 9.4 days. It shows a significant upward trend of 0.6 days/decade on average over the northern basin. Similar to CWD, it shows a latitudinal gradient that decreases as latitude increases. The R1mm shows a breakpoint, which is highlighted by Hubert's test at the 1% significance level of the Scheffé test. This point was detected in 1956. An average of 91.16 days was recorded for the first period (1951-1956) and an average of 76.865 days for the second period (1957-2020).

Figure 4 shows the spatial distribution of the average intensity indices (RX1day, RX5day, R95p, R99p and PRCPTOT), their trends and significance, as well as their chronological evolution and probable

breakpoints over the historical period (1951-2020). Figure 5 shows that the RX1day index varies between 52.7 and 141.5 mm, with an average of 78.1 ± 11.2 mm, while the RX5day index varies between 90.5 and 185.5 mm, with an average of 124 ± 17.6 mm. The R95p index varies between 60.3 and 581.6 mm with an average of 228.1 ± 77.8 mm, while the R99p varies between 0 and 251.6 mm with an average of 70.3 ± 35.9 mm. PRCPTOT varies between 671.6 and 1575.3 mm with an average of 1128.8 ± 155.5 mm. The RX5day, R95p, R99p, and PRCPTOT indices show a non-significant downward trend, except for PRCPTOT, which is significant in the northern basin at the 1% threshold. The RX1day is increasing non-significantly at the 1% threshold. Of all the intensity indices, only PRCPTOT shows a breakpoint detected in 1969.

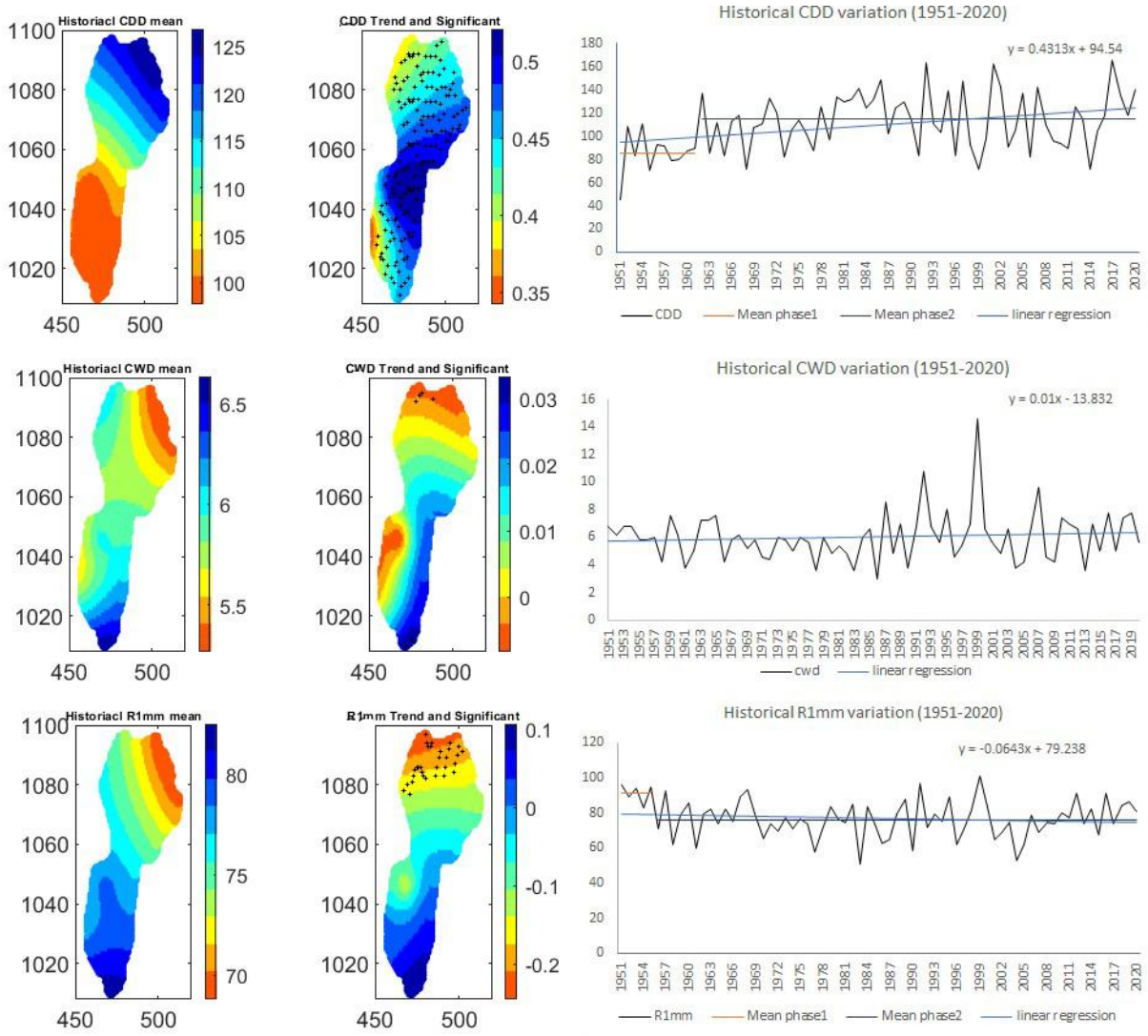

Fig. 3. Trends of frequency indices (R1mm, CDD, and CWD) over 1951-2020.

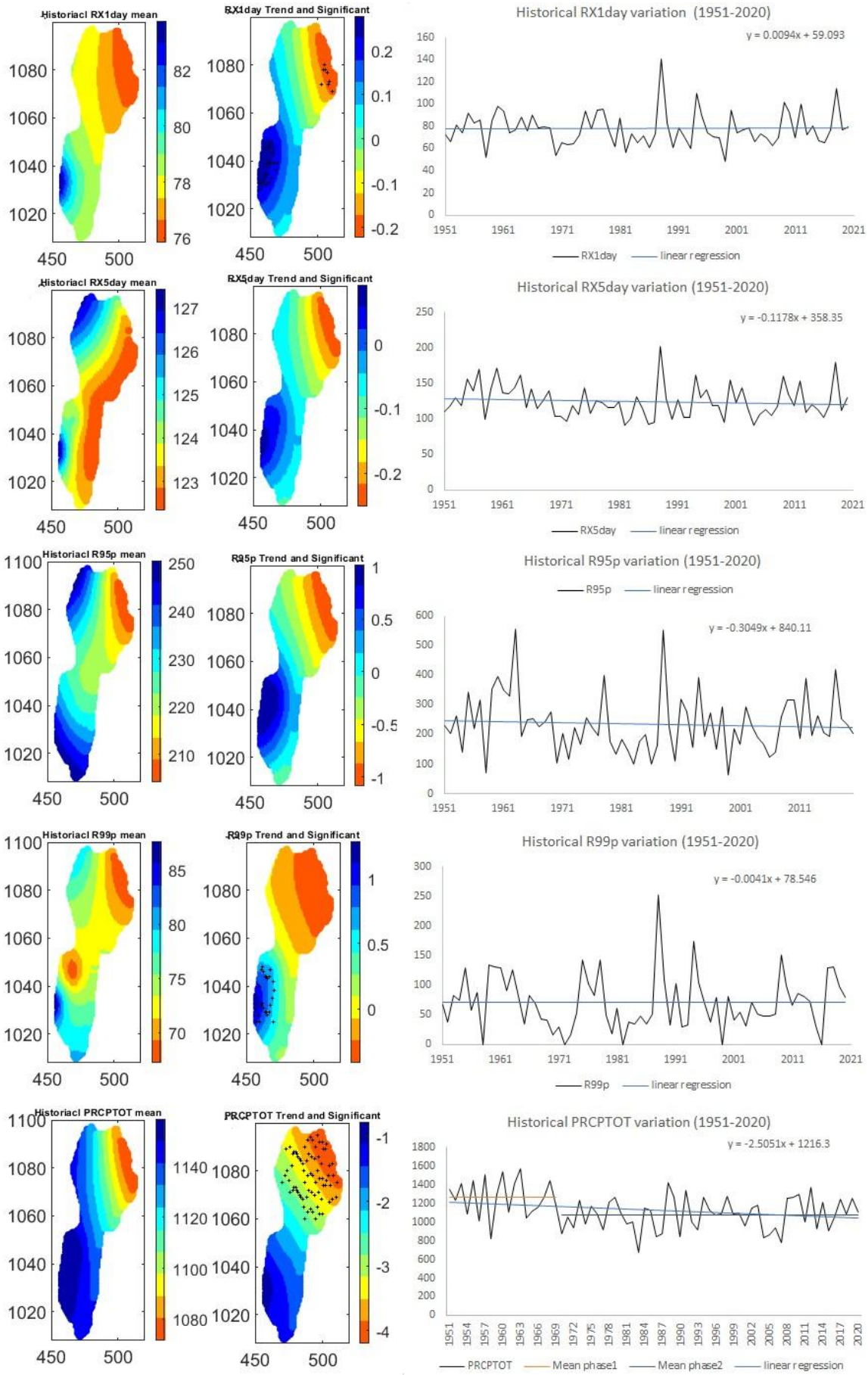

Fig. 4. Trends of intensity indices (RX1day, RX5day, R95p, R99p, and PRCPTOT) over 1951-2020.

3.3. Future trends and changes in climate indices in the Nanon basin

Figure 5 shows future trends in the CDD and CWD indices of the AWI-CM, EC-Earth3, and INM-CM4 climate models under the SSP245 and SSP585 scenarios for the period 2030-2099. Under the SSP245 scenario, the AWI-CM model indicates significant increasing trends that vary from 1.5 to 5 days per decade. The EC-Earth3 model indicates decreasing trends of –4.1 to –1.5 days per decade. These trends are significant in the center of the basin. Under the SSP585 scenario, the INM-CM4 model indicates non-significant mixed (downward and upward) trends for CDD. Significant downward trends in CDD, varying from –5.4 to –3 days per decade, are indicated in the northern basin for the EC-Earth3 model, while non-significant upward trends are predicted for the AWI-CM model.

The CWD index shows non-significant upward trends under both scenarios for the AWI-CM. Using the EC-Earth3 model, non-significant downward trends are indicated for the SSP245 scenario, whereas significant upward trends are predicted for the SSP585 scenario across the entire basin. For the INM-CM4 model, regardless of the scenario, the CWD index shows downward trends across the entire basin; the trends are significant for the SSP585 scenario. Overall, the predicted trends for all models and scenarios are very small (less than 1 day per decade).

Figure 6 presents the changes in the CDD and CWD indices under the SSP245 and SSP585 scenarios (2030-2099) compared to the observation period (1951-2020). The CDD could increase by 0 to 5 days in the southern part of the basin and decrease by 0 to 7 days in the northern part of the basin under both SSP245 and SSP585 scenarios for the AWI-CM model compared to the observation period. The EC-Earth3 model predicts increases of about 7 to 15 days for the CDD under the SSP245 scenario and 6 to 12 days under the SSP585 scenario compared to the observation period. These increases are statistically significant in the central and southern basin. The INM-CM4 model indicates a significant decrease in CDD over the entire basin, varying from 13 to 33 days for SSP245 and from 19 to 40 days for SSP585. The indications are a possible decrease in the dry period in the basin and an increase in the rainy season under these scenarios. The CWD could increase significantly over the entire basin compared to the observation period, regardless of the scenario and the climate model considered. These increases are of the order of 3 to 7 days for the AWI-CM and EC-Earth3 models but relatively low for the INM-CM4 model (1 to 3 days).

Figure 7 shows the future trends of the PRCPTOT and RX1day indices under the SSP245 and SSP585 scenarios (2030-2099). The three climate models indicate non-significant increasing trends in the basin, except for the INM-CM4 model, which predicts decreasing trends. However, significant upward trends were found over the entire basin with the SSP585 scenario for all models. For the PRCPTOT index, the trends vary from 7.1 to 9.1 mm/year, 9.4 to 13.8 mm/year, and 12.1 to 13.4 mm/year, respectively, for the AWI-CM, EC-Earth3 and INM-CM4 models. For the RX1day index, the trends vary between 6 and 11 mm/decade for the 3 climate models. The RX5day index shows significant upward trends across the basin under the SSP585 scenario for the 3 climate models considered, varying from 12 to 18 mm/decade.

The R1mm index shows downward trends under both AWI-CM model scenarios; significant under the SSP245 scenario, and varying between 1 and 2 days/decade, while the EC-Earth3 and INM-CM4 models indicate significant upward trends under the SSP585 scenario across the basin and vary between 1.1 and 3.5 days/decade for EC-Earth3 and 3.6 and 4.3 days/decade for INM-CM4. These significant increases in the number of wet days are consistent with the increase in PRCPTOT in the basin.

Figure 8 shows the changes in the PRCPTOT and RX1day indices under the SSP245 and SSP585 scenarios compared to observations. The PRCPTOT and RX1day indices could increase significantly across the basin regardless of the scenario and climate model considered, except for the SSP245 scenario of the AWI-CM climate model, which indicates significant decreases in the south of the basin and non-significant increases in the north. Under the SSP245 scenario, the PRCPTOT index could increase compared to the observation period by 230 to 440 mm/year, 270 to 420 mm/year and 200 to 280 mm/year, respectively for the AWI-CM, EC-Earth3, and INM-CM4 models under the SSP245 scenario compared to increases of 550 to 700 mm/year, 430 to 550 mm/year and 420 to 500 mm/year under SSP585. This indicates that future periods will be wetter than past periods under both scenarios . The SSP585 scenario would be wetter than the SSP245 scenario. The increases are also significant for the RX1day index. They vary from 6 to 16 mm/year under SSP245 and 25 to 45 mm/year under SSP585 for the EC-Earth3 model. For the INM-CM4 model, they vary from 55 and 75 for both scenarios. Regardless of the scenario and climate model, the R1mm and RX5day indices could increase significantly across the basin. The R1mm index could increase by 6 to 14 days/year under both scenarios for the EC-Earth3 and INM-CM4 models compared to 10 to 30 days/year for the AWI-CM model.

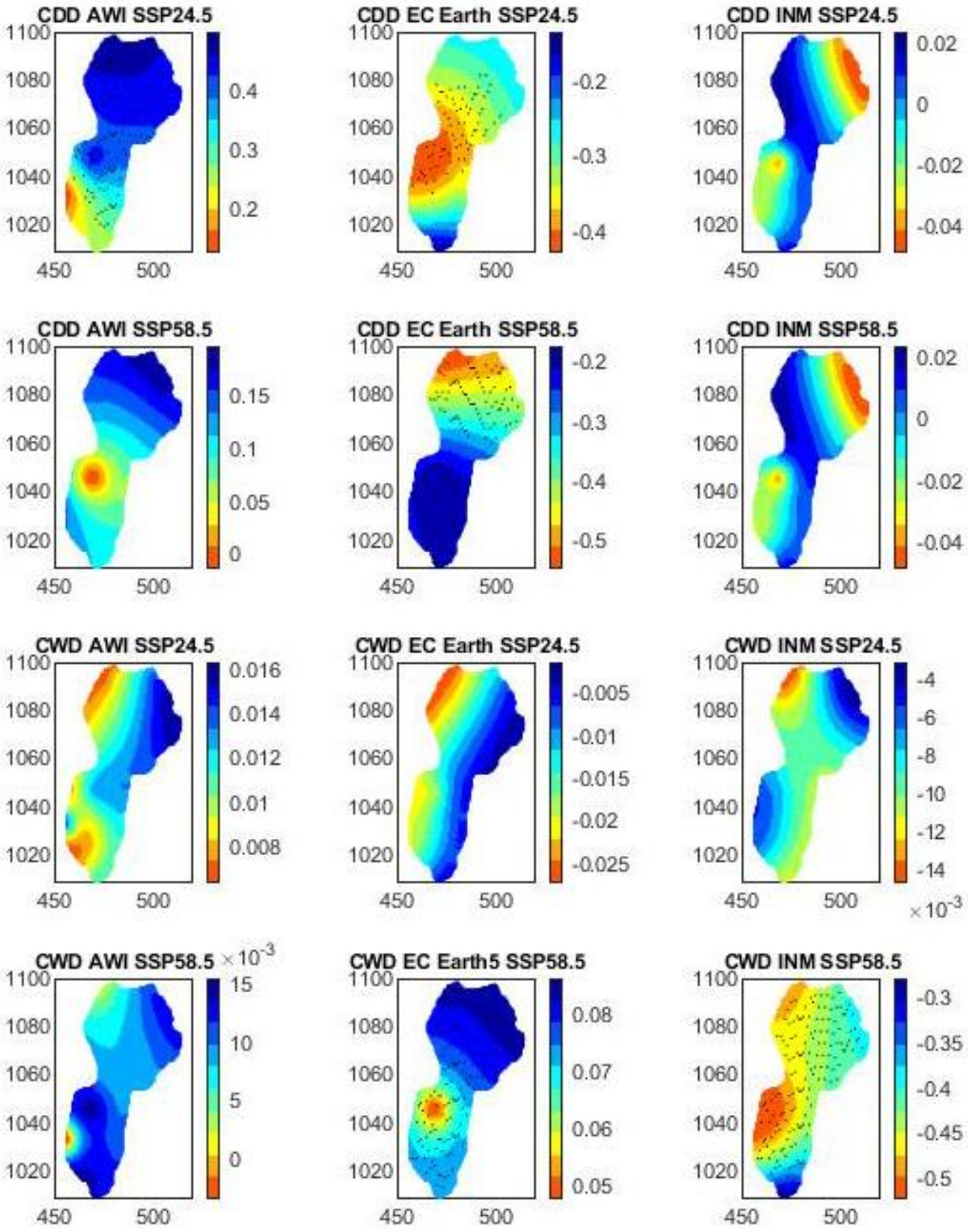

Fig. 5. Trends in CDD and CWD under SSP245 and SSP585 scenarios (2031-2099) at Nanon.

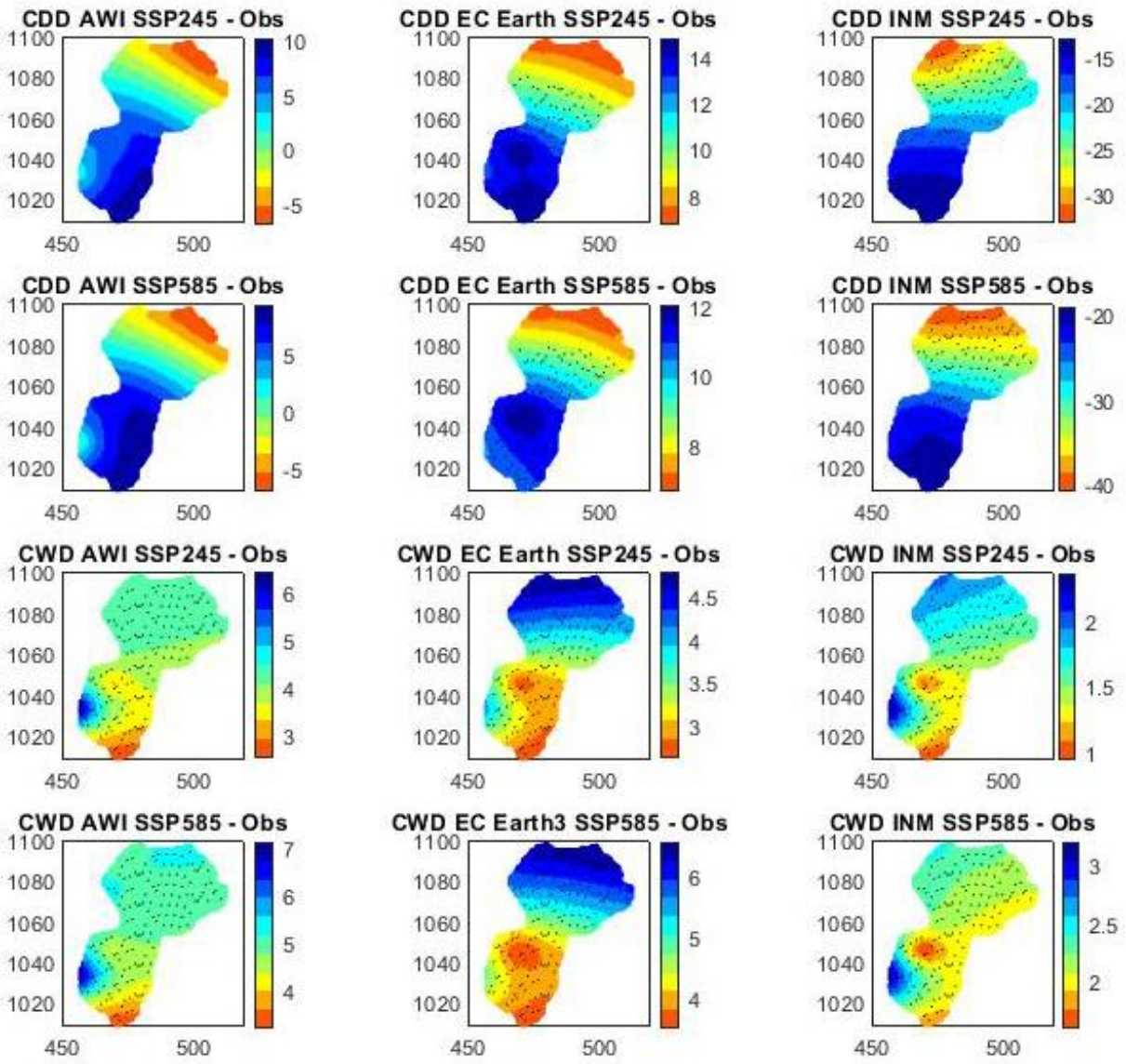

Fig. 6. Changes in CDD and CWD under SSP245 and SSP585 scenarios (2031-2099) compared to historical observations (1951-2020) at Nanon.

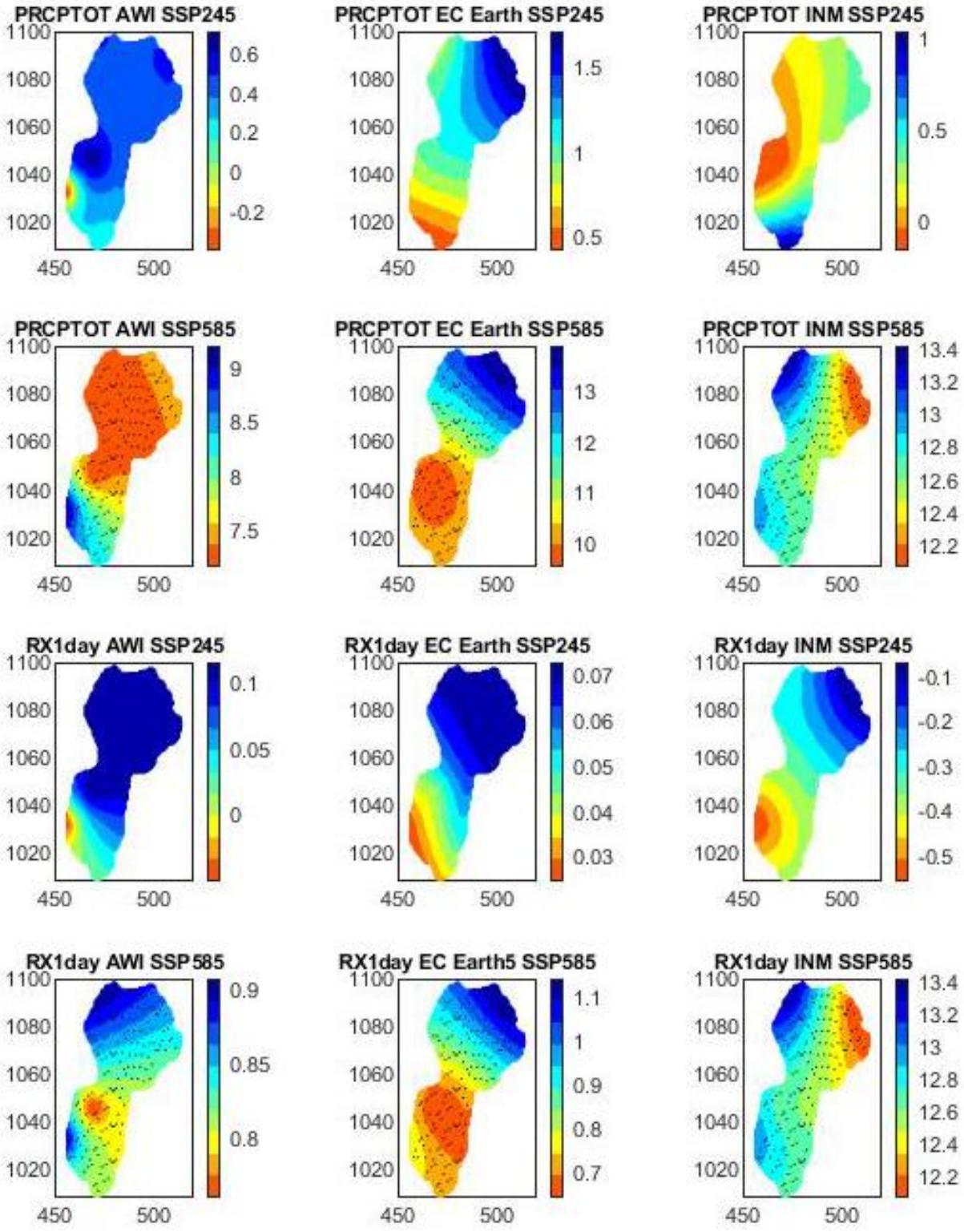

Fig. 7. Trends in PRCPTOT and RX1day under SSP245 and SSP585 scenarios (2031-2099) at Nanon.

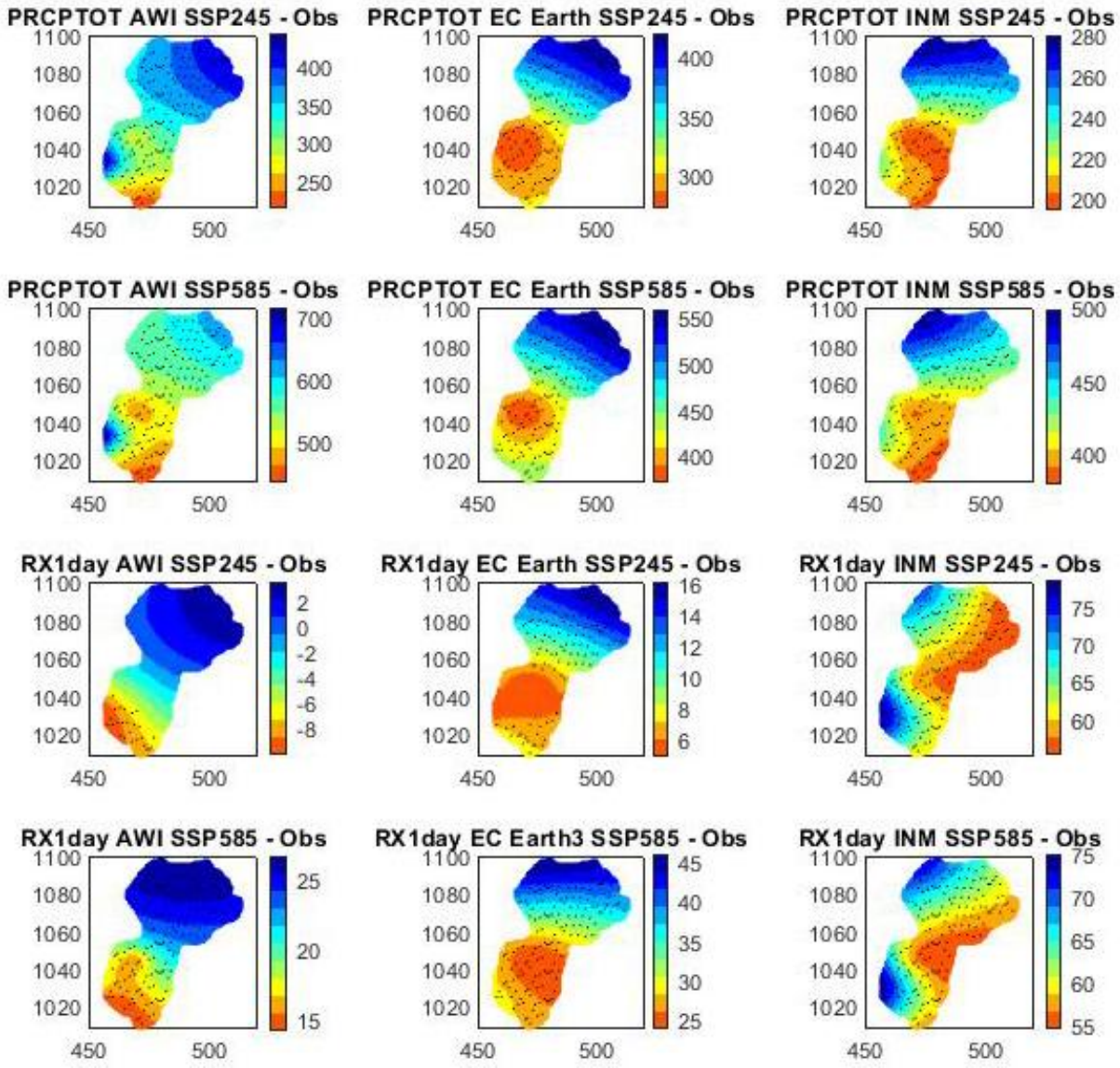

Fig. 8. Changes in PRCPTOT and RX1day under SSP245 and SSP585 scenarios (2031-2099) compared to historical observations (1951-2020) at Nanon.

4. Discussion

In this study, three global climate models are used for a local-scale study: the Okpara watershed at Nanon outlet. The models have shown sufficient capacity to reproduce the region's precipitation pattern, making them ideal tools for studying the impact of climate change in the region. However, the models are unable to simulate precipitation amounts correctly, underestimating the dry months and overestimating the wettest months (July-August). These difficulties in simulating the local climate can be explained by the limited spatial resolution of these models, which does not allow them to capture fine-scale phenomena, and by the complexity of the interactions between the components of the climate system. Furthermore, these difficulties may also be due to poor integration of regional boundary conditions (such as ocean currents and topography) and local forcings such as changes in land use. These limitations lead to errors in key variables such as clouds, precipitation, and winds, which are influenced by fine-scale processes.

The ISI-MIP method used to correct model errors has effectively brought the model simulation data closer to the observation data. As a result, the projections using these models in the region would be acceptable.

Over the 2030-2099 period, maximum consecutive wet day (CWD) and maximum consecutive days (CDD) indices show upward and downward trends depending on SSP scenarios and climate models. For the number of wet days (R1mm), maximum daily precipitation (RX1day), maximum precipitation of 5 consecutive (RX5day), heavy precipitation (R95p), very heavy (R99p), and total annual precipitation of wet days (PRCPTOT) indices of all scenarios and models generally display significant upward trends. These results are consistent with those obtained at the global scale with SSPs scenarios (Shi et al. 2021; Anil, Raj 2024, Tavosi et al. 2024; Nazarenko et al. 2025). For Africa, Lagos-Zúñiga et al. (2024) report mixed trends in the Rx5day and CDD indices, with significant spatial heterogeneity in both magnitude and direction using RCPs scenarios. The frequency and intensity of heavy precipitation events are also expected to increase with rising greenhouse gas emissions in East Africa (Ayugi et al. 2021; Demissie et al. 2025). Similar results are reported by Ebedi-Nding et al. (2024) for Central Africa. In the far future (2071-2100), intensified wet conditions are expected on the Guinea Coast under SSP585, according to Ilori and Adeyewa (2025).

The upward trends observed for most of the extreme precipitation indices led to a significant increase in these indices under the SSP245 and SSP585 scenarios over the period of 2030-2099 compared to the reference period (1951-2020). This suggests an intensification of wet conditions in the future in the Okpara basin. This intensification could increase the risk of flooding (Aryee et al. 2024). Other consequences of this warming are an increase in gross domestic product (GDP) and population exposed to hazards (Shi et al. 2021; Yang, Zhao 2024). These trends reveal a need for specific management and adaptation strategies focused on flooding. The findings of this work could provide useful information for the development of climate change mitigation and adaptation policies in a region that is highly vulnerable to the consequences of climate change due to a constantly increasing population and a lack of adequate adaptation strategies (Diatta et al. 2020). The various development programs of the municipality of Parakou should account for these aspects to preserve the safety of people and property, and with the aim of efficiently managing possible water-related crises.

5. Conclusion

The analysis of precipitation indices in the Okpara Basin at Nanon over the period 1951-2020 shows non-significant increasing trends for consecutive wet days (CWD), number of wet days (R1mm), and maximum daily precipitation (RX1day). Maximum consecutive dry days (CDD), maximum precipitation of 5 consecutive (RX5day), heavy precipitation (R95p), very heavy precipitation (R99p), and total annual precipitation of wet days (PRCPTOT) indices indicated non-significant downward trends. Projections from AWI-CM, INM-CM4, and EC-Earth3 climate models under the SSP245 and SSP585 scenarios indicate statistically significant upward trends for most of the indices, leading to a statistically significant

increase of these indices in the future related to the observation period. An intensification of wet conditions is therefore expected in the basin, and it is important that basin managers, planners, and decision-makers must develop strategies to prevent and properly manage possible water-related crises in the basin.

References

Agyekum J., Annor T., Quansah E., Lamptey B., Okafar G., 2022, Extreme precipitation indices over the Volta Bassin: CMIP6 model evaluation, Scientific African, 16, DOI: 10.1016/j.sciaf.2022.e01181.

Alamou E.A., Zandagba J.E., Biao E.I., Obada E., Da-Allada C.Y., Bonou F.K., Pomalegni Y., Baloitcha E., Tilmes S., Irvine P.J., 2022, Impact of stratospheric aerosol geoengineering on extreme precipitation and temperature indices in West Africa using GLENS simulations, Journal of Geophysical Research: Atmospheres, 127 (9), DOI: 10.1029/2021JD035855.

Anil S., Raj P.A., 2024, An exhaustive investigation of changes in projected extreme precipitation indices and streamflow using CMIP6 climate models: A case study, Journal of Earth System Sciences, 133, DOI: 10.1007/s12040-024-02267-6.

Aryee J.N.A., Afrifa F.O.T., Agyapong K-H., Gyau Frimpong N.A., Quagraine K.T., Davies P., 2024, Quantifying climatic heavy-precipitation-induced floods in West Africa using multiple precipitation indices, Scientific African, 25, DOI: 10.1016/j.sciaf.2024.e02309.

Atiah W.A., Tsidu G.M., Amekudzi L.K., Yorke C., 2020, Trends and interannual variability of extreme rainfall indices over Ghana, West Africa, Theorical and Applied Climatology, 140, 1393-1407, DOI: 10.1007/s00704-020-03114-6.

Attogouinon A., Lawin A.E., M'Po Y.N., Houngue R., 2017, Extreme precipitation indices trend assessment over the Upper Oueme River Valley (Benin), Hydrology, 4 (3), DOI: 10.3390/hydrology4030036.

Ayugi B., Dike V., Ngoma H., Babaousmail H., Mumo R., Ongoma V., 2021, Future changes in precipitation extremes over East Africa based on CMIP6 models, Water, 13 (17), DOI: 10.3390/w13172358.

Bera S., 2017, Trend analysis of rainfall in Ganga Basin, India during 1901-2000, American Journal of Climate Change, 6 (1), 116-131, DOI: 10.4236/ajcc.2017.61007.

Demissie T., Diro G.T., Duku C., Solomon D., Jimma T.B., 2025, Current and projected changes in climate extremes and agro-climatic zones over East Africa, Theoretical and Applied Climatology, 156, DOI: 10.1007/s00704-025-05405-2.

Diatta S., Diedhiou C.W., Dione D.M., Sambou S., 2020, Spatial variation and trend of extreme precipitation in West Africa and teleconnections with remote indices, Atmosphere, 11 (9), DOI: 10.3390/atmos11090999.

Ebedi-Nding D.D., Tamoffo A.T., Mouassom F.L., 2024, Extremes events and socio-economic impacts in central Africa: a CMIP6-based analysis of projections, Modeling Earth Systems and Environment, 10, 6575-6598, DOI: 10.1007/s40808-024-02139-4.

Hempel S., Frieler K., Warszawski L., Schewe J., Piontek F., 2013, A trend-preserving bias correction – the ISI-MIP approach, Earth System Dynamics, 4 (2), 219-236, DOI: 10.5194/esd-4-219-2013.

Hounguè R., Lawin A.E., Moumouni S., Afouda A.A., 2019, Change in climate extremes and pan evaporation influencing factors over Ouémé Delta in Benin, Climate, 7 (1), DOI: 10.3390/cli7010002.

Ilori O.W., Adeyewa D.Z., 2025, Projected changes in extreme rainfall events over West Africa and its sub-regions: a multi-scenario climate analysis, Meteorology and Atmospheric Physics, 137, DOI: 10.1007/s00703-025-01081-z.

IPCC, 2007, Climate Change 2007: Impact, Adaptation and Vulnerability, Working Group II Contribution to the Fourth Assessment Report of the Intergovernmental Panel on Climate Change, Cambridge University Press.

IPCC, 2013, Climate Change 2013: The Physical Science Basis, The Working Group I Contribution to the Fifth Assessment Report of the Intergovernmental Panel on Climate Change.

IPCC, 2021, Climate Change 2021: The Physical Science Basis, The Working Group I Contribution to the Sixth Assessment Report of the Intergovernmental Panel on Climate Change.

Jaagus J., 2006, Trends in sea ice conditions in the Baltic Sea near the Estonia coast during the period 1949/1950 – 2003/2004 and their relationships to large scale atmospheric circulation, Boreal Environment Research, 11, 169-183.

Kendall M., 1975, Rank Correlation Methods, 4th edition, Charles Griffin, London.

Lagos-Zúñiga M., Balmaceda-Huarte R., Regoto P., Torre L., Olmo M., Lyra A., Pareja-Quispe D., Bettolli M.L., 2024, Extreme indices of temperature and precipitation in South America: trends and intercomparison of regional climate models, Climate Dynamics, 62, 4541-4562, DOI: 10.1007/s00382-022-06598-2.

Lebeza T.M., Gashaw T., Bayabil H.K., van Oel P.R., Worqlul A.W., Dile Y.T., Chukalla A.D., 2024, Performance of specific CMIP6 GCMs for simulating the historical rainfall and temperature climatology of Lake Tana sub-basin, Ethiopia, Scientific African, 26, DOI: 10.1016/j.sciaf.2024.e02387.

Mann H.B., 1945, Nonparametric tests against trend, Econometrica, 13 (3), 245-259, DOI: 10.2307/1907187.

N'Tcha M'Po Y., Lawin A.E., Yao B.K., Oyerinde G.T., Attogouinon A., Afouda A.A., 2017, Decreasing past and mid-century rainfall indices over Ouémé River Basin, Benin (West Africa), Climate, 5 (3), DOI: 10.3390/cli5030074.

Nazarenko L.S., Tausnev N.L., Elling M.T., 2025, Temperature and precipitation extremes under SSP emission scenarios with GISS-E2.1 Model, Atmosphere, 16 (8), DOI: 10.3390/atmos16080920.

Obada E., Alamou A.E., Biao I.E., Zandagba E.J., 2021, Interannual variability and trends of extreme rainfall indices over Benin, Climate, 9 (11), DOI: 10.3390/cli9110160.

Odoulami R.C., Akinsanola A.A, 2018, Recent assessment of West African summer monsoon daily rainfall trends, Weather, 73 (9), 283-287, DOI: 10.1002/wea.2965.

ONERC, 2018, Les événements météorologiques extrêmes dans un contexte de changement climatique, Rapport au Premier ministre et au Parlement, La documentation Française, 200 pp.

PNE-Bénin, 2008, Problématique de la gestion durable du barrage de l'Okpara : enjeux, défis majeurs et approches de solution pour l'alimentation en eau potable de la ville de Parakou, rapport, 8 pp.

Riahi K., van Vuuren D.P., Kriegler E., Edmonds J., O'Neill B.C., Fujimori S., Bauer N., Calvin K., Dellink R., Fricko O., Lutz W., Popp A., Cuaresma J.C., Samir K.C., Leimbach M., Jiang L., Kram T., Rao S., Emmerling J., Ebi K., Hasegawa T., Havlik P., Humpenöder, Da Silva L.A., Smith S., Stehfest E., Bosetti V., Eom E., Gernaat D., Masui T., Rogelj J., Strefler J., Drouet L., Krey V., Luderer G., Harmsen M., Takahashi K., Baumstark L., Doelman J.C., Kainuma M., Klimont Z., Marangoni G., Lotze-Campen H., Obersteiner M., Tabeau A., Tavoni M., 2017, The shared socioeconomic pathways and their energy, land use, and greenhouse gas emissions implications: An overview, Global Environmental Change, 42, 153-168, DOI: 10.1016/j.gloenvcha.2016.05.009.

Royer A., 2024, L'évolution des évènements météorologiques extrêmes avec les changements climatiques, Sciences et Technologies.

Shi X., Chen J., Gu L., Xu C.-Y., Chen H., Zhang L., 2021, Impacts and socioeconomic exposures of global extreme precipitation events in 1.5 and 2.0°C warmer climates, Science of the Total Environment, 766, DOI: 10.1016/j.scitotenv.2020.142665.

Tabari H., Talaee P.H., 2011, Temporal variability of precipitation over Iran: 1966-2005, Journal of Hydrology, 396 (3-4), 313-320, DOI: 10.1016/j.jhydrol.2010.11.034.

Tavosi M., Vafakhah M., Shekohideh H., Sadeghi S.H., Moosavi V., Zheng Z., Yang Q., 2024, Rainfall extreme indicators trend and meteorological drought changes under climate change scenarios, Water Resources Management, 38, 4393-4413, DOI: 10.1007/s11269-024-03871-3.

Wörner V., Kreye P., Meon G., 2019, Effects of bias-correcting climate model data on the projection of future changes in high flows, Hydrology, 6 (2), DOI: 10.3390/hydrology6020046.

Yang Y., Zhao N., 2024, Future projections of compound temperature and precipitation extremes and corresponding population exposure over global land, Global and Planetary Change, 236, DOI: 10.1016/j.gloplacha.2024.104427.

Yu X., Zhao G., Zhao W., Yan T., Yuan X., 2017, Analysis of precipitation and drought data in Hexi Corridor, Northwest China, Hydrology, 4 (2), DOI: 10.3390/hydrology4020029.

Zhang X., Alexander L., Hegerl G.C., Jones P., Klein Tank A., Peterson T.C., Trewin B., Zwiers F.W., 2011, Indices for monitoring changes in extremes based on daily temperature and precipitation data, WIREs Climate Change, 2 (6), 851-870, DOI: 10.1002/wcc.147.

Reviewers cooperating with Editorial Board of
Meteorology Hydrology and Water Management Magazine in 2025

Acharya Bibek (Nepal)
Bayrak Mustafa (Turkey)
Bryła Monika (Poland)
C.P. Priju (India)
Chaibou Abdoul Aziz Saidou (Niger)
Curic Mladen (Serbia)
Diémé Laurent Pascal Malang (Senegal)
Gorbachova Liudmyla (Ukraine)
Jaczewski Adam (Poland)
Kasiulis Egidijus (Lithuania)
Kažys Justas (Lithuania)
Khokhlov Valeriy (Ukraine)
Kleniewska Małgorzata (Poland)
Kohnová Silvia (Slovak Republic)
Kumar Krishan (India)
Kutyłowska Małgorzata (Poland)
Ledvinka Ondřej (Czech Republic)
Mourad Mohamed (Egypt)
Nowakowska Monika (Poland)
Oktawiec Michał (Poland)
Oliveria Carlos (Brazil)
Ozga-Zieliński Bogdan (Poland)
Parchure Amit (India)
Perz Adam (Poland)
Pietrucha-Urbanik Katarzyna (Poland)
Raoufi Homayoon (Afghanistan)
Sezen Cenk (Turkey)
Stachura Gabriel (Poland)
Sulik Sławomir (Poland)
Szwed Małgorzata (Poland)
Terassi Paulo Miguel de Bodas (Brazil)
Trapaidze Vazha (Georgia)
Twaróg Bernard (Poland)
Wartalska Katarzyna (Poland)
Yaméogo Joseph (Burkina Faso)
Zhezheria Vladyslav (Ukraine)
Żyromski Andrzej (Poland)

THANK YOU

METEOROLOGY HYDROLOGY AND WATER MANAGEMENT
IMGW-PIB Science Journal since 2013